[redacted]

JOINT INSTITUTE FOR AERONAUTICS AND ACOUSTICS

[redacted]

National Aeronautics and
Space Administration

Ames Research Center

JIAA TR - 85

Stanford University

THEORETICAL STUDIES ON FLAPPED DELTA WINGS

BY

S. Oh, D. Tavella, and L. Roberts

Stanford University
Department of Aeronautics and Astronautics
Stanford, CA 94305

AUGUST 1988

Abstract

The effects of leading edge flaps on the aerodynamic characteristics of a low aspect-ratio delta wing are studied theoretically. As an extension of the classical cross-flow plane analysis and in order to include separated shear layers, an analogy between three dimensional steady conical and two dimensional unsteady self-similar flows is explored. This analogy provides a simple steady-unsteady relationship. The criteria for the validity of the steady-unsteady analogy are also examined.

Two different theoretical techniques are used to represent the separated shear layers based on the steady-unsteady analogy, neglecting the trailing edge effect. In the first approach, each vortex system is represented by a pair of concentrated vortices connected to the separation points by straight feeding sheets. The analysis is carried out in the cross-flow plane by mapping the wing trace, by means of the Schwarz-Christoffel transformation, into the real axis of the transformed plane, allowing for exact satisfaction of boundary conditions. Although the model does not yield satisfactory comparison with experiments, the effects of leading edge flaps on delta wing aerodynamics are observed qualitatively.

In the second approach, the vortex cloud method is adopted for simulating the flow field in the cross-flow plane. The separated shear layers are replaced with a cloud of discrete vortices and the boundary element method is employed to represent

the wing trace by a vorticity distribution. Combined with the steady-unsteady analogy, the vortex cloud method constitutes a numerically efficient methodology with good definition of separated shear layers and good prediction of surface pressure distribution. A simple merging scheme is used to model the core region of the vortical flow as a single vortex by imposing a restriction on the shear layer rotation angle. The results are compared with experiments and with results from 3-D panel calculations.

In agreement with experimental evidence, it is found that flap deflection causes a decrease of lift and drag due to partial suppression of the leading edge vortical flow, while the lift-to-drag ratio increases due to the thrust component of the force acting on the flap surfaces.

Acknowledgment

This research was supported by NCC 2-55.

Nomenclature

$a(x)$	total half span length
a_{ij}	geometric influence coefficient
c	speed of sound
D	drag
$\mathbf{e}$	unit vector
e	total energy
F	complex potential in the cross-flow plane
f	wing cross-section shape function
G	normalized vorticity distribution function inside core
H	total head
i	internal energy, $\sqrt{-1}$
k	ratio of main wing span length to total span length
L	lift
l_j	length of j^{th} vorticity panel
M	Mach number
m	similarity coefficients
N	normal force
p	static pressure
R	resultant force, characteristic length scale
r	radial direction in cross-flow plane

$\bar{r}$	conical coordinate, Prandtl's similarity coordinate
S	wing and vortex sheet geometry
T	characteristic time scale
t	time coordinate
U	chordwise component of free-stream velocity
$\mathbf{u}$	velocity
u	$\lvert\mathbf{u}\rvert$
v	disturbance velocity component
$\overline{v}$	complex conjugate of the velocity in the cross-flow plane
$\mathbf{x}$	vector position
x	chordwise coordinate of delta wing
$\tilde{x}, \tilde{y}, \tilde{z}$	stretched wing reference coordinate system through Prandtl-Glauert transformation
$\hat{y}, \hat{z}$	rectangular form of conical coordinates
α	angle of attack
β_i	inside angle at the i^{th} vertex of the polygon
χ	vorticity distribution function inside core
δ	flap deflection angle, dirac delta function
δ_{ij}	kronecker delta function
ϵ	half apex angle of main delta wing
η	spanwise component of bound vorticity
Γ	vortex strength

γ	specific heat ratio
κ_i	polygon i^{th} vertex external angle
μ	viscous coefficient
$\vec{\Omega}$	vorticity on wing surface
$\vec{\omega}$	vorticity
ω	$\lvert\vec{\omega}\rvert$
Φ	total velocity potential
ϕ	disturbance velocity potential
φ	dimensionless form of disturbance velocity potential
Ψ	cross flow stream function
ρ	density
ϱ	distance normalized with vortex core radius
σ	$\sigma = y + iz$, complex representation of cross-flow plane
ς	vortex core radius
Θ	$\Theta = \xi + i\vartheta$, complex representation of transformed plane
$\Theta_2, \Theta_3, \Theta_5, \Theta_6$	transformation coefficients
$\tilde{\tau}$	viscous stress tensor
θ	angular coordinate in cross-flow plane

Subscripts

c	conical flow, core
F	flap

h	hinge vortex
l	leading edge vortex
p	potential
r	rotational
s	separation point, body surface
u	2-D unsteady self-similar flow
v	vortex position
w	main wing
x, y, z	wing reference coordinate system
∞	freestream

$\overline{(\ )}$ indicates complex conjugate

$(\ )'$ length scale normalized with $a(x)$

Contents

Chapter 1

Introduction

1.1 General Remarks on the Flow Field around Flapped Delta Wings

The flow field on the leeside of low aspect ratio delta wings at incidence is characterized by a vortical flow originating at the leading edges, as shown in Fig. 1. This vortical flow is very stable up to a certain angle of attack and causes an enhancement of lift, called vortex lift, by inducing low pressure regions on the upper surface. Generating a stable vortical flow above the wing surface is an efficient way of obtaining additional lift,[1] especially during maneuvering and in take-off and landing. At high angle of attack, however, the vortical flow also causes the following problems:

- Large lift-dependent drag due to loss of leading-edge suction
- Side force due to asymmetric formation of vortical flows
- Pitch-up due to vortex breakdown at high angle of attack

Fig. 2 shows typical concepts for handling these problems, as well as the basic functions of the concepts.

Leading edge flaps have been applied to the design of subsonic-transonic tactical delta wing aircraft, and to aircraft that require both supersonic cruise efficiency and high maneuverability.[2] On the other hand, the flow field about a wing with leading edge flaps is more complex than that of a wing without flaps due to the appearance of an additional vortical system originating at the flap hinge, as shown in Fig. 3. It has been shown that the effect of these hinge vortices is negligible, except at small angle of attack with large flap deflection angle.[3] Various shapes of leading edge flaps have been studied experimentally in the past, in an attempt to optimize their influence on the aerodynamics of delta wings.[4–14] One of the effects of leading edge flaps is to increase the lift-to-drag ratio by reducing the wing drag. This augmentation occurs due to a thrust component of force acting on the flap surfaces. Fig. 4 shows the variation of lift-to-drag ratio in cruise for three different aircraft configurations: the F-16 aircraft, a precramp wing* aircraft of supersonic design, and a flapped delta wing, for a wide range of Mach number. Leading edge flaps also have the detrimental effect of partially suppressing the vortical flow, thereby reducing the total lift. These two phenomena have been observed experimentally[3,12–16] and theoretically.[17,18]

1.2 Previous Studies

In view of the important influence of vortical flow on wing design, numerous studies have been conducted on the leading edge vortices around low aspect ratio delta wings.[20–51] These studies were aimed at understanding the fundamental physics of rolled-up shear layers and the effect of the vortical flows on the aerodynamic characteristics of the wing. Main topics of such studies were:

* a cranked wing planform with twist and camber

- Mathematical modeling of rolled-up shear layers
- Flow field analysis of the core regions of vortical flows
- Three-dimensional (3-D) boundary layer calculations and prediction of separation lines
- Vortex breakdown

The analysis of the core region of the vortical flow is essentially a part of the study of the rolled-up shear layer. The main difficulties in the study of the core region arise from the mathematical treatment of the tightly coiled shear layers and the effect of viscosity.[34–37] The calculation of the 3-D boundary layer[38,39] and the prediction of separation lines[51,52] can not be made until the flow field external to the boundary layer, a flow field composed of rolled-up shear layers, has been determined. A description of the core regions combined with trailing edge effects is also necessary for an improved understanding of vortex breakdown. In this regard very little progress has been made in the analysis of this problem, however.

The first successful model for the vortical flow was a straight-feeding-sheet model used by Brown and Michael, as shown in Fig. 5.[20,21] Other attempts have used analytical approaches,[23–29] vortex cloud methods,[30–33] and 3-D panel methods.[40–42] More recently, with the aid of high computing power, simulations of separated vortical flows have been carried out using numerical solutions of either the Euler or Navier-Stokes equations.[47–50]

Studies on control of vortical flow were started in late 1970's, after some understanding of the physics of vortical flow had been achieved. At the beginning, attempts to suppress the vortical flow were made when it was recognized that conventional control surfaces could not operate well in this type of flow. Leading edge flaps were found to be quite effective in providing vortical flow control, as was

revealed in experiments conducted with complex-geometry delta-wing aircraft.[15,16] Those experimental results showed that leading edge flap deflection was effective in promoting an attached flow configuration by suppressing the formation of leading edge vortices. The tabbed-vortex-flap* has also been considered to avoid asymmetric vortex breakdown with sideslip angle. Both plain leading edge flaps and tabbed-vortex-flaps caused significant increments in lift-to-drag ratio.

In the experimental study by Rao *et al.*[7–9] various shapes of leading edge devices were suggested to reduce lift-dependent drag. Frink[10] performed a study of the effects of leading edge flaps by using a 3-D free-vortex-sheet method.** Hoffler *et al.*[14] investigated the aerodynamic influence of tabbed-vortex-flaps and plain leading edge flaps, both experimentally and using a 3-D panel method. Marchman[11,12] performed similar experiments for different delta wing configurations in an attempt to confine the vortical flow to the vicinity of flap surfaces in order to reduce drag, while keeping the lift almost constant. The effect of a vortex fence, which is an alternative form of leading edge flap, as shown in Fig. 2, has been investigated by Reddy using a 3-D Free Vortex Sheet Method.[19] Lee[3] made experiments with a flapped delta wing with conical geometry, including flow visualization, to observe the influence of the hinge vortices.

1.3 Present Study

In this study, two different theoretical techniques are used to assess the effects of leading edge flaps on the aerodynamic characteristics of slender delta wings. The

* An alternative form of leading edge flaps; a second leading edge flap is attached to the main flap with different deflection angle.

** Frink's 3-D panel calculations made use of only one vortical system, existence of the hinge and trailing edge vortex systems being neglected.

first technique uses the simplest vortex model in a plane normal to the wing surface (cross-flow plane) to explore the general trends of the aerodynamic coefficients of flapped delta wings. The second technique improves on the first by incorporating an inviscid vortex cloud simulation of the shear layers. Both approaches ignore the presence of the trailing edge.

The foundation of both approaches is based on the mathematical analogy between conical steady and two-dimensional (2-D) unsteady self-similar flows, which results in a simple relationship between time and space coordinates. With this analogy (steady-unsteady analogy) a steady conical flow field can be reduced to a 2-D unsteady self-similar flow in the cross-flow plane. This steady-unsteady analogy under the conical assumptions yields more accurate results in the case of supersonic flow,[53,54] since the whole flow field is conical, whereas for subsonic flow the analogy ceases to be valid near the trailing edge and the apex. The maximum flap deflection angle for which the steady-unsteady methodology remains valid is found by using a simple geometrical relationship. A deflection beyond that limit would cause the leading edge vortex system to move under the wing surface, a situation that cannot be accounted for in the context of a cross-flow plane analysis. For both techniques, the effect on the lift-to-drag ratio of the resultant forces acting on wing and flap surfaces is derived to first order using a coordinate transformation.

The two approaches are now described in more detail. The first approach constitutes an extension of the vortex model first suggested by Brown and Michael. The study used here simulates each vortex system by a pair of concentrated vortices with straight feeding sheets. The unknowns in the problem, vortex strength and position, are found from force equilibrium conditions imposed on the singularity

systems. The Schwarz-Christoffel transformation is used to allow for exact satisfaction of boundary conditions. Although the model does not give satisfactory results on vortex position and pressure distribution the global quantities, such as lift, drag and normal force, are satisfactorily calculated. Particular attention is paid to the following aspects:

- Influence on lift-to-drag ratio of forward components of the forces acting on the flap surfaces
- Variation of vortex position and strength with flap deflection angle
- Contribution of vortical and attached flows* to the aerodynamic forces

In the second approach, the vortex cloud method, the steady-unsteady analogy plays a more explicit role. Assuming that geometric and aerodynamic slenderness are satisfied, this analogy reduces a conical steady flow field to a 2-D, unsteady self-similar flow through the relationship $x = Ut$, where x is the chordwise coordinate and U is the chordwise component of the free-stream velocity. Using this analogy the vortex cloud method, an intrinsically 2-D approach originally developed to describe separated flow past bluff bodies,[55–76] is modified to simulate a conical flow. This approach leads to a numerically efficient methodology with good definition of shear layers. Another motivation for the use of this approach is the parallel between the physics of planar shear layers and the delta wing rolled-up shear layer, as suggested in Fig. 6.[77]

Rolled-up shear layers are replaced by discrete vortices having finite core size, so that all of the rotational and viscous effects are assumed to take place within the core, while outside the core the flow field is governed by conventional potential

* As will be discussed later, the lift of a delta wing with separated flow may be expressed as the sum of a contribution that would have been caused by a wing with attached flow and a component due to the separated flow.

theory. Viscous diffusion of each vortex is taken into account through a formulation derived by Prandtl.[78] In conical flow the "vortex jungle ", which usually forms in the wake region in 2-D flow simulations, would represent the region of tightly coiled shear layers, or core region of the delta wing flow field. Such a representation of the core region as a "vortex jungle" is inappropriate in conical flow due to the appearance of the high axial velocity, which would violate the aerodynamic slenderness assumption and could not be modeled in a 2-D flow context.[79] To improve the computational efficiency as well as to avoid this unphysical core representation, a merging scheme between neighboring vortices and near the core region is employed. A quasi-steady Kutta condition is imposed at leading edges and flap hinges by fixing the separation angle of new vortices generated at each computational step. If the Kutta condition were unsteady the new vortex strength and position would be coupled with the strengths and positions of other vortices in the shear layers and those of vortices representing the wing surface, leading to a matrix inversion operation for computing the bound vortex strengths.[56–60] With this treatment of the Kutta condition matrix inversion, which requires a great computational effort, can be avoided at each iteration by decoupling the Kutta condition from the system of equations.

In the context of the vortex cloud method, attention is focused on the following aspects:

- Distortions of rolled-up shear layer with flap deflection angle
- Pressure distribution
- Variation of vortex position and strength with flap deflection
- General features of trailing edge wake structure

The last item is explored under the assumption that the conicality of the flow field

is sustained up to the trailing edge. These results are compared with experimental and other theoretical studies, including results from 3-D panel computations.[19,61]

1.4 Overview

This work is divided into six chapters. Chapter 2 contains the derivation of the basic mathematical equations, including the analogy between conical steady and 2-D unsteady self-similar flow, the range of flap deflection angle where the steady-unsteady analogy is valid, and the lift-to-drag ratio of a flapped delta wing to the first order. Chapter 3 describes the first approach together with the fundamental concepts of the Brown-Michael vortex model and the Schwarz-Christoffel transformation. In Chapter 4 the basic mathematical background of the vortex cloud method for a 2-D unsteady flow is derived and adapted to conical flows, and numerical implementation is carried out. At the end of these chapters the results of each method are presented and the mathematical and numerical limitations of each technique are discussed. Chapter 5 shows the comparison of the results from the two methods with those from other analyses. Chapter 6 contains discussions on the relative accuracy of each of the techniques implemented here as compared with experiments and other methods of calculations, as well as recommendations for future work.

Chapter 2

Basic Mathematical Analysis

The basic mathematical analysis to treat steady 3-D conical flows is derived. The linearized potential equation is derived from the Navier-Stokes equations, and transformed through the Prandtl-Glauert transformation. The assumption of conicality of the flow field around delta wings is examined for the subsonic and supersonic cases. Criteria for applicability of the cross-flow plane analysis are obtained through the mathematical analogy between a steady 3-D conical flow, which is governed by the linearized potential equation, and a 2-D unsteady self-similar ideal flow. The range of validity of the steady-unsteady analysis is examined. The fundamental equations for the two approaches, the straight-feeding-sheet and vortex cloud models, are presented on the basis of the analogy. An expression for the lift-to-drag ratio of flapped delta wings is derived to first order.

2.1 Linearized Potential Equation

As described in Chapter 1, the flow field around a delta wing is composed of the boundary layer on the wing surface, the rolled-up shear layers originating at the leading edge, the secondary vortex systems originating in flow separation from the

upper surface, and the trailing edge wake, as shown in Fig. 1. The equations governing this flow field are:

Conservation of mass:

$$\frac{\partial \rho}{\partial t} + \nabla \cdot (\rho \mathbf{u}) = 0 \tag{2.1.1}$$

Conservation of momentum:

$$\frac{\partial (\rho \mathbf{u})}{\partial t} + \nabla \cdot (\rho \mathbf{u}\mathbf{u}) = -\nabla p + \nabla \cdot \tilde{\tau} \tag{2.1.2}$$

Conservation of energy:

$$\frac{\partial \rho e}{\partial t} + \nabla \cdot (\rho e \mathbf{u}) = -\nabla \cdot (p\mathbf{u}) + \nabla \cdot (\tilde{\tau} \cdot \mathbf{u}) \tag{2.1.3}$$

where $\tilde{\tau}$ is the stress tensor which, using Stokes hypothesis for the molecular viscosity, can be expressed as

$$\tau_{ik} = \mu \left(\frac{\partial u_i}{\partial x_k} + \frac{\partial u_k}{\partial x_i} - \frac{2}{3} \delta_{ik} \frac{\partial u_l}{\partial x_l} \right) \tag{2.1.4}$$

and e is the total energy per unit mass

$$e = i + u^2/2 \tag{2.1.5}$$

The boundary conditions are

$$\mathbf{u} = 0 \quad \text{at } S(x,y,z) = 0 \tag{2.1.6a}$$

$$\mathbf{u} = \mathbf{U} \quad \text{as } \mathbf{x} \to \infty \tag{2.1.6b}$$

where $S(x,y,z) = 0$ represents the wing surface geometry.

Usually an aircraft operates in the range of high Reynolds number, where the thickness of the boundary layer and the shear layer become so small that all the viscous effects are confined to thin regions. Thus, the viscous effects can be neglected in most of the flow field. The boundary condition on the wing surface is

$$\mathbf{u} \cdot \mathbf{n} = 0 \tag{2.1.7}$$

where $\mathbf{n}$ is the outward normal vector on the wing surface.

In the absence of viscous effects the rolled-up shear layers are infinitely thin with boundary conditions requiring that there must be no pressure jump across them. These concepts lead to an inviscid model for the flow field governed by the Euler equations. The flow field is still rotational, in which case the velocity can be decomposed into two components as follows

$$\mathbf{u} = \mathbf{u}_p + \mathbf{u}_r \tag{2.1.8}$$

where $\mathbf{u}_p$ and $\mathbf{u}_r$ are the potential and rotational part of the velocity respectively. These two components have the following properties

$$\mathbf{u}_p = \nabla\Phi \quad \text{or} \quad \nabla \times \mathbf{u}_p = 0 \tag{2.1.9a}$$

$$\nabla \times \mathbf{u}_r = \vec{\omega} \tag{2.1.9b}$$

where Φ is a scalar potential and $\vec{\omega}$ is the vorticity.

Neglecting the viscous terms Eqs. (2.1.1) and (2.1.2) become

$$\frac{D\rho}{Dt} = -\rho\nabla^2\Phi - \rho\nabla\cdot\mathbf{u}_r \tag{2.1.10}$$

$$\begin{aligned}\nabla\left(\frac{\partial\Phi}{\partial t} + \frac{|\nabla\Phi|^2}{2} + \int_{p_\infty}^{p}\frac{dp}{\rho}\right)\\ = -\frac{\partial\mathbf{u}_r}{\partial t} - \nabla\left(\nabla\Phi\cdot\mathbf{u}_r + \frac{{u_r}^2}{2}\right) + (\nabla\Phi + \mathbf{u}_r)\times\vec{\omega}\end{aligned} \tag{2.1.11}$$

Assuming that the flow field is homentropic the following relationships hold

$$\begin{aligned}\frac{D}{Dt}\int_{p_\infty}^{p}\frac{dp}{\rho} = \frac{d}{dp}\left(\int_{p_\infty}^{p}\frac{dp}{\rho}\right)\frac{Dp}{Dt} = \frac{1}{\rho}\frac{dp}{d\rho}\frac{D\rho}{Dt}\\ = \frac{c^2}{\rho}\frac{D\rho}{Dt} = -c^2\left(\nabla^2\Phi + \nabla\cdot\mathbf{u}_r\right)\end{aligned} \tag{2.1.12}$$

where c is the speed of sound.

Combining Eqs. (2.1.11) and (2.1.12) there results

$$\nabla^2\Phi - \frac{1}{c^2}\left(\frac{\partial^2\Phi}{\partial t^2} + \frac{\partial}{\partial t}|\nabla\Phi|^2 + \nabla\Phi\cdot\nabla\left(\frac{1}{2}|\nabla\Phi|^2\right)\right)$$
$$= -\nabla\cdot\mathbf{u}_r$$
$$- \frac{1}{c^2}\left(-\mathbf{u}_r\cdot\frac{\partial\nabla\Phi}{\partial t} - \mathbf{u}_r\cdot\nabla\frac{|\nabla\Phi|^2}{2} + \frac{\partial}{\partial t}\int\mathbf{A}\cdot d\mathbf{x} + (\nabla\Phi+\mathbf{u}_r)\cdot\mathbf{A}\right) \tag{2.1.13}$$

where

$$\mathbf{A} = \frac{\partial\mathbf{u}_r}{\partial t} - \nabla\left(\nabla\Phi\cdot\mathbf{u}_r + \frac{{u_r}^2}{2}\right) + (\nabla\Phi+\mathbf{u}_r)\times\vec{\omega} \tag{2.1.14}$$

The left-hand side of Eq. (2.1.13) is exactly the same as the full potential equation for a compressible gas. The right-hand side can be interpreted as the source of rotational effects.

Let

$$\Phi = Ux + U\tan\alpha\, y + \phi \tag{2.1.15}$$

where α is the angle between the free-stream and the x direction and

$$\mathbf{u}_r = (u_{rx}, u_{ry}, u_{rz}) \tag{2.1.16}$$

Assuming the flow field is steady and all the disturbance velocities are small compared to the uniform free-stream velocity Eq. (2.1.13) gives, after neglecting terms of second and higher order in α, ϕ and u_r

$$\frac{\partial^2\phi}{\partial x^2} + \frac{1}{1-{M_\infty}^2}\left(\frac{\partial^2\phi}{\partial y^2} + \frac{\partial^2\phi}{\partial z^2}\right)$$
$$= -\frac{\partial u_{rx}}{\partial x} - \frac{1}{1-{M_\infty}^2}\left(\frac{\partial u_{ry}}{\partial y} + \frac{\partial u_{rz}}{\partial z}\right) \tag{2.1.17}$$

where M_∞ is the free-stream Mach number.

Applying the Prandtl-Glauert transformation for subsonic flow

$$\tilde{x} = x, \qquad \tilde{y} = y\sqrt{1-{M_\infty}^2}, \qquad \tilde{z} = z\sqrt{1-{M_\infty}^2} \tag{2.1.18}$$

to Eq. (2.1.17) there results

$$\frac{\partial^2\phi}{\partial\tilde{x}^2} + \frac{\partial^2\phi}{\partial\tilde{y}^2} + \frac{\partial^2\phi}{\partial\tilde{z}^2} = -\frac{\partial u_{rx}}{\partial\tilde{x}} - \frac{1}{\sqrt{1-{M_\infty}^2}}\left(\frac{\partial u_{ry}}{\partial\tilde{y}} + \frac{\partial u_{rz}}{\partial\tilde{z}}\right) \tag{2.1.19}$$

which is a form of the Poisson equation.

As mentioned before, all of the rotational effects are confined to thin layers. Green's theorem will be applied by treating the shear layers as part of the boundaries. Green's theorem states that a potential function can be obtained through a suitable distribution of singularities on the boundaries,[80–82] in this case the wing surface and the shear layers, as follows

$$\phi = \frac{1}{4\pi}\oint\frac{1}{|\mathbf{x}|}\nabla\phi\cdot\mathbf{n}dS - \frac{1}{4\pi}\oint\phi\left(\mathbf{n}\cdot\nabla\frac{1}{|\mathbf{x}|}\right)dS \tag{2.1.20}$$

where S represents the surface of the boundaries and $\mathbf{n}$ is the outward normal vector.

Eq. (2.1.20) shows that the velocity potential ϕ is due to a surface distribution of sources and doublets. The density of sources is $-\nabla\phi\cdot\mathbf{n}$ per unit area. The density of the doublets is ϕ per unit area and the doublet axis is directed along the inward normal to the surface.

Once the boundaries are replaced with a suitable distribution of singularities, the governing equation of the flow field outside the boundaries is

$$\frac{\partial^2\phi}{\partial\tilde{x}^2} + \frac{\partial^2\phi}{\partial\tilde{y}^2} + \frac{\partial^2\phi}{\partial\tilde{z}^2} = 0 \tag{2.1.21}$$

For supersonic flow the Prandtl-Glauert transformation is

$$\tilde{x} = x, \qquad \tilde{y} = y\sqrt{{M_\infty}^2-1}, \qquad \tilde{z} = z\sqrt{{M_\infty}^2-1} \tag{2.1.22}$$

and the governing equation becomes

$$-\frac{\partial^2\phi}{\partial\tilde{x}^2}+\frac{\partial^2\phi}{\partial\tilde{y}^2}+\frac{\partial^2\phi}{\partial\tilde{z}^2}=\frac{\partial u_{rx}}{\partial\tilde{x}}-\frac{1}{\sqrt{M_\infty{}^2-1}}\left(\frac{\partial u_{ry}}{\partial\tilde{y}}+\frac{\partial u_{rz}}{\partial\tilde{z}}\right) \quad (2.1.23)$$

In the supersonic case the confined rotational effects can also be replaced with suitable singularities,[81,82] leading to a statement similar to Eq. (2.1.20). The governing equation outside the singular regions is in this case

$$-\frac{\partial^2\phi}{\partial\tilde{x}^2}+\frac{\partial^2\phi}{\partial\tilde{y}^2}+\frac{\partial^2\phi}{\partial\tilde{z}^2}=0 \quad (2.1.24)$$

Eqs. (2.1.21) and (2.1.24) show that the linearized potential equation can be reduced through the Prandtl-Glauert transformation to

$$\pm\frac{\partial^2\phi}{\partial\tilde{x}^2}+\frac{\partial^2\phi}{\partial\tilde{y}^2}+\frac{\partial^2\phi}{\partial\tilde{z}^2}=0 \quad (2.1.25)$$

which implies that the governing equation in case of subsonic flow is transformed to that of an incompressible flow and in supersonic flow to that of another flow with free-stream Mach number equal to $\sqrt{2}$.

2.2 Cross-Flow Plane Analysis

2.2.1 Delta Wing Flow Conicality

The steady-unsteady analogy, which will be discussed later, is conducted under the assumption of conicality of the flow field. The conical assumption for a flow field requires that the wing geometry be conical and that there should not exist any characteristic length scales.[83] In a conical flow field, velocity and pressure are constant along rays emanating from the wing vertex.

Conicality of the flow field around a delta wing is better discussed using the small disturbance potential equation expressed in physical space. If the shear layers are

treated as a part of the boundaries, Eq. (2.1.17) becomes

$$\frac{\partial^2\phi}{\partial x^2} + \frac{1}{1-{M_\infty}^2}\left(\frac{\partial^2\phi}{\partial y^2} + \frac{\partial^2\phi}{\partial z^2}\right) = 0 \qquad (2.2.1)$$

For a supersonic flow the value $1-{M_\infty}^2$ becomes negative, resulting in a wave equation, with solutions propagating in the positive x direction. Hence, there is no effect of the length scale given by the trailing edge, since all of the disturbances as a result of the wing propagate only in the downstream direction.

For a finite delta wing subsonic conicality is an approximation that stems from ignoring the presence of the trailing edge and the singular nature of the apex, and must be interpreted as a local solution near the wing apex region. Hence, conicality for subsonic flows means that the area of interest is removed from the trailing edge and at some distance from the apex. This is consistent with experimental observation.[3]

2.2.2 Analogy between 3-D Conical and 2-D Unsteady Self-Similar Flows

In this section, as a extension of the classical slender body theory,[53,54,81,82] which does not consider separated shear layers, a comparison is made between a three-dimensional, steady flow field governed by Eq. (2.1.25) and growing conically in space, and a two-dimensional, self-similar ideal flow field growing in time, as illustrated in Fig. 7.

For a conical flow field around a delta wing with incidence angle α, the equation expressing the velocity potential can be written

$$\Phi_c(\tilde{x},r,\theta) = \tilde{x}\,U\,(1 + \bar{r}\tan\alpha\,\sin\theta + \varphi_c(\bar{r},\theta)) \qquad (2.2.2)$$

where $\bar{r} = r/\tilde{x}$, and φ_c is the dimensionless form of the disturbance velocity potential defined as

$$\varphi_c = \frac{\phi_c}{U\tilde{x}} \qquad (2.2.3)$$

The geometry of the vortex sheet and the wing surface can be also written

$$S(\tilde{x},r,\theta) \;=\; r \;-\; \tilde{x}\; f_c(\theta) \;=\; 0 \tag{2.2.4}$$

where $\tilde{x}\; f_c$ represents the cross-section of the wing and the rolled-up shear layer growing linearly in the $\tilde{x}$ direction.

In terms of φ_c, $\bar{r}$ and θ, Eq. (2.1.25) becomes

$$\frac{1}{\bar{r}}\frac{\partial\varphi_c}{\partial\bar{r}} \;+\; (1\pm\bar{r}^2)\frac{\partial^2\varphi_c}{\partial\bar{r}^2} \;+\; \frac{1}{\bar{r}^2}\frac{\partial^2\varphi_c}{\partial\theta^2} \;=\; 0 \tag{2.2.5}$$

where $+$ and $-$ correspond to the subsonic and supersonic case respectively.

The condition for the boundaries, the wing surface and the vortex sheet to be stream surfaces is

$$\nabla\Phi_c \cdot \nabla S \;=\; 0 \tag{2.2.6}$$

Combining Eq. (2.2.6) with Eqs. (2.2.2) and (2.2.4) gives

$$\begin{aligned}\left(1+\frac{v_{\tilde{x}}}{U}\right) f_c \;-\; &\left(\tan\alpha\;\sin\theta+\frac{\partial\varphi_c}{\partial\bar{r}}\right)\\ &+\;\frac{f_c'}{f_c}\left(\tan\alpha\;\cos\theta+\frac{1}{\bar{r}}\frac{\partial\varphi_c}{\partial\theta}\right) \;=\; 0\end{aligned} \tag{2.2.7}$$

where $v_{\tilde{x}}/U = \varphi_c - \bar{r}(\partial\varphi_c/\partial\bar{r})$

The boundary condition that there be no pressure difference across the vortex sheet can be formulated by invoking Bernoulli's equation

$$\begin{aligned}\frac{\tilde{p}-\tilde{p}_\infty}{(\rho U^2/2)} \;=\; &\left(1+\tan^2\alpha\right) \;-\; \left(1+\frac{v_{\tilde{x}}}{U}\right)^2 \;-\; \left(\tan\alpha\;\sin\theta+\frac{v_r}{U}\right)^2\\ &-\left(\tan\alpha\cos\theta+\frac{v_\theta}{U}\right)^2\end{aligned} \tag{2.2.8}$$

where $\tilde{p}$ is the pressure in the transformed space.

In terms of φ_c, $\bar{r}$ and θ Bernoulli's equation can be written as

$$-C_p = 2\frac{v_{\tilde{x}}}{U} + \left(\frac{v_{\tilde{x}}}{U}\right)^2 + \left(\frac{\partial \varphi_c}{\partial \bar{r}}\right)^2 + \frac{1}{\bar{r}^2}\left(\frac{\partial \varphi_c}{\partial \theta}\right)^2 + 2\tan\alpha\left(\frac{\partial \varphi_c}{\partial \bar{r}}\sin\theta + \frac{1}{\bar{r}}\frac{\partial \varphi_c}{\partial \theta}\right) \tag{2.2.9}$$

The value of this pressure must be the same on either side of the vortex sheet.

For an unsteady, self-similar, 2-D flow, Prandtl's analysis[22] showed that the vortex sheet has a shape that belongs to a self-similar family. Following his analysis with the assumption that the free-stream velocity causing separation is $U\tan\alpha$, the velocity potential and the geometry of the boundaries, including the vortex sheets, can be written

$$\Phi_u(t,r,\theta) = U\ r\ \tan\alpha\ \sin\theta + \frac{R^2}{T}\left(\frac{t}{T}\right)^{2m-1}\varphi_u(\bar{r},\theta) \tag{2.2.10}$$

$$S(t,r,\theta) = r - R\left(\frac{t}{T}\right)^m f_u(\theta) = 0 \tag{2.2.11}$$

where

$$\bar{r} = \left(\frac{r}{R}\right)\Big/\left(\frac{t}{T}\right)^m \tag{2.2.12}$$

and φ_u is the dimensionless form of the disturbance velocity potential defined as

$$\varphi_u = \frac{\phi_u}{\frac{R^2}{T}\left(\frac{t}{T}\right)^{2m-1}} \tag{2.2.13}$$

and T and R are constant reference values for time and length. m is a parameter which designates a particular member of the family of the vortex sheets. f_u is the collapsed geometry of the family of the vortex sheets and the wing geometry when those are represented in terms of the similarity variable $\bar{r}$. In this study the geometry of the wing surface is also growing with time.

For the 2-D unsteady case Laplace's equation can be written in terms of φ_u as

$$\frac{1}{\bar{r}}\frac{\partial \varphi_u}{\partial \bar{r}} + \frac{\partial^2 \varphi_u}{\partial \bar{r}^2} + \frac{1}{\bar{r}^2}\frac{\partial^2 \varphi_u}{\partial \theta^2} = 0 \tag{2.2.14}$$

The kinematic boundary conditions of the vortex sheet and wing surface are[80]

$$\frac{\partial S}{\partial t} + \nabla \Phi_i \cdot \nabla S = 0 \tag{2.2.15a}$$

$$\frac{\partial S}{\partial t} + \nabla \Phi_e \cdot \nabla S = 0 \tag{2.2.15b}$$

where subscripts i and e represent each side of the vortex sheet, and

$$\nabla \Phi_i = \nabla \Phi|_s + \frac{\vec{\gamma}}{2} \tag{2.2.16a}$$

$$\nabla \Phi_e = \nabla \Phi|_s - \frac{\vec{\gamma}}{2} \tag{2.2.16b}$$

where $\nabla \Phi|_s$ is the value on the vortex sheet, and $\vec{\gamma}$ is the vorticity intensity of the sheet.

Combining Eqs. (2.2.15) and (2.2.16) there results

$$\frac{\partial S}{\partial t} + \nabla \Phi|_s \cdot \nabla S = 0 \tag{2.2.17}$$

In terms of $\bar{r}$ and φ_u this equation becomes

$$\begin{aligned} m\, f_u - \left(\frac{T}{R}\left(\frac{T}{t}\right)^{m-1} U \tan\alpha \sin\theta + \frac{\partial \varphi_u}{\partial \bar{r}} \right) \\ + \left(\frac{T}{R}\left(\frac{T}{t}\right)^{m-1} U \tan\alpha \cos\theta + \frac{1}{\bar{r}}\frac{\partial \varphi_u}{\partial \theta} \right) \frac{f_u'}{f_u} = 0 \end{aligned} \tag{2.2.18}$$

The dynamic boundary condition on the vortex sheet is that the pressure must be the same on either side of the sheet. The pressure can be obtained from the

unsteady Bernoulli's equation

$$-C_p = -\frac{p-p_\infty}{(\rho U^2)/2} = -\tan^2\alpha + 2\frac{\partial \Phi_u}{\partial t} + {v_r}^2 - {v_\theta}^2 \qquad (2.2.19a)$$

$$= \frac{1}{U^2}\left(\frac{R}{T}\right)^2\left(\frac{t}{T}\right)^{2(m-1)} \times$$

$$\left((2m-1)\varphi_u - m\bar{r}\frac{\partial \varphi_u}{\partial \bar{r}} + \left(\frac{\partial \varphi_u}{\partial \bar{r}}\right)^2 + \frac{1}{\bar{r}^2}\left(\frac{\partial \varphi_u}{\partial \theta}\right)^2\right)$$

$$+ 2\frac{R}{T}\left(\frac{t}{T}\right)^{m-1}\frac{\tan\alpha}{U}\left(\sin\theta\frac{\partial \varphi_u}{\partial \bar{r}} + \cos\theta\frac{1}{\bar{r}}\frac{\partial \varphi_u}{\partial \theta}\right) \qquad (2.2.19b)$$

All the governing equations for the two cases, Eqs. (2.2.5), (2.2.7), (2.2.9) (the steady case) and Eqs. (2.2.14), (2.2.18), (2.2.19b), (the unsteady 2-D case), are written in nondimensional form. The unknowns become the scalar functions φ_c and φ_u, the collapsed form of the boundary geometry, including that of the vortex sheet, f_c and f_u for both cases. If the governing equations and auxiliary conditions were identical, the solutions would be the same in both cases. The conditions under which such is the case provide the criteria for a mathematical analogy between a steady conical flow and an unsteady, self-similar, 2-D flow. The mathematical requirements for such analogy to exist are as follows:

Laplace's equation for the two cases, Eqs. (2.2.5) and (2.2.14), becomes formally identical if $\bar{r} = 0$. Hence the requirement

$$\bar{r} \ll 1 \qquad (2.2.20)$$

The form of the boundary conditions for the vortex sheet and the wing surface, Eqs. (2.2.7) and (2.2.18), become the same if $v_x/U = 0, m = 1$ and $R/T = U$. Hence the requirements

$$v_{\tilde{x}} = U\left(\varphi_c - \bar{r}\frac{\partial \varphi_c}{\partial \bar{r}}\right) \ll U \qquad (2.2.21)$$

$$m = 1 \tag{2.2.22}$$

$$\frac{R}{T} = U \tag{2.2.23}$$

Conditions (2.2.22) and (2.2.23) also guarantee that Bernoulli's equation on the vortex sheet, Eqs. (2.2.9) and (2.2.19) becomes identical. The relationship between $\tilde{x}$ and t is given by

$$\tilde{x} = Ut \tag{2.2.24}$$

The analogy shows that the governing equations for a 3-D conical flow reduce to those for a 2-D unsteady self-similar flow if following criteria are met

- $\bar{r} \ll 1$
- $v_{\tilde{x}} \ll U$

These conditions mean that the conical flow field must be geometrically and aerodynamically slender.

2.3 Equations for the Straight-Feeding-Sheet and Vortex Cloud Models

2.3.1 Space-Time Transformation with Conical Flow Assumptions

With the analogy described in the previous section, a 3-D conical flow field can be obtained from the results of a 2-D unsteady self-similar flow field. The two approaches, which will be described in the next two chapters, are formulated on the basis of solving a 2-D unsteady flow in the cross-flow plane instead of solving 3-D conical flow directly. The solutions of the 2-D unsteady flow should reach a converged state when they are represented in terms of the similarity variable, due to the requirement of the self-similarity. From the relationship given by Eq. (2.2.24),

the time derivative can be rewritten as

$$\frac{d}{dt} = U\frac{d}{d\tilde{x}} \tag{2.3.1}$$

The length scales in the cross-flow plane should be normalized with a characteristic length, which is proportional to t, or from the relationship $\tilde{x} = Ut$, proportional to $\tilde{x}$. In both approaches all the length scales are normalized with the total span length $a(\tilde{x})$. From Fig. 8, $a(\tilde{x})$ is given by

$$a(\tilde{x}) = \frac{\tilde{x}\ \tan\ \epsilon}{k} \tag{2.3.2}$$

where k is the ratio of the main wing span length to the total wing span length. Combined with the conical assumption, Eq. (2.3.1) reduces to

$$\begin{aligned} U\ \frac{d\Sigma}{d\tilde{x}} = U\ \frac{\Sigma}{\tilde{x}} &= \frac{U\ \tan\epsilon}{ka(\tilde{x})}\ \Sigma \\ &= \frac{U\ \tan\epsilon}{k}\ \Sigma' \end{aligned} \tag{2.3.3}$$

where Σ stands for any quantity, growing linearly with x, associated with the kinematics of the flow field. As a consequence of this, $\Sigma' = \Sigma/a(\tilde{x}) = \text{constant}$.

2.3.2 Basic Equations for the Straight-Feeding-Sheet Model

In this approach the vortex structure is specified as consisting of a straight vortex sheet, emanating from the leading edge and flap hinges, and concentrated vortex cores, as shown in Fig. 9. The steady-unsteady analogy of the previous section showed that the analysis can be carried out in a time dependent fashion in the cross-flow plane, by solving Laplace's equation within prescribed boundaries, Eqs. (2.2.14) and (2.2.17). The vortex sheets are part of the boundaries. In the straight-feeding-sheet model Eq. (2.2.17) cannot be satisfied. This means that

the singularities representing the separated vortex sheets cannot be made force-free at every point. Instead of Eq. (2.2.17), a global force-free requirement for the vortex+sheet system is introduced. By representing the cross-flow plane with complex notation, the force per unit length acting on the j^{th} vortex+sheet system, as represented in the unsteady cross-flow plane formulation is [85,86]

$$\rho\, i\Gamma_j \left(\frac{d\sigma_{vj}}{dt} - v_{vj} \right) + \rho \frac{d(i\Gamma_j)}{dt} (\sigma_{vj} - \sigma_{sj}) = f_j \qquad (2.3.4)$$

where the cross-flow plane has been replaced by the complex representation $\sigma = y + iz$. Γ_j is the vortex strength and $\sigma_{vj} = y_{vj} + iz_{vj}$ is the vortex position, v_{vj} is the velocity at the vortex position excluding its own induced velocity, and σ_{sj} is the origin of the vortex sheet.

The first term is the force acting on the vortex core, the second is that acting on the vortex sheet. The term $(d\sigma_{vj}/dt) - v_{vj}$ is the relative velocity causing a Joukowsky force acting on the concentrated vortex core.[87] Equilibrium requires that this force be balanced by forces acting on the sheet. This will be imposed on each vortex+sheet separately. Eq. (2.2.14) is rewritten in complex notation as:

$$\nabla^2 F = \sum_{j=1}^{4} i\Gamma_j\, \delta(\sigma - \sigma_j) \qquad (2.3.5)$$

where F is the sum of the complex potential due to the vertical component of the free stream velocity, concentrated vortex and the wing trace, and $\delta(\sigma - \sigma_j)$ represents the dirac delta function, required to represent a singular vortex.

The basic equations for the straight-feeding-sheet model are the global force-free conditions:

$$f_j = 0 \qquad j = 1, 2, 3, 4 \qquad (2.3.6)$$

2.3.3 Basic Equations for the Vortex Cloud Model

As justified by the steady-unsteady analogy of Section **2.2.2**, the approach will be implemented in a 2-D unsteady form. Moreover, the vortex cloud method is a well-established technique to simulate a 2-D unsteady separated flows. In this approach the shear layers are replaced with a cloud of discrete vortices. The governing equation and the boundary condition given by Eqs. (2.2.14) and (2.2.17) were derived by treating the separated shear layers as a part of the boundary. In contrast, in the vortex cloud method the shear layers are not considered as a part of the boundary, instead, the shear layers are computed by tracing a large number of vortices, whose intensities and positions become known as the calculation proceeds. If the shear layers, represented by a vorticity distribution ω, are included in the field rather than in the boundaries, Eq. (2.2.14) takes the form

$$\nabla^2 \Psi = -\omega \tag{2.3.7}$$

where Ψ is the stream function.

The reason for the use of a stream function instead of a velocity potential is that, in terms of the stream function, the boundary value problem in the cross-flow plane is of Dirichlet type, and hence well-posed.

The tangency condition represented by Eq. (2.2.17) is now replaced by the requirement that the vorticity representing the shear layers be convected with the local velocity

$$\frac{D\omega}{Dt} = 0 \tag{2.3.8}$$

which implies that the vorticity of each particle is not changed during the convection and represents the conservation of vorticity.

In addition, the total circulation in the flow field, including the bound vortex due to the wing trace and the vortices distributed on the shear layers, should be conserved:[80]

$$\frac{d(\Gamma_W + \Gamma_{SL})}{dt} = 0 \tag{2.3.9}$$

where Γ_W and Γ_{SL} represent the circulation bound to the wing trace and that of the shear layers, respectively:

$$\Gamma_W = \oint_C v_s dl \tag{2.3.10a}$$

$$\Gamma_{SL} = \int\int \omega dS \tag{2.3.10b}$$

where v_s is the velocity on the wing surface, dl follows the contour around C along the wing trace, and S is the area including all the vortices representing the shear layers, as shown in Fig. 10.

The boundary conditions on the wing trace and the far field condition in terms of Ψ are

$$\Psi = \text{constant on wing surface} \tag{2.3.11a}$$

$$\Psi = \Psi_\infty \quad \text{as} \quad r \to \infty \tag{2.3.11b}$$

Details of implementation will be presented in Chapter 4.

The fundamental equations for the vortex cloud model are then Eq. (2.3.7) with boundary conditions (2.3.11), and Eqs. (2.3.8) and (2.3.9).

2.4 Validity Range of the Cross-Flow Plane Analysis

2.4.1 Slenderness of Flow Field around Delta Wings

In the flow field around delta wings having half apex angle ϵ and at angle of attack

α, the disturbances in the cross-flow plane, such as the rolled-up shear layers, remain within a region whose radius is one to two times the half span length, except when the angle of attack is extremely high. Thus the region of interest in this study is limited by a radius given by

$$r \sim \tilde{x} \tan \epsilon \ll \tilde{x} \tag{2.4.1}$$

since for a low aspect ratio delta wing the half apex angle is small. This satisfies the condition mentioned in Section **2.2.2**

$$\bar{r} \ll 1 \tag{2.4.2}$$

This also implies

$$O(\bar{r}) = O(\epsilon) \tag{2.4.3}$$

Experimental observations[79] have shown that the condition $v_{\tilde{x}} \ll U$ is also satisfied except in the core region of the rolled-up shear layers, where the axial velocity is larger than free-stream velocity. Hence, it can be assumed that the flow field around a slender delta wing at moderate angle of attack satisfies the geometric and aerodynamic slenderness conditions.

2.4.2 Relationship between α and ϵ

Although the steady-unsteady analogy developed in Section **2.2.2** does not impose any limitations on the relative magnitude of α and ϵ, as long as both are small, experimental observations indicate that the ratio α/ϵ must be within certain upper and lower bounds for the steady-unsteady analogy to hold.

For large α/ϵ the rolled-up shear layers do not form stable conical shapes but develop in a Karman-vortex-street pattern, thereby destroying conicality.[84] If α is of order smaller than that of ϵ, the shear layers roll up tightly within a small

region, thus becoming immersed in a region of dominant viscous effects. The viscous effect provides the characteristic length scale $\sqrt{\mu/(\rho U)}$ and as a result the flow field cannot be conical, which requires no characteristic length scale. Thus, the steady-unsteady analogy is valid if α and ϵ are of the same order.

2.4.3 Limit of Flap Deflection Angle

The cross-flow plane analysis in the framework of the steady-unsteady analogy, as described in Section **2.2.2**, implies that the significant velocity component causing separation along leading edges is the vertical component of the free-stream velocity in the cross-flow plane. The maximum flap deflection for which such analysis is valid is related to the velocity component normal to the flap surface. This can be shown by considering that, if that component were directed towards the upper flap surface, as shown in Fig. 11, the leading edge vorticity system would tend to be located under the wing. The cross-flow plane analysis cannot, by definition, exactly account for the actual orientation of the velocity component normal to the flap surface. Since the discrepancy between the actual velocity component normal to the flap surface and the one assumed by the cross-flow analysis increases with flap deflection, this method is expected to fail for flap deflection beyond a certain range. An assessment of that range can be made by considering the condition under which the velocity component normal to the flap surface vanishes (a situation unaccountable for in the cross-flow analysis.) This assessment is facilitated if the velocity component normal to the flap surface is assumed to be due to the free-stream velocity alone, that is, if the perturbation velocity of the wing is neglected. This is plausible if the angle of attack and apex angles are both small.

The outward normal vector, $\mathbf{n}$, on the flap surfaces can be obtained through

the coordinate transformations as shown in Fig. 12. $\mathbf{e}_x, \mathbf{e}_y, \mathbf{e}_z$ denote the unit vectors along axis x, y, z. The relationships between the unit vectors $(\mathbf{e}_x, \mathbf{e}_y, \mathbf{e}_z)$ and $(\mathbf{e}_{x_1}, \mathbf{e}_{y_1}, \mathbf{e}_{z_1})$, and between $(\mathbf{e}_{x_1}, \mathbf{e}_{y_1}, \mathbf{e}_{z_1})$ and $(\mathbf{e}_{x_2}, \mathbf{e}_{y_2}, \mathbf{e}_{z_2})$ are

$$\begin{pmatrix} \mathbf{e}_{x_1} \\ \mathbf{e}_{y_1} \\ \mathbf{e}_{z_1} \end{pmatrix} = \begin{pmatrix} \cos\epsilon & 0 & \sin\epsilon \\ 0 & 1 & 0 \\ -\sin\epsilon & 0 & \cos\epsilon \end{pmatrix} \begin{pmatrix} \mathbf{e}_x \\ \mathbf{e}_y \\ \mathbf{e}_z \end{pmatrix} \tag{2.4.4}$$

$$\begin{pmatrix} \mathbf{e}_{x_2} \\ \mathbf{e}_{y_2} \\ \mathbf{e}_{z_2} \end{pmatrix} = \begin{pmatrix} 1 & 0 & 0 \\ 0 & \cos\delta & \sin\delta \\ 0 & -\sin\delta & \cos\delta \end{pmatrix} \begin{pmatrix} \mathbf{e}_{x_1} \\ \mathbf{e}_{y_1} \\ \mathbf{e}_{z_1} \end{pmatrix} \tag{2.4.5}$$

Identifying $\mathbf{n}$ with the outward normal vector on the upper flap surface, it can be seen from Fig. 12 that

$$\mathbf{n} = \mathbf{e}_{y_2} \tag{2.4.6}$$

Then

$$\begin{aligned} \mathbf{n} &= \cos\delta\, \mathbf{e}_{y_1} + \sin\delta\, \mathbf{e}_{z_1} \\ &= -\sin\epsilon \sin\delta\, \mathbf{e}_x + \cos\delta\, \mathbf{e}_y + \sin\delta\cos\epsilon\, \mathbf{e}_z \end{aligned} \tag{2.4.7}$$

The free-stream velocity has two components such that

$$\mathbf{U} = U\, \mathbf{e}_x + U \tan\alpha\, \mathbf{e}_y \tag{2.4.8}$$

The component of the free-stream normal to the flap surface is then

$$U_n = \mathbf{U} \cdot \mathbf{n} = -U \sin\delta \sin\epsilon + U \tan\alpha \cos\delta \tag{2.4.9}$$

The condition that $U_n > 0$ is

$$\frac{\tan\alpha}{\sin\epsilon} > \tan\delta \tag{2.4.10}$$

The boundary shown in Fig. 13 represents the limit where the component of the free-stream velocity normal to the flap surface vanishes for $\epsilon = 15$ deg.

2.5 Lift-to-Drag Ratio for Flapped Delta Wings

In this section, a general formulation for the lift-to-drag ratio of a flapped delta wing is derived. Experiments[3,4,15,16] show significant increment of lift-to-drag ratio with flap deflection. The rotation of the leading edge flap about the flap hinge axis causes the normal vector to have a component opposite to the flight direction, as derived in the previous section. The first term in the last line in Eq. (2.4.7) indicates the forward component of the normal vector. The associated force component constitutes the thrust force and is of higher order than the other two, under the assumption that ϵ is small. The fact that flap deflection causes suppression of the vortical flow[6] can be interpreted as the vortical flow being confined to the vicinity of the leading edge flaps. Hence, most of the pressure peak region induced by the vortical flow is located on the flap surfaces. As a result, this higher order term can cause a considerable change in drag.

On the main wing the resultant force is normal to the wing surface. From Fig. 14 the lift and the drag components are

$$L_w = R_w \cos \alpha \tag{2.5.1a}$$

$$D_w = R_w \sin \alpha \tag{2.5.1b}$$

where R_w is the resultant force on the main wing.

On the flap surface there are all three components of force, as indicated by Eq. (2.4.7)

$$R_{F_x} = -R_F \sin \epsilon \sin \delta \tag{2.5.2a}$$

$$R_{F_y} = R_F \cos \delta \tag{2.5.2b}$$

$$R_{F_z} = R_F \cos \epsilon \sin \delta \tag{2.5.2c}$$

where R_F is the resultant force on the flap surface as shown in Fig. 14.

Since the R_{F_z} component is canceled by symmetry, only R_{F_x} and R_{F_y} contribute to lift and drag as illustrated in Fig. 14.

$$L_F = R_{F_y} \cos \alpha - R_{F_x} \sin \alpha \tag{2.5.3a}$$

$$D_F = R_{F_y} \sin \alpha + R_{F_x} \cos \alpha \tag{2.5.3b}$$

From Eqs. (2.5.2a) and (2.5.2b)

$$R_{F_x} = -\sin \epsilon \tan\delta \, R_{F_y} \tag{2.5.4}$$

From Eqs. (2.5.2),(2.5.3) and (2.5.4), the drag and lift on the flap is

$$L_F = R_{F_y} (\cos \alpha + \sin \epsilon \sin \alpha \tan \delta) \tag{2.5.5a}$$

$$D_F = R_{F_y} \sin \alpha \left(1 - \frac{\sin \epsilon}{\tan \alpha} \tan \delta\right) \tag{2.5.5b}$$

The total lift and drag are

$$L = R_w \cos\alpha + R_{F_y}(\cos \alpha + \sin \epsilon \sin \alpha \tan\delta) \tag{2.5.6}$$

$$D = \sin \alpha \left(R_w + R_{F_y} \left(1 - \frac{\sin \epsilon}{\tan \alpha} \tan \delta\right)\right) \tag{2.5.7}$$

For small α and ϵ these equations reduce to

$$L \simeq R_w + R_{F_y}(1 + \epsilon \alpha \tan\delta) \tag{2.5.8}$$

$$D \simeq \alpha \left(R_w + R_{F_y} \left(1 - \frac{\epsilon}{\alpha} \tan \delta\right)\right) \tag{2.5.9}$$

Eqs. (2.5.8) and (2.5.9) show the influence of the forward component of force on lift and drag. Due to this thrust component the lift increases by an amount of order α^2, while the drag is reduced by almost the same order as the drag itself. For moderate deflection angle, the lift-to-drag ratio is

$$\frac{L}{D} = \frac{1}{\alpha} \left[\left(1 + \frac{R_{F_y}}{R_w + R_{F_y}} \frac{\epsilon}{\alpha} \tan \delta\right) + O(\alpha^2)\right] \tag{2.5.10}$$

The second term within the parenthesis shows the influence of flap deflection on the lift-to-drag ratio. This amount is of order $1/\alpha$, the same as that of the lift-to-drag ratio without flap deflection.

Chapter 3

Straight-Feeding-Sheet Model

In this chapter the simplest vortex model for the delta wing vortical flow, first suggested by Legendre and implemented by Brown and Michael,[20,21] is chosen to investigate the qualitative trends of the effect of a leading edge flap on the aerodynamic characteristics of a low aspect ratio delta wing. This model simply assumes that the rolled-up shear layer consists of a straight vortex sheet and a singular vortex core and requires this singularity system to be force free in a global sense. The analysis is carried out in the cross-flow plane based on the steady-unsteady analogy developed in Section **2.2.2**. Complex representation of the cross-flow plane is utilized. The trace of the wing in the cross-flow plane is transformed into the horizontal axis of a transformed plane by the Schwarz-Christoffel transformation. The advantage of the conformal mapping is that the boundary condition on the wing surface is satisfied exactly.

3.1 Force Free Conditions

As explained in Section **2.3.2** the force free condition is imposed on each vortex+sheet system. Combined with Eqs. (2.3.1) and (2.3.3), the force free equation

given by Eq. (2.3.4) for small ϵ reduces to

$$\frac{U\,\epsilon}{k}\left(2\sigma'_{vj} - \sigma'_{sj}\right) = v_{vj} \tag{3.1.1}$$

where $()'$ indicates the length scale normalized with $a(x)$, and v_{vj} can be expressed as

$$\overline{v}_{vj} = \frac{d}{d\sigma}\left(F - \frac{i\Gamma_j}{2\pi}\log\left(\sigma - \sigma_{vj}\right)\right)_{\sigma\to\sigma_{vj}} \tag{3.1.2}$$

where F is the complex potential in the cross-flow plane, to be derived in the next section, and $\overline{(\,)}$ indicates the complex conjugate.

In the present case there is a system of four vortices fed by straight vortex sheets emanating from the leading edges and from the flap hinges. Since only the symmetrical configurations are treated, the analysis considers one half of the cross-flow plane, as shown in Fig. 15. Thus $\sigma'_s = i\,(k + (1-k)e^{i\delta})$ for the leading edge vortex and $\sigma'_s = i\,k$ for the hinge vortex. The force free conditions for both vortex systems are

$$\frac{U\epsilon}{k}\left(2\overline{\sigma}'_{vl} + i\left(k + (1-k)\,e^{-i\delta}\right)\right) = \frac{d}{d\sigma}\left(F - \frac{i\Gamma_l}{2\pi}\log\left(\sigma - \sigma_{vl}\right)\right)\Big|_{\sigma\to\sigma_{vl}} \tag{3.1.3}$$

$$\frac{U\epsilon}{k}\left(2\overline{\sigma}'_{vh} + ik\right) = \frac{d}{d\sigma}\left(F - \frac{i\Gamma_h}{2\pi}\log\left(\sigma - \sigma_{vh}\right)\right)\Big|_{\sigma\to\sigma_{vh}} \tag{3.1.4}$$

where subscripts l and h refer to the leading edge and hinge vortices respectively.

3.2 Schwarz-Christoffel Transformation

The derivation of the complex potential F is facilitated by transforming the trace

of the wing in the cross-flow plane, together with its line of symmetry, into the real axis of a transformed plane. To perform this transformation the Schwarz-Christoffel transformation is used. The mapping procedure is shown in Fig. 16.

The general form of Schwarz-Christoffel transformation is

$$\frac{d\sigma}{d\Theta} = A_1 \prod_{i=1}^{n} (\Theta - \Theta_i)^{\beta_i} \tag{3.2.1}$$

where $\Theta = \xi + i\vartheta$ is the complex representation of the transformed plane.

In integral form

$$\sigma = A_2 + A_1 \int_{\Theta_o}^{\Theta} \prod_{i=1}^{n} (\Theta - \Theta_i)^{\beta_i} \, d\Theta \tag{3.2.2}$$

where $\beta_i = \kappa_i/\pi - 1$, and κ_i is the external angle of the i^{th} vertex of the polygon, and Θ is the corresponding point of σ in the mapping plane. A_1 and A_2 are complex constants.

From Fig. 16

$$\begin{aligned} \kappa_1 &= \pi, \quad & \kappa_2 &= \pi/2, \quad & \kappa_3 &= \pi - \delta, \\ \kappa_4 &= 2\pi, \quad & \kappa_5 &= \pi + \delta, \quad & \kappa_6 &= \pi/2 \end{aligned} \tag{3.2.3}$$

then

$$\begin{aligned} \beta_1 &= 0, \quad & \beta_2 &= -1/2, \quad & \beta_3 &= -\delta/\pi, \\ \beta_4 &= 1, \quad & \beta_5 &= \delta/\pi, \quad & \beta_6 &= -1/2 \end{aligned} \tag{3.2.4}$$

Riemann's mapping theorem[88] establishes that the correspondence of two arbitrary points plus a far field condition can be imposed. Here two points are chosen arbitrarily as

$$\Theta_4 = 0 \tag{3.2.5a}$$

$$\Theta_o = \Theta_2 \tag{3.2.5b}$$

These conditions imply that the leading edge is transformed to the origin and the initial point of the integration is taken arbitrarily at Θ_2. Requiring that the velocity in both planes be equal at infinity gives another condition as

$$\left.\frac{d\sigma}{d\Theta}\right|_{\sigma\to\infty} = 1 \tag{3.2.6}$$

With Eqs. (3.2.5) and (3.2.6), the transformation function becomes

$$\sigma' = \int_{\Theta_2'}^{\Theta'} \frac{\Theta'}{\sqrt{(\Theta'-\Theta_2')\,(\Theta'-\Theta_6')}} \left(\frac{\Theta'-\Theta_5'}{\Theta'-\Theta_3'}\right)^{\delta/\pi} d\Theta' \tag{3.2.7}$$

where $()'$ indicates the length scale normalized with $a(x)$.

The real constants $\Theta_2', \Theta_3', \Theta_5', \Theta_6'$ can be obtained by matching the four corresponding points in the physical and the transformed plane

$$\sigma_3' = ik \quad \to \quad \Theta_3' \tag{3.2.8a}$$

$$\sigma_4' = ik\left(1+(1-k)\,e^{i\delta}\right) \quad \to \quad 0 \tag{3.2.8b}$$

$$\sigma_5' = ik \quad \to \quad \Theta_5' \tag{3.2.8c}$$

$$\sigma_6' = 0 \quad \to \quad \Theta_6' \tag{3.2.8d}$$

Application of Eqs. (3.2.8 a,b,c,d) to the transformation function (3.2.7) gives

$$k + \int_{\Theta_2'}^{\Theta_3'} \frac{\xi'}{\sqrt{(\Theta_6'-\xi')(\xi'-\Theta_2')}} \left(\frac{\Theta_5'-\xi'}{\Theta_3'-\xi'}\right)^{\delta/\pi} d\xi' = 0 \tag{3.2.9a}$$

$$1 - k + \int_{\Theta_3'}^{0} \frac{\xi'}{\sqrt{(\Theta_6'-\xi')(\xi'-\Theta_2')}} \left(\frac{\Theta_5'-\xi'}{\xi'-\Theta_3'}\right)^{\delta/\pi} d\xi' = 0 \tag{3.2.9b}$$

$$1 - k - \int_{0}^{\Theta_5'} \frac{\xi'}{\sqrt{(\Theta_6'-\xi')(\xi'-\Theta_2')}} \left(\frac{\Theta_5'-\xi'}{\xi'-\Theta_3'}\right)^{\delta/\pi} d\xi' = 0 \tag{3.2.9c}$$

$$k - \int_{\Theta_5'}^{\Theta_6'} \frac{\xi'}{\sqrt{(\Theta_6'-\xi')(\xi'-\Theta_2')}} \left(\frac{\xi'-\Theta_5'}{\xi'-\Theta_3'}\right)^{\delta/\pi} d\xi' = 0 \tag{3.2.9d}$$

This system is solved numerically for $\Theta_2', \Theta_3', \Theta_5', \Theta_6'$ using the Wolfe method,[89] as described in Appendix 1.

3.3 Mathematical Procedure

From Fig. 16 the complex potential in the transformed plane is the sum of the potentials of a uniform velocity and that of four vortices, two of which are the image vortices needed to satisfy the boundary condition on the wing surface. Then the complex potential in the transformed plane is

$$F(\Theta) = U\alpha\Theta + \frac{i\Gamma_l}{2\pi}\log\left(\frac{\Theta-\Theta_{vl}}{\Theta-\overline{\Theta}_{vl}}\right) + \frac{i\Gamma_h}{2\pi}\log\left(\frac{\Theta-\Theta_{vh}}{\Theta-\overline{\Theta}_{vh}}\right) \tag{3.3.1}$$

and the complex velocity in the physical plane is

$$\begin{aligned}\overline{v} &= \frac{dF}{d\sigma} = \frac{dF}{d\Theta}\frac{d\Theta}{d\sigma} \\ &= \left[U\alpha + \frac{i\Gamma_l}{2\pi}\left(\frac{1}{\Theta-\Theta_{vl}} - \frac{1}{\Theta-\overline{\Theta}_{vl}}\right)\right. \\ &\qquad \left. + \frac{i\Gamma_h}{2\pi}\left(\frac{1}{\Theta-\Theta_{vh}} - \frac{1}{\Theta-\overline{\Theta}_{vh}}\right)\right]\frac{d\Theta}{d\sigma}\end{aligned} \tag{3.3.2}$$

where

$$\frac{d\Theta}{d\sigma} = \frac{\sqrt{(\Theta-\Theta_6)(\Theta-\Theta_2)}}{\Theta}\left(\frac{\Theta-\Theta_3}{\Theta-\Theta_5}\right)^{\delta/\pi} \tag{3.3.3}$$

According to Eq. (3.3.3) the velocity becomes singular at the leading edge, $\Theta = 0$, and at the flap hinge, $\Theta = \Theta_5$. To avoid this singularity, a Kutta condition is imposed at these two points. The two equations for the Kutta condition are

$$U\alpha + \frac{i\Gamma_l}{2\pi}\left(\frac{1}{\overline{\Theta}_{vl}} - \frac{1}{\Theta_{vl}}\right) + \frac{i\Gamma_h}{2\pi}\left(\frac{1}{\overline{\Theta}_{vh}} - \frac{1}{\Theta_{vh}}\right) = 0 \tag{3.3.4}$$

$$U\alpha + \frac{i\Gamma_l}{2\pi}\left(\frac{1}{\Theta_5-\Theta_{vl}} - \frac{1}{\Theta_5-\overline{\Theta}_{vl}}\right) + \frac{i\Gamma_h}{2\pi}\left(\frac{1}{\Theta_5-\Theta_{vh}} - \frac{1}{\Theta_5-\overline{\Theta}_{vh}}\right) = 0 \tag{3.3.5}$$

With the complex potential F in Eq. (3.3.1), the force free conditions given by Eqs. (3.1.3) and (3.1.4) become

$$\begin{aligned}
&\frac{U\epsilon}{k}\left(2\overline{\sigma}'_{vl} + i\left(k+(1-k)\,e^{-i\delta}\right)\right) = \\
&\left(U\alpha - \frac{i\Gamma_l}{2\pi}\frac{1}{\Theta_{vl}-\overline{\Theta}_{vl}} + \frac{i\Gamma_h}{2\pi}\left(\frac{1}{\Theta_{vl}-\Theta_{vh}} - \frac{1}{\Theta_{vl}-\overline{\Theta}_{vh}}\right)\right)\times \\
&\left(\frac{\sqrt{(\Theta_{vl}-\Theta_6)(\Theta_{vl}-\Theta_2)}}{\Theta_{vl}}\left(\frac{\Theta_{vl}-\Theta_3}{\Theta_{vl}-\Theta_5}\right)^{\delta/\pi}\right) \\
&+ \frac{i\Gamma_l}{2\pi}\frac{d}{d\sigma}\Big(\log(\Theta-\Theta_{vl}) - \log(\sigma-\sigma_{vl})\Big)_{\sigma\to\sigma_{vl}}
\end{aligned} \tag{3.3.6}$$

for the leading edge vortex system, and

$$\begin{aligned}
&\frac{U\epsilon}{k}\left(2\overline{\sigma}'_{vh} + ik\right) = \\
&\left(U\alpha + \frac{i\Gamma_l}{2\pi}\left(\frac{1}{\Theta_{vh}-\Theta_{vl}} - \frac{1}{\Theta_{vh}-\overline{\Theta}_{vl}}\right) - \frac{i\Gamma_h}{2\pi}\frac{1}{\Theta_{vh}-\overline{\Theta}_{vh}}\right)\times \\
&\left(\frac{\sqrt{(\Theta_{vh}-\Theta_6)(\Theta_{vh}-\Theta_2)}}{\Theta_{vh}}\left(\frac{\Theta_{vh}-\Theta_3}{\Theta_{vh}-\Theta_5}\right)^{\delta/\pi}\right) \\
&+ \frac{i\Gamma_h}{2\pi}\frac{d}{d\sigma}\Big(\log(\Theta-\Theta_{vh}) - \log(\sigma-\sigma_{vh})\Big)_{\sigma\to\sigma_{vh}}
\end{aligned} \tag{3.3.7}$$

for the hinge vortex system.

Combining Eqs. (3.3.6) and (3.3.7) with Eqs. (3.3.4) and (3.3.5), and normalizing all the length scales with $a(x)$, the following system of two complex equations for

the vortex positions Θ_{vl} and Θ_{vh} (or σ_{vl} and σ_{vh}) is obtained

$$\frac{\epsilon}{k\alpha}\left(2\overline{\sigma}'_{vl}+i\left(k+(1-k)\,e^{-i\delta}\right)\right) =$$

$$\left(1-\frac{D-B}{CB-AD}\frac{1}{\Theta'_{vl}-\overline{\Theta}'_{vl}}+\frac{C-A}{CB-AD}\left(\frac{1}{\Theta'_{vl}-\Theta'_{vh}}-\frac{1}{\Theta'_{vl}-\overline{\Theta}'_{vh}}\right)\right)\times$$

$$\left(\frac{d\sigma'}{d\Theta'}\right)\Big|_{\sigma'=\sigma'_{vl}}+\frac{D-B}{CB-AD}\frac{d}{d\sigma'}\left(\log\left(\Theta'-\Theta'_{vl}\right)-\log\left(\sigma'-\sigma'_{vl}\right)\right)\Big|_{\sigma'\to\sigma'_{vl}} \tag{3.3.8a}$$

$$\frac{\epsilon}{k\alpha}\left(2\overline{\sigma}'_{vh}+ik\right) =$$

$$\left(1+\frac{D-B}{CB-AD}\left(\frac{1}{\Theta'_{vh}-\Theta'_{vl}}-\frac{1}{\Theta'_{vh}-\overline{\Theta}'_{vl}}\right)-\frac{C-A}{CB-AD}\frac{1}{\Theta'_{vh}-\overline{\Theta}'_{vh}}\right)\times$$

$$\left(\frac{d\sigma'}{d\Theta'}\right)\Big|_{\sigma'=\sigma'_{vh}}-\frac{A-C}{CB-AD}\frac{d}{d\sigma'}\left(\log\left(\Theta'-\Theta'_{vh}\right)-\log\left(\sigma'-\sigma'_{vh}\right)\right)\Big|_{\sigma'\to\sigma'_{vh}} \tag{3.3.8b}$$

where

$$A = \frac{1}{\overline{\Theta}'_{vl}}-\frac{1}{\Theta'_{vl}} \tag{3.3.9a}$$

$$B = \frac{1}{\overline{\Theta}'_{vh}}-\frac{1}{\Theta'_{vh}} \tag{3.3.9b}$$

$$C = \frac{1}{\Theta'_5-\Theta'_{vl}}-\frac{1}{\Theta'_5-\overline{\Theta}'_{vl}} \tag{3.3.9c}$$

$$D = \frac{1}{\Theta'_5-\Theta'_{vh}}-\frac{1}{\Theta'_5-\overline{\Theta}'_{vh}} \tag{3.3.9d}$$

System (3.3.8) is solved using the Newton-Raphson method, as described in Appendix 2.

In the absence of flaps the only governing parameter would be the ratio of ϵ/α. In the present case two additional parameters, δ and k, are included in the group $\epsilon/(k\ \alpha)$, as indicated in Eqs. (3.3.8a,b). The flap deflection angle δ does not appear explicitly but through the transformation parameters $\Theta_2, \Theta_3, \Theta_5, \Theta_6$, which are functions of δ and k.

With the vortex positions known, the vortex strengths can be obtained from

$$\frac{i\Gamma_l'}{2\pi} = \frac{D-B}{CB-AD}\,\alpha \tag{3.3.10a}$$

$$\frac{i\Gamma_h'}{2\pi} = \frac{A-C}{CB-AD}\,\alpha \tag{3.3.10b}$$

where $\Gamma' = \Gamma/(Ua(x))$

3.4 Aerodynamic Forces

3.4.1 Resultant Force

To evaluate the lift-to-drag ratio for a flapped delta wing, as derived in Section **2.5**, the pressure must be calculated first. For small α and using Eq. (2.3.1), the unsteady pressure coefficient given by Eq. (2.2.19b) becomes

$$C_p = \alpha^2 - 2\frac{v_x}{U} - \left(\frac{v_y}{U}\right)^2 - \left(\frac{v_z}{U}\right)^2 \tag{3.4.1}$$

where the v_y and v_z components are given by

$$\begin{aligned}\frac{v_y}{U} - i\frac{v_z}{U} &= \frac{1}{U}\frac{dF}{d\sigma} \\ &= \left[\left(\alpha + \frac{i\Gamma_l'}{2\pi}\left(\frac{1}{\Theta' - \Theta_{vl}'} - \frac{1}{\Theta' - \overline{\Theta}_{vl}'}\right) + \frac{i\Gamma_h'}{2\pi}\left(\frac{1}{\Theta' - \Theta_{vh}'} - \frac{1}{\Theta' - \overline{\Theta}_{vh}'}\right)\right) \times \right. \\ &\quad \left. \left(\frac{\sqrt{(\Theta' - \Theta_6')\,(\Theta' - \Theta_2')}}{\Theta'}\left(\frac{\Theta' - \Theta_3'}{\Theta' - \Theta_5'}\right)^{\delta/\pi}\right)\right]\end{aligned} \tag{3.4.2}$$

Thus

$$\frac{v_y}{U} = \Re\left(\frac{1}{U}\frac{dF}{d\sigma}\right) \tag{3.4.3}$$

$$\frac{v_z}{U} = -\Im\left(\frac{1}{U}\frac{dF}{d\sigma}\right) \tag{3.4.4}$$

where $\Re$ and $\Im$ represent the real and imaginary part of a complex function.

The v_x component is best obtained from the conical expression of the velocity potential in Eq. (2.2.2). In terms of rectangular coordinates the potential can be written as

$$\Phi_c = x\,(U + U\alpha\hat{y} + \varphi_c(\hat{y}, \hat{z})) \tag{3.4.5}$$

where

$$\hat{y} = \frac{y}{x} \qquad \hat{z} = \frac{z}{x} \tag{3.4.6}$$

Then the perturbation velocity in axial direction is

$$\begin{aligned}\frac{v_x}{U} &= \alpha + \varphi_c - \hat{y}\frac{\partial\varphi_c}{\partial\hat{y}} - \hat{z}\frac{\partial\varphi_c}{\partial\hat{z}} \\ &\simeq \alpha + \varphi_u - \hat{y}\frac{v_y}{U} - \hat{z}\frac{v_z}{U}\end{aligned} \tag{3.4.7}$$

Introducing the complex potential F this becomes

$$\frac{v_x}{U} = \frac{\epsilon}{k}\Re\left[\alpha\Theta' + \frac{i\Gamma'_l}{2\pi}\log\left(\frac{\Theta' - \Theta'_{vl}}{\Theta' - \overline{\Theta}'_{vl}}\right) + \frac{i\Gamma'_h}{2\pi}\log\left(\frac{\Theta' - \Theta'_{vh}}{\Theta' - \overline{\Theta}'_{vh}}\right) - y'\frac{v_y}{U} - z'\frac{v_z}{U}\right] \tag{3.4.8}$$

The presence of the feeding sheet induces a discontinuity in the v_x component of the velocity, leading to the treatment of branch cuts, as shown in Fig. 17.

The resultant force is given by

$$R = \int_{\text{each surface}} p\, d\sigma \tag{3.4.9}$$

3.4.2 Normal Force

As mentioned in the Introduction, experiments[3,15,16] have shown that the lift decreases with flap deflection due to the suppression of the vortical flow. This phenomenon can be best observed by considering the lift contribution of the vortex systems. For small α and ϵ the lift is related to the total force component normal to the wing surface

$$L \simeq N + R_{Fy}\,\epsilon\alpha\,\tan\delta \tag{3.4.10}$$

where N is the total force acting normal to the free-stream and R_{Fy} is the y-component of the force acting on the flap, as illustrated in Fig. 14.

The second term represent the contribution to the total lift of the thrust component of force, which is of order α^2. Thus,

$$L \simeq N \tag{3.4.11}$$

The total normal force can be calculated by considering the momentum flux across the cross-flow plane

$$N = -\rho U \int\int \left(\frac{\partial \Phi}{\partial y} - U\alpha \right) dydz \tag{3.4.12}$$

Applying Stokes' theorem

$$N = -\rho U \oint \Phi \, dz \tag{3.4.13}$$

The integration path is taken around the wing surface including all the singularities. In terms of the complex potential and the real stream function

$$N = -\rho U \, \Im \oint (F - i\,\Psi)\, d\sigma \tag{3.4.14}$$

Since the contour is a streamline

$$N = -\rho U \, \Im \oint (F \, d\sigma) \tag{3.4.15}$$

Substituting for F

$$\begin{aligned} N = -\rho U \, \Im \oint \Bigg[U\alpha\Theta + \frac{i\Gamma_l}{2\pi} \log\left(\frac{\Theta - \Theta_{vl}}{\Theta - \overline{\Theta}_{vl}} \right) \\ + \frac{i\Gamma_h}{2\pi} \log\left(\frac{\Theta - \Theta_{vh}}{\Theta - \overline{\Theta}_{vh}} \right) \Bigg] \frac{d\sigma}{d\Theta} \, d\Theta \end{aligned} \tag{3.4.16}$$

To perform the integral of the parts containing logarithmic terms, the path can be altered by taking a circle of infinite radius, as shown in Fig. 17, since there are no singularities in the far field, where $d\sigma/d\Theta = 1$

$$\begin{aligned} &\oint \left(\frac{i\Gamma_l}{2\pi} \log\left(\frac{\Theta - \Theta_{vl}}{\Theta - \overline{\Theta}_{vl}} \right) + \frac{i\Gamma_h}{2\pi} \log\left(\frac{\Theta - \Theta_{vh}}{\Theta - \overline{\Theta}_{vh}} \right) \right) \frac{d\sigma}{d\Theta} d\Theta \\ &= \oint_{|\Theta|=\infty} \left(\frac{i\Gamma_l}{2\pi} \log\left(\frac{\Theta - \Theta_{vl}}{\Theta - \overline{\Theta}_{vl}} \right) + \frac{i\Gamma_h}{2\pi} \log\left(\frac{\Theta - \Theta_{vh}}{\Theta - \overline{\Theta}_{vh}} \right) \right) d\Theta \end{aligned} \tag{3.4.17}$$

In the transformed plane, the normal force arising from the logarithmic terms does not depend explicitly on the wing trace geometry, but implicitly through the vortices' positions and strengths. This equation shows that the normal force is just the sum of the rate change of impulse of two pairs of vortices. Then the result of the integration of the logarithmic terms could be simply obtained by considering the impulse of a pair of vortices, or by integrating along the branch lines as shown in Fig. 17. Following the second approach gives

$$\begin{aligned}
&\oint_{|\Theta|\to\infty} \frac{i\Gamma_l}{2\pi}\left(\log\left(\Theta-\Theta_{vl}\right)-\log\left(\Theta-\overline{\Theta}_{vl}\right)\right)d\Theta \\
&= \frac{i\Gamma_l}{2\pi}\left[\int_{\overline{\Theta}_{vl}}^{\Theta_{vl}} \log\left(\Theta-\Theta_{vl}\right)|_p-\log\left(\Theta-\overline{\Theta}_{vl}\right)|_p-i\,2\pi\;d\Theta\right. \\
&\qquad\left.+\int_{\Theta_{vl}}^{\overline{\Theta}_{vl}} \log\left(\Theta-\Theta_{vl}\right)|_p-\log\left(\Theta-\overline{\Theta}_{vl}\right)|_p\;d\Theta\right] \\
&= \Gamma_l\;\left(\Theta_{vl}-\overline{\Theta}_{vl}\right)
\end{aligned} \tag{3.4.18}$$

Then the normal force originating from the logarithmic terms is

$$N_V = \rho U\,\Im\Big(\Gamma_l\left(\Theta_{vl}+\overline{\Theta}_{vl}\right)+\Gamma_h\left(\Theta_{vh}-\overline{\Theta}_{vh}\right)\Big) \tag{3.4.19}$$

This force is associated with the separated flow field about the wing.

The component of normal force from the the first term in Eq. (3.4.16) has a singularity at infinity. This component could be identified with the force produced by the wing if the flow were attached. Integrating along the wing trace, as shown

in Fig. 18, there results

$$
\begin{aligned}
-\frac{N_A}{\rho U^2 \alpha} &= \oint \frac{\Theta^2}{\sqrt{(\Theta-\Theta_6)(\Theta-\Theta_2)}} \left(\frac{\Theta-\Theta_5}{\Theta-\Theta_3}\right)^{\delta/\pi} d\Theta \\
&= 2\left(\int_{\Theta_2}^{\Theta_3} + \int_{\Theta_5}^{\Theta_6} + \cos 2\delta \int_{\Theta_3}^{\Theta_5}\right) \times \\
&\qquad \frac{\Theta^2}{\sqrt{(\Theta-\Theta_6)(\Theta-\Theta_2)}}\bigg|_p \left(\frac{\Theta-\Theta_5}{\Theta-\Theta_3}\right)^{\delta/\pi}\bigg|_p d\Theta
\end{aligned}
\tag{3.4.20}
$$

where the subscript p represents the principal value (i.e., all values are calculated in the same Riemann surface.)

Then the total normal force is

$$
\begin{aligned}
N &= \rho U \Im \left(\Gamma_l(\Theta_{vl} - \overline{\Theta}_{vl}) + \Gamma_h(\Theta_{vh} - \overline{\Theta}_{vh})\right) \\
&\quad - \rho U^2 \alpha \Im \oint \frac{\Theta^2}{\sqrt{(\Theta-\Theta_6)(\Theta-\Theta_2)}} \left(\frac{\Theta-\Theta_5}{\Theta-\Theta_3}\right)^{\delta/\pi} d\Theta
\end{aligned}
\tag{3.4.21}
$$

The normal force is composed of two parts; the normal force from the equivalent attached flow and that from the separated flow.

Dividing this total normal force by the dynamic pressure $\rho U^2/2$ and the total wing area $ka(x)^2/\epsilon$, the normal force coefficient can be obtained as

$$
C_N = \frac{\epsilon}{k}\left(C_{N_V} + C_{N_A}\right) \tag{3.4.22}
$$

where C_{N_V} and C_{N_A} represent the contribution to the normal force of the vortex systems and the attached-type flow respectively. Hence

$$
C_{N_V} = \Im\left(2\Gamma_l'(\Theta_{vl}' - \overline{\Theta}_{vl}') + 2\Gamma_h'(\Theta_{vh}' - \overline{\Theta}_{vh}')\right) \tag{3.4.23}
$$

$$C_{N_A} = -4\alpha\,\Im\left(\int_{\Theta'_2}^{\Theta'_3} + \int_{\Theta'_5}^{\Theta'_6} + \cos 2\delta \int_{\Theta'_3}^{\Theta'_5}\right)\times \frac{\Theta'^2}{\sqrt{(\Theta'-\Theta'_6)(\Theta'-\Theta'_2)}}\left(\frac{\Theta'-\Theta'_5}{\Theta'-\Theta'_3}\right)^{\delta/\pi}\Bigg|_p d\Theta' \tag{3.4.24}$$

Here all the values of the integrand are principal values. Eq. (3.4.24) shows explicitly the effect of the flap angle on the normal force through the term $\cos 2\delta$ in the integration over the flap surface, while the transformation coefficients $\Theta'_2, \Theta'_3, \Theta'_5, \Theta'_6$ depend implicitly on δ and k. The region from Θ_3 to Θ_5 is the flap surface.

3.5 Numerical Implementation

3.5.1 Integration at Singular Points

In Eqs. (3.2.9 a,b,c,d), from which the transformation coefficients $\Theta_2, \Theta_3, \Theta_5, \Theta_6$ are calculated, the integrands are singular at the points $\xi = \Theta_2, \Theta_3, \Theta_6$. To perform the numerical integration, the integrand is expanded to 1st order in Taylor series about those points. For example, at $\xi = \Theta_2$

$$\begin{aligned}
&\int_{\Theta_2}^{\Theta_2+\varepsilon} \frac{\xi}{\sqrt{(\Theta_6-\xi)(\xi-\Theta_2)}}\left(\frac{\Theta_5-\xi}{\Theta_3-\xi}\right)^{\delta/\pi} d\xi \\
&= \int_0^{\varepsilon} \frac{\zeta+\Theta_2}{\sqrt{\zeta(\Theta_6-\zeta-\Theta_2)}}\left(\frac{\Theta_5-\zeta-\Theta_2}{\Theta_3-\zeta-\Theta_2}\right)^{\delta/\pi} d\zeta \\
&\simeq \frac{\Theta_2}{\sqrt{\Theta_6-\Theta_2}}\left(\frac{\Theta_5-\Theta_2}{\Theta_3-\Theta_2}\right)^{\delta/\pi}\int_0^{\varepsilon}\frac{1}{\sqrt{\zeta}}d\zeta \\
&= \frac{2\Theta_2}{\sqrt{\Theta_6-\Theta_2}}\left(\frac{\Theta_5-\Theta_2}{\Theta_3-\Theta_2}\right)^{\delta/\pi}\sqrt{\varepsilon}
\end{aligned} \tag{3.5.1}$$

where $\zeta = \xi - \Theta_2$.

Romberg integration is used on the rest of the range.[90]

3.5.2 Integration Path for Calculating Vortex Positions

During the numerical procedure for calculating the vortex positions in the physical plane through the mapping function (3.2.7), by solving Eqs. (3.3.8a,b), taking the integration path as a straight line connecting Θ_2 with the assumed vortex position, as shown in the broken line in Fig. 19, causes the following problem: When the vortex position is very close to the real axis in the transformed plane, which is the case when α is small or δ is large, the integration path passes close to the singular points Θ_3 and Θ_6. To avoid this possible numerical singularity, the integration path is taken in the following way:

$$\Theta_2 \quad \rightarrow \quad \Theta_2 + i\,2 \quad \rightarrow \quad \text{assumed} \quad \Re\,\Theta_v + i\,2 \quad \rightarrow \quad \text{assumed} \quad \Theta_v \tag{3.5.2}$$

The maximum imaginary value, taken as 2, is large enough to calculate the vortex positions.

3.5.3 Velocity at the Vortex Position

Eqs. (3.3.8a,b) contain terms of the form

$$\frac{d}{d\sigma}\Big(\log(\Theta - \Theta_v) - \log(\sigma - \sigma_v)\Big)_{\sigma \rightarrow \sigma_v} \tag{3.5.3}$$

which can be written as

$$\frac{d}{d\Theta}\Big(\log(\Theta - \Theta_v) - \log(\sigma - \sigma_v)\Big)_{\Theta \rightarrow \Theta_v} \frac{d\Theta}{d\sigma}\Big|_{\sigma_v} \tag{3.5.4}$$

In calculating this value numerically, a finite difference scheme is employed as follows

$$\begin{aligned}
&\left[\frac{\log(\Theta_v+\Delta\Theta-\Theta_v)-\log(\Theta_v-\Delta\Theta-\Theta_v)}{2\Delta\Theta}\right.\\
&\qquad\left.-\frac{\log\Big(\sigma(\Theta_v+\Delta\Theta)-\sigma(\Theta_v)\Big)-\log\Big(\sigma(\Theta_v-\Delta\Theta)-\sigma(\Theta_v)\Big)}{2\Delta\Theta}\right]\frac{d\Theta}{d\sigma}\Big|_{\Theta_v}\\
&=\left[\left(\log\frac{\Theta_v+\Delta\Theta-\Theta_v}{\sigma(\Theta_v+\Delta\Theta)-\sigma_v}-\log\frac{\Theta_v-\Delta\Theta-\Theta_v}{\sigma(\Theta_v-\Delta\Theta)-\sigma_v}\right)\Big/(2\Delta\Theta)\right]\frac{d\Theta}{d\sigma}\Big|_{\Theta_v}\\
&=\left(\left(\log\frac{\sigma_v-\sigma(\Theta_v-\Delta\Theta)}{\sigma(\Theta_v+\Delta\Theta)-\sigma_v}\right)\Big/(2\Delta\Theta)\right)\frac{d\Theta}{d\sigma}\Big|_{\Theta_v}
\end{aligned}\tag{3.5.5}$$

3.6 Results

3.6.1 Conformal Mapping Parameters

The following table shows the transformation coefficients $\Theta_2', \Theta_3', \Theta_5', \Theta_6'$ for varying flap deflection angle with $k = 0.6$ and $\epsilon = 15$ deg.

δ (deg.)	Θ_2'	Θ_3'	Θ_5'	Θ_6'
40	-0.6369	-0.5160	0.9785	1.301
32	-0.7091	-0.5722	0.9531	1.251
24	-0.7824	-0.6284	0.9183	1.195
16	-0.8558	-0.6836	0.8794	1.134
8	-0.9286	-0.7371	0.8362	1.069
2	-0.9822	-0.7756	0.8010	1.018

The results shows that as $\delta \to 0$, $\Theta_2' \to -1$ and $\Theta_6' \to 1$, which correspond to the Brown and Michael case.

3.6.2 Aerodynamic Forces; a Comparison with Experimental Results

To compare with the experimental results of Ref. 14 a wing with $\epsilon = 15$ deg. and $k = 0.6$ was chosen. The angle of attack α was varied from 0 deg. to 20 deg.

Fig. 20 and 21 show the increment of lift on the main wing and flap respectively. The abrupt departure from experiments observed at about 12 deg. appears to suggest that the trailing edge effects begin to be significant for the experiments.

Fig. 22 depicts the total lift change. Again, the sudden departure from the experimental trends may indicate that those measurements were affected by the trailing edge effect.

Fig. 23 shows the drag on the main wing. It can be seen that the vortex model overestimates the drag, particularly at higher angles of attack.

Fig. 24 shows the drag on the flap. Notice that this component of drag can reach negative values. This is due to the forward force component discussed above.

Fig. 25 shows the evolution of the resultant drag. The negative values of drag arise from the conical assumptions, where no trailing vortices and associated drag are considered.

Fig. 26 shows the change in the L/D. No experimental values were available for a comparable geometry of the wing. The no-deflection case is included for comparison.

Fig. 27 shows the positions of vortices for varying flap deflection. For flap deflection less than 18 deg. the hinge vortex almost disappears. The vortex

positions in the physical plane are shown in Fig. 28. It can be observed that that flap deflection causes the hinge vortex to move away from the surface and the leading edge vortex to approach the surface for the given conditions.

Fig. 29 describes the strength of both vortices as functions of flap deflection. Flap deflection strengthens the hinge vortex and weakens the leading edge vortex. The strength of leading edge vortex reduces by a half for a 30 deg. flap deflection.

Fig. 30 shows the different components of normal force. It is noticed that flap deflection acts primarily on the leading edge vortex component of the normal force. The hinge vortex has a negligible effect on the total force.

Fig. 31 and 32 show the pressure distribution obtained from the straight-feeding-sheet model, compared with experiment.[3] Experimental data are chosen at 37% of the chord from the apex to minimized the effects of trailing edge. Without flap deflection the prediction is reasonable but shows overprediction of pressure and the peak is shifted toward the leading edges. The pressure distribution with 15 deg. flap deflection angle shows unrealistic pressure peak at the leading edges. The unrealistic pressure peak is due to the vortex position, which is located very close to the wing surface.

3.7 Summary

Even with the crudeness of the vortex model, the two major phenomena due to flap deflection, increment of lift-to-drag ratio and suppression of vortical flow, are qualitatively observed. The leading edge vortex pair is much stronger and is responsible for most of the lift and drag changes that take place during flap deflection. In agreement with experimental evidence, it is found that flap deflection causes a

decrease of lift and drag, and an increase of the lift-to-drag ratio. The rapid reduction in drag is attributable to a thrust force component developed by the flaps, while the main reason for the lift reduction is the partial suppression of the leading edge vortical system. There is agreement with experiments in the general trends.

This model does not yield satisfactory vortex positions, which result in inaccurate pressure distribution. The simplified vortex model used here leads to an overprediction of lift and drag forces. For better prediction of pressure distribution and force, a improved vortex model is required. This is the objective of the vortex cloud model, discussed in the next chapter.

Chapter 4

Vortex Cloud Model

Due to the crudeness of the vortex model only global quantities, such as lift and drag, were evaluated in Chapter **3**. In this chapter a vortex cloud method is adopted to investigate the pressure distribution and the shear layer structures. Combined with the steady-unsteady analogy developed in Section **2.2.2**, the vortex cloud method leads to a numerically efficient methodology with good definition of shear layers. The shear layers are replaced by a cloud of discrete vortices having finite core size, and the core region of the vortical flow is modeled with a single vortex. A boundary element method is employed to represent the trace of the wing in the cross-flow plane. The various aspects of numerical implementation, such as core modeling, merging of vortices and integration methods, are investigated.

4.1 Vortex Model

The vortex cloud method simulating 2-D separated flow fields consists in tracing the trajectories of a large number of discrete vortices. A problem facing methods of this type is the large velocities induced by neighboring vortices. Some researchers employ vortices with finite core size to avoid large mutually induced velocities,[60,62–65]

while others redistribute the vortices at each time step so as to avoid logarithmically infinite velocities.[66] In this study vortices having finite core size are employed for two reasons. The redistribution of the vortices at each time step is computationally expensive, and causes the disappearance of the coherent structures shown in Fig. 6. This disappearance occurs because the redistribution technique prevents the overriding of vortices.

The rolled-up shear layers are replaced by a cloud of discrete vortices, each of which is generated from the separation point at a time step. Chorin[62] first introduced the concept of vortices of finite core size in the cloud approach, so that all of the rotational and viscous effects can be assumed to take place in the core, while outside of this core the flow field is governed by potential theory. By a proper distribution of vorticity within the core, the infinite velocity induced by neighboring vortices can be avoided. Using this concept, the vorticity distribution, which appears in the right hand side of Eq. (2.3.7), can be represented as:

$$\omega(\mathbf{x},t) \;=\; \sum_{i=1}^{N} \Gamma_i \; \chi_i(|\mathbf{x}-\mathbf{x}_i(t)|) \tag{4.1.1}$$

where χ_i is the vorticity distribution function satisfying the normalizing condition

$$\int_0^{\infty} \chi_i(|\mathbf{x}|)\; d\mathbf{x} \;=\; 1 \tag{4.1.2}$$

In the case of point vortices, the functions χ_i become the dirac-delta function $\delta(|\mathbf{x}-\mathbf{x}_i|)$. Introducing a core radius ς_i, χ_i can be written as:

$$\chi_i(|\mathbf{x}-\mathbf{x}_i|) \;=\; \frac{1}{{\varsigma_i}^2}\, G\Big(\frac{|\mathbf{x}-\mathbf{x}_i|}{\varsigma_i}\Big) \tag{4.1.3}$$

where G is a shape function common to all vortices.

The velocity induced by the vorticity distribution $\Gamma_i \chi_i(|\mathbf{x} - \mathbf{x}_i(t)|)$ is

$$\mathbf{u}(\mathbf{x},t) = -\frac{1}{2\pi} \frac{(\mathbf{x}-\mathbf{x}_i) \times \mathbf{e}_x \, \Gamma_i \, g\left(\frac{|\mathbf{x}-\mathbf{x}_i|}{\varsigma_i}\right)}{|\mathbf{x}-\mathbf{x}_i|^2} \tag{4.1.4}$$

where

$$g\left(\frac{|\mathbf{x}-\mathbf{x}_i|}{\varsigma_i}\right) = 2\pi \int_0^{\frac{|\mathbf{x}-\mathbf{x}_i|}{\varsigma_i}} G\left(\frac{|\mathbf{x}'-\mathbf{x}_i|}{\varsigma_i}\right) \frac{|\mathbf{x}'-\mathbf{x}_i|}{\varsigma_i} \, d\left(\frac{|\mathbf{x}'-\mathbf{x}_i|}{\varsigma_i}\right) \tag{4.1.5}$$

The following vorticity distribution G and the associated velocity distribution used in this study were derived by Spalart[63]

$$\pi \, G = \begin{cases} 0 & \varrho \geq 1 \\ 3(\varrho^2 - 1)^2 & \varrho \leq 1 \end{cases} \tag{4.1.6}$$

$$\frac{2\pi \, u \, \varsigma_i}{\Gamma_i} = \begin{cases} \frac{1}{\varrho} & \varrho \geq 1 \\ \varrho \, (3 - 3\,\varrho^2 + \varrho^4) & \varrho \leq 1 \end{cases} \tag{4.1.7}$$

where $\varrho = |\mathbf{x} - \mathbf{x}_i| / \varsigma_i$.

It can be assumed that the most desirable core vorticity distribution would be of the form $1 - \exp(-\varrho^2)$, since this corresponds to an isolated vortex in a viscous fluid. However, the computational time and effort would be considerably larger than in the case of distributions (4.1.6) and (4.1.7), and as shown by A. Leonard,[67] for fixed core size, differences in the velocity representation have a small influence on global flow features. The distribution used here, shown in Fig. 33, resemble a Gaussian distribution and was chosen as a compromise between computational efficiency and truthful representation of vorticity diffusion. Accordingly, Prandtl's relationship[78] for core size,

$$\varsigma_i^2 \propto t \tag{4.1.8}$$

valid for a Gaussian distribution of vorticity, is used together with Eqs. (4.1.6) and (4.1.7).

4.2 Kutta Condition

In this approach, a new discrete vortex is generated from the separation point at each time step such that the flow field including this new vortex satisfies an appropriate Kutta condition at the separation point. For an unsteady flow, as opposed to a steady flow, the vorticity is continuously supplied to the surrounding fluid from a separation point such that the strength and the space distribution of the shed vorticity allow for pressure continuity to be satisfied.[56–59] Such strength and space distribution are functions of the velocity on each side of the vortex sheet.[57] From Fig. 34a, Bernoulli's equation on each side of the vortex sheet is

$$H_1 = \frac{1}{2}\rho\, {u_1}^2 + p_1 + \rho\frac{\partial\phi_1}{\partial t} \qquad (4.2.1a)$$

$$H_2 = \frac{1}{2}\rho\, {u_2}^2 + p_2 + \rho\frac{\partial\phi_2}{\partial t} \qquad (4.2.1b)$$

Here, H, u and p represent the total head, velocity and pressure respectively. The total head must be the same on each side since the whole flow is started from a uniform state. This requirement, together with pressure continuity, gives

$$\left|\frac{\partial(\phi_1 - \phi_2)}{\partial t}\right| = \frac{1}{2}\left|({u_1}^2 - {u_2}^2)\right| \qquad (4.2.2)$$

Since the difference in velocity potential across the sheet represents the vortex intensity of the sheet, there results

$$\left|\frac{\partial\omega}{\partial t}\right| = \frac{1}{2}\left|({u_1}^2 - {u_2}^2)\right| \qquad (4.2.3)$$

The separation angle of the vortex sheet, θ_s, as shown in Fig. 34a, is such that the boundary condition on the wing surface, given by Eq. (2.3.11a), is satisfied. In this study the separation angle is set to zero, as shown in Fig. 34b, implying that vorticity going into the vortex structure is shed parallel to the lower surface.[57,60]

This assumption makes the velocity on the upper side of the vortex sheet equal to zero, since the assumed streamline, as indicated in Fig. 34b, causes a stagnation point on the upper part of the vortex sheet. Combining Eq. (4.2.3) with the relationships $x = Ut$, the strength of a new vortex can be calculated as

$$\begin{aligned} \Gamma_{\text{new}} &= \frac{1}{2}\, {u_1}^2\, \Delta t \\ &= \frac{1}{2}\, {u_1}^2\, \frac{\Delta x}{U} \end{aligned} \tag{4.2.4}$$

Normalizing with $Ua(x)$, Eq. (4.2.4) reduces to

$$\Gamma'_{\text{new}} = \frac{\Gamma_{\text{new}}}{Ua(x)} = \frac{1}{2}\left(\frac{u_1}{U}\right)^2 \frac{\Delta x}{x}\, \frac{k}{\tan\epsilon} \tag{4.2.5}$$

The position of this new vortex can be obtained by considering the convection velocity at the separation point. By definition, a vortex sheet moves with the average of the velocities at its two sides. Then, the convection velocity of the newly shed vortex is

$$u_s = \frac{1}{2}\,(u_1 + u_2) = \frac{1}{2}\, u_1 \tag{4.2.6}$$

The position of the new vortex is then

$$\sigma_{\text{new}} = \sigma_s + \mathbf{e}_s\, \Delta t\, u_s = \sigma_s + \mathbf{e}_s\, \frac{\Delta x}{U}\, u_s \tag{4.2.7}$$

where σ_s is the position of the separation point, and $\mathbf{e}_s$ is the unit vector tangent to the lower surface at the separation point, as illustrated in Fig. 34c.

Normalizing with $a(x)$, Eq. (4.2.7) becomes

$$\sigma'_{\text{new}} = \sigma'_s + \mathbf{e}_s\, \frac{\Delta x}{x}\, \frac{k}{\tan\epsilon}\, \frac{u_s}{U} \tag{4.2.8}$$

4.3 Wing Cross-Section Representation

The problem consists in solving Eq. (2.3.7) with the vorticity distribution given by Eq. (4.1.1) on the rolled-up shear layer, subject to boundary conditions (2.3.11a,b) and the Kutta condition expressed by Eqs. (4.2.5) and (4.2.8).

As mentioned in Section **2.1**, the boundary value problem given by Eqs. (2.3.7) and (2.3.11) can be solved in terms of a distribution of sources and doublets on the boundaries. The doublet distribution is replaceable by a vorticity distribution.[91] In this study the wing cross-section is represented by vorticity panels of linearly varying strength.

If the body is divided into $m-1$ vorticity panels and there are n vortices in the shear layers, as shown in Fig. 35, the stream function at the point i in the flow field can be written as

$$\begin{aligned} \Psi_i \;=\; & \oint \omega(\sigma_j)\; K(\sigma_i, \sigma_j)\; d\sigma_j \\ & + \frac{1}{2\pi} \sum_{k=1}^{n} \Gamma_k \;\log r_{ik} \;+\; U \;\tan\alpha \; y_i \end{aligned} \tag{4.3.1}$$

where $\omega(\sigma_j)$ is the bound vorticity density at the j^{th} panel, and $K(\sigma_i, \sigma_j)$ are the geometric influence coefficients, which depends only on wing geometry. r_{ik} is the distance between the i point and the k^{th} vortex.

The first term on the right-hand side is the stream function due to the bound vorticity panels, and the second term represents the stream function due to the discrete vortices distributed on the shear layer. The last term is due to the vertical component of the free-stream.

Boundary condition (2.3.11a) gives

$$\Psi_1 = \Psi_2 = \cdots = \Psi_m = \text{const.} = c \tag{4.3.2}$$

Conservation of the total circulation in the flow field as given by Eq. (2.3.9) implies that the total vorticity in the whole flow field must be zero

$$\oint \omega_j \, d\sigma_j + \sum_{k=1}^{n} \Gamma_k = 0 \tag{4.3.3}$$

Here there are $m+1$ unknowns; m ω's for the vorticity panels and c, the value of the stream function on the wing trace in the cross-flow plane. Eqs. (4.3.1) and (4.3.3) are a set of $m+1$ equations. Combining Eqs. (4.3.1), (4.3.2) and (4.3.3), the following system of equations results

$$\begin{pmatrix} a_{11} & a_{12} & \cdots & a_{1m} & 1 \\ a_{21} & a_{22} & \cdots & a_{2m} & 1 \\ \vdots & \vdots & \ddots & \vdots & \vdots \\ a_{m1} & a_{m2} & \cdots & a_{mm} & 1 \\ d_1 & d_2 & \cdots & d_m & 0 \end{pmatrix} \begin{pmatrix} \omega_1 \\ \omega_2 \\ \vdots \\ \omega_m \\ c \end{pmatrix} = - \begin{pmatrix} b_1 \\ b_2 \\ \vdots \\ b_m \\ \sum_{k=1}^{n} \Gamma_k \end{pmatrix} \tag{4.3.4}$$

The matrix a_{ij} is called the geometric influence coefficient matrix and is constant during time iteration. The b_j's are the stream function values induced by the vortices in the shear layers and the free stream. The last row in the matrix represents the integration of the bound vorticity panels. Using the trapezoidal rule for the integration, d_j can be written as

$$d_j = \frac{1}{2}(l_j + l_{j+1}) \tag{4.3.5}$$

where l_j is the length of j^{th} vorticity panel.

4.4 Solution Procedure

The steady-unsteady analogy developed in Section **2.2.2** shows that the solution of Eq. (4.3.4) (bound vortex strength and stream function at wing trace) as well as the the position and strength of the shear layer core (represented by a single vortex) must reach a converged state when expressed in terms of a similarity variable. Converting the time variable to the x coordinate through the relationship $x = Ut$, all the length scales can be normalized with $a(x)$ and the vortex strength with $Ua(x)$. Since in this transformation the total wing span length $a(x)$ increases with time, the vortex strength, vortex position and core radius are re-normalized at the beginning of each time step. Only the right-hand side vector of Eq. (4.3.4) is varied at each time step. Such changes result from an increment in the number of vortices in the shear layer through the Kutta condition given by Eqs. (4.2.5) and (4.2.8), and from the movement of the vortices as a consequence of the induced velocities. The left-hand side matrix remains constant throughout the calculation procedure.

4.5 Aerodynamic Forces

The pressure coefficient was derived in the previous chapter as

$$C_p = \tan^2\alpha - 2\frac{v_x}{U} - \left(\frac{v_y}{U}\right)^2 - \left(\frac{v_z}{U}\right)^2 \tag{4.5.1}$$

The magnitude of the velocity in the cross-flow plane is numerically equal to the bound vortex strength per unit length, since the flow internal to the wing cross-section is assumed to be at rest.[57] As indicated in Fig. 36, the bound vortex strength can be written as

$$\omega\, ds = \int \mathbf{v} \cdot d\mathbf{l} = \sqrt{{v_y}^2 + {v_z}^2}\, ds \tag{4.5.2a}$$

hence

$$\omega = \sqrt{{v_y}^2 + {v_z}^2} \tag{4.5.2b}$$

In this study, the bound vortex strength itself represents the outer velocity of the boundary layer. As a result, the magnitude of the velocity in the cross-flow plane can be obtained from the solutions of Eq. (4.3.4). The perturbation velocity in the axial direction can be obtained from the following conical relationship

$$v_x = \frac{1}{x}\left(U \tan\alpha + \phi_u - y\, v_y - z\, v_z\right) \tag{4.5.3}$$

The velocity potential is given in terms of logarithmic functions and its evaluation requires consideration of branch cuts, as shown in Fig. 37. By integrating the load distribution given by Eq. (4.5.1) over wing and flap surfaces, the total resultant force on each surface can be obtained.

4.6 Trailing Edge Wake

The trailing edge wake of a delta wing, as shown in Fig. 1, has a shape different from that of a conventional large aspect-ratio wing. The pressure peak just below the leading edge vortex core reflects a vorticity distribution such that the bound vortex strength, as a function of spanwise location, has a maximum between the wing center and the wing leading edge, as illustrated in Fig. 38. Conical flow implies the assumption that the wing extends infinitely far downstream, namely, that no trailing edge exists. To study the trailing edge wake roll-up in a qualitative way, an artificial trailing edge is assumed to exist, from which the conical vorticity distribution calculated on the wing surface is released. A Kutta condition is applied such that there is no pressure jump at the trailing edge.

The bound vorticity on the wing surface has two components, as shown in Fig.

39. These two components must satisfy the divergence free condition

$$\nabla \cdot \vec{\Omega} = \frac{\partial \omega}{\partial x} + \frac{\partial \eta}{\partial z} = 0 \tag{4.6.1}$$

where $\vec{\Omega} = \omega\, \mathbf{e}_x + \eta\, \mathbf{e}_z$

The absence of a pressure jump at the wing trailing edge demands that the shed vorticity at the trailing edge should be aligned with the local velocity. An approximate form of the trailing edge Kutta condition[92] can be written as follows

$$\frac{\partial\, \eta}{\partial\, z} = 0 \tag{4.6.2}$$

then Eq. (4.6.1) reduces to

$$\frac{\partial \omega}{\partial x} = 0 \tag{4.6.3a}$$

or

$$\omega = \omega(z) \tag{4.6.3b}$$

This indicates that ω, which is identified with the ω's from Eq. (4.3.4), is constant as it moves downstream. After the trailing edge, the evolution of the wake is solved in a straightforward way using a 2-D time evolution technique.

4.7 Numerical Implementation

4.7.1 Influence Coefficients

The stream function at a control point i due to the j^{th} panel, having linearly varying vorticity intensity, and its corresponding panel at the other side of the

plane of symmetry, as shown in Fig. 40, can be written as

$$2\pi\Psi_{ij} = \int_0^{l_j} \left(\omega_j + \frac{\omega_{j+1}-\omega_j}{l_j}\right) (\log r_{is} - \log r_{i\bar{s}})\ ds \tag{4.7.1}$$

$$= P_{ij}\omega_j + Q_{ij+1}\ (\omega_{j+1}-\omega_j)$$

where l_j is the length of j^{th} panel and

$$P_{ij} = \int_0^{l_j} (\log r_{is} - \log r_{i\bar{s}})\ ds \tag{4.7.2a}$$

$$Q_{ij} = \frac{1}{l_j}\int_0^{l_j} s\,(\log r_{is} - \log r_{i\bar{s}})\ ds \tag{4.7.2b}$$

$$r_{is} = \sqrt{(y_i-y_s)^2 + (z_i-z_s)^2} \tag{4.7.2c}$$

$$r_{i\bar{s}} = \sqrt{(y_i-y_s)^2 + (z_i+z_s)^2} \tag{4.7.2d}$$

Evaluating these integrals, P_{ij} and Q_{ij} can be written as

$$P_{ij} = l_j\,(\log l_j - 1) - \int_0^{l_j} \log r_{i\bar{s}}\ ds \quad \text{if } i=j \text{ or } i=j+1 \tag{4.7.3a}$$

$$Q_{ij} = \begin{cases} \frac{1}{2}l_j\,(\log l_j - 1/2) - \frac{1}{l_j}\int_0^{l_j} s\ \log r_{i\bar{s}}\ ds & \text{if i=j} \\ \frac{1}{2}l_j\,(\log l_j - 3/2) - \frac{1}{l_j}\int_0^{l_j} s\ \log r_{i\bar{s}}\ ds & \text{if i=j+1} \end{cases} \tag{4.7.3b}$$

The stream function value at point i due to the bound panels is

$$2\pi\ \Psi_i = \sum_1^{m-1} \left(P_{ij}\omega_j + Q_{ij}\,(\omega_{j+1}-\omega_j)\right)$$

$$= \sum_1^{m-1} \left(P_{ij} - Q_{ij} + Q_{ij-1}\right)\ \omega_j \tag{4.7.4}$$

Then the elements of the matrix of influence coefficients are

$$a_{ij} = \frac{1}{2\pi}\left(P_{ij} - Q_{ij} + Q_{ij-1}\right) \tag{4.7.5}$$

4.7.2 Induced Velocity

Once strength of the bound vortex panels is obtained by solving Eq. (4.3.4), the flow field velocity is used to update the positions of the vortices in the shear layers. From Eq. (4.1.4), each component of the induced velocity outside the core is

$$v_y = \frac{\Gamma_j}{2\pi}\frac{z - z_j}{(y-y_j)^2 + (z-z_j)^2} \tag{4.7.6a}$$

$$v_z = -\frac{\Gamma_j}{2\pi}\frac{y - y_j}{(y-y_j)^2 + (z-z_j)^2} \tag{4.7.6b}$$

where Γ_j is the strength of the j^{th} vortex.

With

$$y - y_s = y - \left(y_j + s\hat{y}_j\right) \tag{4.7.7a}$$

$$z - z_s = z - \left(z_j + s\hat{z}_j\right) \tag{4.7.7b}$$

where $(\hat{y}_j, \hat{z}_j)$ is the slope of the j^{th} vortex panel, the velocity induced by the j^{th} bound vortex panel can be obtained from Eqs. (4.7.6a,b) with the following definition of Γ_j

$$\Gamma_j = \int_0^{l_j}\left(\omega_j + \frac{\omega_{j+1} - \omega_j}{l_j}\, s\right) ds \tag{4.7.8}$$

When the point where the induced velocity to be calculated is located within the core, the induced velocity is obtained from the velocity distribution in Eq. (4.1.7)

$$v_y = \frac{\Gamma_j}{2\pi}\,(z - z_j)\,\frac{3 - 3\varrho^2 + \varrho^4}{\varsigma_j^2} \tag{4.7.9a}$$

$$v_z = -\frac{\Gamma_j}{2\pi}\,(y - y_j)\,\frac{3 - 3\varrho^2 + \varrho^4}{\varsigma_j^2} \tag{4.7.9b}$$

where

$$\varrho^2 = \frac{(y-y_j)^2 + (z-z_j)^2}{\varsigma_j^2} \tag{4.7.10}$$

4.7.3 Numerical Implementation of the Kutta Condition

Flow separation in a 2-D or a 3-D flow arises from viscous effects. An equivalent effect is imposed on the inviscid problem through a Kutta condition. A converged quasi-steady analysis requires that the shed vorticity at the wing side edges be convected with finite velocity. This velocity, not known a priori, is the average of the velocity on both sides of the wing at the side edge.[59] In a 2-D case the velocity at the separation point can be determined from the experimentally established fact that the Strouhal number, when expressed in terms of the base pressure at the separation point, is constant.[93] Experimental observations on the flow past an inclined flat plate have shown that this velocity is about 1.5 U.[94] Under the conical flow assumption, the value of this velocity must be constant along the leading edges. Other workers have attempted to find this value experimentally and have applied it to the solution of delta wing problems with the vortex cloud method,[31] failing to attain converged solutions. In this work this velocity is theoretically determined by recognizing the fact that, after a sufficiently large time and for given values of α, ϵ and δ, it must achieve a constant value. It was found that if an initial value for the bound vortex strength of about $3U$ is assumed, convergence to the final value of the side edge convective velocity is achieved within 300 steps. Too large initial values lead to oscillatory end behavior, while too small initial values require significantly more time steps.

4.7.4 Core Model

The core region for a conical flow has large axial velocity, and the flux of vorticity generated along the leading edges and supplied to the core through the rolled-up shear layer is balanced by that convected by the axial velocity. Thus, the core region, usually identified with the "vortex jungle" in a 2-D vortex cloud computation, cannot be included in this model of the conical flow since it would violate the condition of aerodynamic slenderness. Hence, the core region is represented by a single vortex through a simple merging scheme. By imposing a restriction on the rotation angle of the vortices, the efficiency of the numerical effort is increased and good definition of shear layers is achieved. Other studies[30,37] have shown that the rotation angle of the shear layer, as long as it is set greater than 2π, has a small effect on overall quantities. The same conclusion is arrived at in this study.

The vortices which rotate more than a given angle are allowed to merge into the core, which is then simulated by a single vortex. The position, strength and core size are determined such that the angular momentum before and after the merging is conserved. If k vortices are merged together, conservation of angular momentum outside the core region is expressed by the following relationships for the core position and strength

$$\sigma_c = \frac{\sum_{i=1}^{k} \sigma_i \Gamma_i}{\sum_{i=1}^{k} \Gamma_i} \tag{4.7.11}$$

$$\Gamma_c = \sum_{i=1}^{k} \Gamma_i \tag{4.7.12}$$

The angular momentum within the core is

$$M = \int_0^{2\pi} \int_0^{\varsigma} (\sigma_c + r)\, u\, r\, d\theta\, dr \tag{4.7.13}$$

where σ_c is the position of the core center, and r is a distance from the core center to a point inside the core. u is the velocity distribution inside the core as given by Eq. (4.1.7). Performing the integration, the angular momentum reduces to

$$M = \frac{17}{24}\, \Gamma\, \varsigma^3 \tag{4.7.14}$$

Then the core size after merging is

$$\varsigma_c = \left(\frac{\sum_{i=1}^{k} \Gamma_i\, \varsigma_i^3}{\sum_{i=1}^{k} \Gamma_i} \right)^{1/3} \tag{4.7.15}$$

Strength and position are independent of the vorticity distribution inside the core, but core size is dependent on vorticity distribution.

4.7.5 Merging between Neighboring Vortices

A similar merging technique as the one used for the core model is also applied to the neighboring vortices such that if the distance between them is less than a given value two vortices are allowed to merge into one. This value is set equal to the mean value of the radii of the two vortices. Position, strength and the core radius after merging are determined from Eqs. (4.7.11), (4.7.12) and (4.7.15). The merging scheme allows for a reduction of the total number of vortices by almost a half, making the scheme much more efficient.

4.7.6 Absorption of Vortices on Wing Surfaces

In this discretization of a separated wake, vortices coming very close to the surface

have the tendency to penetrate the wing surface. This is observed to happen even with very small time step and large number of panels. A means of resolving this difficulty has been suggested by Lighthill,[95] and consists in allowing the vortices that come within a thin layer on the wing surface to disappear. Another way consists in relocating the vortices which penetrated the surface in a preceding time step, to its image point outside the surface.[68] Here the vortices which come closer than a given distance to the wing surface are made to disappear. This distance is set equal to 1% of the local wing span. This surface merging tends to occur when the angle of attack is small or when the flap deflection angle is large.

4.7.7 Integration Method for Advancing Vortex Position

Any 2-D discrete vortex method contains a vorticity diffusion effect due to the numerical error involved in time integration. The numerical diffusion effect is shown in Fig. 41. Some authors[66,69] maintain that this numerical error could be responsible for instability of the vortex motion. Others[60,70] suggest that this numerical error simulates a turbulent diffusion rather than a viscous diffusion. In a conical flow the diffusion effect arising from the numerical error is less marked than in a 2-D flow. This may be attributed to the fact that the shear layers in the conical flow develop in a field of intense circumferential velocity, which allows for a shorter time during which numerical dissipation acts. Here both a 1st order Euler method and a 4th order Runge-Kutta method were used for time integration. These schemes are:

1st order Euler method

$$\sigma_v(t+\Delta t) \;=\; \sigma_v(t) \;+\; \mathbf{v}_v\,(t,\sigma_v(t))\,\Delta t \qquad (4.7.16)$$

4th order Runge-Kutta method

$$\sigma_v^*\left(t+\frac{\Delta t}{2}\right) = \sigma_v(t) + \frac{\Delta t}{2}\,\mathbf{v}_v\left(t,\sigma_v(t)\right)$$

$$\sigma_v^{**}\left(t+\frac{\Delta t}{2}\right) = \sigma_v(t) + \frac{\Delta t}{2}\,\mathbf{v}_v\left(t+\frac{\Delta t}{2},\sigma_v^*\left(t+\frac{\Delta t}{2}\right)\right)$$

$$\sigma_v^{***}(t+\Delta t) = \sigma_v(t) + \Delta t\,\mathbf{v}_v\left(t+\frac{\Delta t}{2},\sigma_v^{**}(t+\Delta t/2)\right)$$

$$\sigma_v(t+\Delta t) = \sigma_v(t) + \frac{\Delta t}{6}\left[\mathbf{v}_v\left(t,\sigma_v(t)\right) + 2\,\mathbf{v}_v\left(t+\frac{\Delta t}{2},\sigma_v^*\left(t+\frac{\Delta t}{2}\right)\right)\right.$$

$$\left. + 2\,\mathbf{v}_v\left(t+\frac{\Delta t}{2},\sigma_v^{**}\left(t+\frac{\Delta t}{2}\right)\right) + \mathbf{v}_v\left(t+\Delta t,\sigma_v^{***}(t+\Delta t)\right)\right] \tag{4.7.17}$$

4.8 Results

4.8.1 Shear Layer Geometry and Surface Pressure Distribution

Fig. 42 shows the convergence of the vorticity intensity at the separation point for an initial guess of $3U$. Significant oscillation can be seen during the first 50 steps. If too large an initial guess is used, the vortex strength oscillates such that it changes sign during some time steps, leading to nonphysical results. Given α and δ, a proper initial guess for each case is needed to obtain the final vorticity intensity at the separation point. This value decreases as the flap deflection angle increases and as the angle of attack decreases.

The convergence of the present calculation can be assessed through core position, core vortex strength and core radius, as shown in Figs. 43a,b. The core vortex

strength shows some oscillation even after convergence is attained, since the vortices in the shear layer merge into the core at finite intervals.

Fig. 44a shows the vortex jungle that arises when no core model is used. In addition, the shear layer is not clearly defined. Fig. 44b shows a case where a core rotation angle of 2.5π was imposed for the same configuration and exhibits good shear layer definition.

The effect of the merging scheme between neighboring vortices is shown in Figs. 45a,b. By replacing high density clouds with fewer vortices, the total number of vortices is reduced by almost a half.

Fig. 46 shows the effect of two schemes of time integration. As anticipated in Section **4.7.7**, the 1^{st} order Euler scheme gives a much more diffused shear layer than the 4^{th} order Runge-Kutta method. Overall flow field features do not depend significantly on the integration scheme.

The data for comparison with experiments were taken from Ref. 3, where the model had a trailing edge thickness of 7.7% of the half span and a 22 deg. half apex angle with undeflected flap. The ratio of the main wing span to the total span was 0.6. The data used for comparison were measured at a spanwise station located 37% of the chord from the apex, to minimize the trailing edge effect.

Figs. 47a,b show the rolled-up shear layer and surface pressure distribution for α =25 deg. and δ = 0 deg. Agreement can be considered very good, except for a small region near the leading edge, where a secondary vortex may have been present in the experiments and would be responsible for the disagreement.

Figs. 48 and 49 are the cases for flap deflection angle of 15 deg. and 30 deg. and same angle of attack as the case of Fig. 47. The pressure at the centerline decreases with flap angle, which indicates that the effect of flap deflection is similar

to a reduction of angle of attack. Although the vortex position does not move much with flap angle, some movement toward the surface is observed, which has also been reported elsewhere.[17] The hinge vortex is hardly observable in the cases analyzed here, being quite weak and tending to be absorbed into the wing surface. Fig. 49 shows a weak hinge vortex. The greater discrepancy between computation and experiment near the leading edge is attributed to the stronger secondary vortices at higher flap deflection.

Fig. 50 shows the case of $\alpha = 15$ deg., without flap deflection. The pressure distribution shows good agreement. The effect of a secondary vortex is also stronger than at $\alpha = 25$ deg. The width of the pressure peak region is less than shown by the measurements.

Fig. 51 shows the case with 15 deg. flap deflection angle with $\alpha = 15$ deg. This figure shows the same trends as the straight-feeding-model, shown in Fig. 32.

Fig. 52 shows the rolled-up shear layer and surface pressure distribution for $\alpha = 35$ deg., without flap deflection. The shear layer shows a tendency to produce the type of coherent structures which have been experimentally observed, as described in Fig. 6, taken from Ref. 77.

The cases of $\delta = 15$ deg. and 35 deg. with same angle of attack are shown in Figs. 53 and 54. In both cases, the hinge vortices have almost entirely disappeared. For a flap deflection of 15 deg. the pressure peak is underpredicted. The effect of the secondary vortex is clearly seen in the case of 35 deg. flap angle. Calculated results show a strong adverse pressure gradient near the leading edge on the upper surface, as indicated in Fig. 54, which would cause flow separation. This separated flow, not resolved for in this calculation, would give rise to a strong vortical flow, which results in the appearance of a secondary pressure peak. This secondary peak

is clearly seen in the experimental data in Fig. 54.

In Fig. 55, the calculated trailing edge wake is compared with computations from a higher-order panel method.[61] Reasonably good agreement is obtained.

4.8.2 Lift, Drag, Lift-to-Drag Ratio

The following table shows computed and measured changes in each of the force components and the lift-to-drag ratio as a result of flap deflection, for $\alpha = 25$ deg. The experimental data are sectional force coefficients taken at 37% of the chord from the apex.

	$\delta = 0$		$\delta = 15$		$\delta = 30$	
	Exp.	VCM	Exp.	VCM	Exp.	VCM
C_L	3.01	3.14	2.52	2.55	2.32	1.88
C_D	1.4	1.46	1.04	1.06	0.85	0.68
C_L/C_D	2.14	2.14	2.42	2.41	2.73	2.76

While lift and drag decrease with flap deflection, the lift-to-drag ratio increases. For a flap deflection of 30 deg., that increment is about 30%.

4.9 Summary

The vortex cloud model gives satisfactory agreement with experiments in pressure distribution and global forces. Good shear layer definition is also obtained.

The wing model analyzed in this work exhibited negligibly small hinge vortices, both in theory and experiment. The usually observed instabilities of delta wing shear layers are hardly found, except in the high angle of attack range, and become more visible if no merging scheme between neighboring vortices is implemented.

Use of a 1^{st} order Euler scheme for time integration shows more clearly this kind of instability than a 4^{th} order Runge-Kutta method.

Comparison of pressure distributions with experimental measurements shows that the effect of the secondary vortex becomes significant in the range of small angle of attack and large flap deflection angle. Limitations of this model can be observed through comparison with experimental results for large flap deflection angles. The disagreement is caused partly by the effects of secondary vortices, and partly by the inability of the cross-flow plane analysis to resolve true velocity components on the flap surface.

Leading edge flap deflection reduces the lift and drag of the wing and increases its lift-to-drag ratio. As was the case with the simpler model in the previous chapter, it is found that flap deflection is equivalent to a reduction in angle of attack.

Chapter 5

Comparison of Results

In this chapter the results obtained from the two approaches analyzed in Chapter **3** and **4** are compared with results from other analyses and experiments. Experimental data are obtained from Ref. 3, and other analyses are given by Smith's theory[30] and a 3-D panel approach.[19]

Fig. 56 shows the comparison of core position and rolled-up shear layer geometry between Smith's calculation and the vortex cloud model, for $\alpha/\epsilon = 1$. Smith determined the shear layer core position by applying the force free condition to the core, which was modeled as a concentrated vortex. In this respect his core model differs from the vortex cloud's, which uses a simple merging scheme by imposing a restriction on the shear layer rotation angle. Although the core models are quite different, shear layer shape and core position show good agreement between both methods.

A comparison between results from a 3-D panel analysis and the vortex cloud model is illustrated in Fig. 57 for the case of a leading edge fence, corresponding to an upward deflection of the leading edge flap of more than 90 deg. The results from the 3-D panel analysis were taken from Ref. 19 for $\epsilon = 16$ deg. and $k = 0.83$,

and chosen at the 30% of the chord from the apex to minimize the upstream effect of the trailing edge. Fig. 57a shows the pressure distribution without the fence for $\alpha = 20$ deg. The pressure peak region calculated with the vortex cloud model lies closer to the leading edge than that from the panel calculation. The case of 130 deg. fence angle is shown in Figs. 57b,c for the same angle of attack as Fig. 57a. The results show better agreement than without fence deflection.

A detailed discussion of the computation between theoretical results from this work and experiments is carried out, and possible reasons for the disagreements with experiment are discussed.

Pressure distributions for $\alpha = 25$ deg. and $\delta = 0$ deg. are shown in Fig. 58. Also shown are the results from the straight-feeding-sheet model. As mentioned in Chapter **3**, the straight-feeding-sheet model overpredicts the pressure peak, which appears shifted toward the leading edge, while the pressures on the lower surface and in the midspan region on upper surface are well predicted. This implies that the straight-feeding-sheet model seems to primarily overpredict the vortex component of lift. The results from the vortex cloud model agree well with experiments.

The pressure distribution for the case of $\alpha = 25$ deg. and $\delta = 15$ deg. is shown in Fig. 59. The results from the vortex cloud model show that the pressure on the upper surface is almost constant near the center region and rises more sharply to a pressure peak than the experimental results. A similar situation occurs in the region where the vortices are absorbed by the wing surface. This phenomenon can be more clearly seen in case of $\delta = 30$ deg., as illustrated in Fig. 49. The overall pressure distribution agrees well with experiments, while the pressure peak is slightly overpredicted. In this case, the hinge vortices are extremely weak. This fact was also suggested by results from the straight-feeding-sheet model. The

extreme closeness of the hinge vortex to the wing surface caused oscillations in the numerics of the straight-feeding-sheet model, such that it was found convenient to neglect the hinge vortex altogether. Results obtained neglecting the hinge vortex are shown in Fig. 59. The pressure peak is unrealistically overpredicted and the pressure peak region is much narrower than indicated by the vortex cloud model or experiments. This is explained by the position of the leading edge vortex being very close to the wing surface.[96] Thus, the straight-feeding-sheet model exaggerates the vortex displacement with flap deflection.

Chapter 6

Conclusions and Recommendations

The effects of leading edge flaps on the aerodynamics of delta wings was investigated theoretically using two different approaches. A mathematical analogy was invoked to treat a 3-D conical flow field in subsonic and supersonic cases. Through the analogy, a conical steady flow field can be represented by a 2-D unsteady self-similar ideal flow, whose treatment is far simpler than that of a 3-D flow. Two different vortex models were used as techniques to solve a 2-D unsteady flow, and the results were compared with experimental data and other methods of analysis.

6.1 Conclusions

6.1.1 Straight-Feeding-Sheet Model

While this simple model leads to poor agreement in pressure distribution with experiments, some of the the effects of leading edge flaps on the delta wing aerodynamics are suggested. The wing's geometric parameters, such as ϵ, δ and k, together with the angle of attack appear explicitly in the equations for the vortex positions and

the normal force components. From Eq. (3.4.23), which shows the normal force arising from the vortex system, it can be predicted that the normal force component reduces with flap deflection, since the leading edge vortex strength and the distance between the vortex and its image vortex in the transformed plane reduce with flap deflection. Also Eq. (3.4.24), which is the normal force component corresponding to an attached flow situation, shows the explicit effects of flap deflection, resulting in a decrement of the normal force component with flap deflection. This model indicates that the increment of lift-to-drag ratio during flap deflection is more significant in the low angle of attack range, as observed in experimental results.[3] The straight-feeding-sheet model exaggerates the vortex displacement and leading edge suction arising from flap deflection.

6.1.2 Vortex Cloud Model

This model provides a good definition of shear layers and good agreement in surface pressure distribution with experiments and 3-D panel calculations, as long as the validity criteria derived in Chapter **2** are respected. The effects of flap deflection are properly represented. The non-appearance of hinge vortices in the range of angle of attack analyzed in this approach is confirmed by experimental observation. Cases of low angle of attack and large flap deflection angle would violate the conicality and slenderness criteria and are consequently not expected to be predicted well by this model.

6.1.3 Effects of Flap Deflection on Delta Wing Aerodynamics

A decrement in vortex strength, caused by flap deflection, delays vortex breakdown by reducing the adverse pressure gradient around the trailing edge. Lift and drag decrease with flap deflection, while the lift-to-drag ratio increases. The reduction

of lift and drag arises from the partial suppression of the vortical flow, and the increment of the lift-to-drag ratio derives from the thrust component of force acting on the flap surfaces.

6.2 Recommendations

The vortex cloud model gives good definition of shear layers, which current Navier-Stokes solvers cannot provide since an impractically fine grid distribution would be required to capture such discontinuity surfaces. This work can provide some insight in supplying initial grid distributions to Navier-Stokes solvers, thereby reducing computational cost.

This study could also be extended to moderately supersonic flows where the Mach cone angle is closer to the wing apex angle. In such cases the approach as developed here would fail, since the far field boundary conditions would be altered by the Mach cone. A mapping function, the so-called Tschaplygin transformation,[82] has been developed to account for the Mach cone trace in the cross-flow plane. Combined with the Tchaplygin transformation, the steady-unsteady analogy developed in this study would provide a scheme to treat a moderately supersonic conical flow.

In this study the comparison between the results from experiments and calculation based on the steady-unsteady analogy is made only for the incompressible case. For compressible flows, application of a similarity rule for the pressure coefficient would be required, since the wing geometry and the free-stream condition are distorted as a result of applying the Prandtl-Glauert transformation. Such a similarity rule for the pressure coefficient for a slender wing is given in Appendix 3.

Bibliography

1. D. Küchmann, F.R.S., *The Aerodynamic Design of Aircraft.* Pergamon, 1978
2. J.E. Lamar and J.F. Campbell, Vortex Flaps - Advanced Control Devices for Supercruise Fighters. *Aerospace America*, January, 95-99, 1984
3. C.S. Lee, Experimental Studies of a Delta Wing with Leading Edge Flaps. JIAA TR-76, Joint Institute for Aeronautics and Acoustics, Stanford University, 1987
4. K.D. Hoffler, D.M. Rao and M.C. Frassinelli, Low-Speed Aerodynamics of Apex Fences on a Tailess Delta Configuration. AIAA Paper-86-1838, 1986
5. D.M. Rao and T.D. Johnson, Jr., Subsonic Pitch-Up Alleviation on a 74 Deg. Delta Wing. NASA Contractor Report 165749, 1981
6. D.M. Rao, Upper Vortex Flap - A Versatile Surface for Highly Swept Wings. ICAS 13^{th} Congress Paper 82-6.7.1 1982
7. D.M. Rao, Vortical Flow Management for Improved Configuration Aerodynamics - Recent Experience. AGARD-342, 1984
8. D.M.Rao, An Exploratory Study of Area-Efficient Vortex Flap Concepts. *Journal of Aircraft* Vol. 20, No. 12, pp. 1062-1067, 1983
9. D.M. Rao and T.D. Johnson, Investigation of Delta Wing Leading-Edge Devices. *Journal of Aircraft* Vol. 18, No. 3, pp. 161-167, 1981

10. N.T. Frink, Analytical Study of Vortex Flaps on Highly Swept Delta Wings. ICAS 13th Congress, Paper 82-6.7.2, 1982

11. J.F. Marchman, III, The Aerodynamics of Inverted Leading Edge Flaps on Delta Wings. AIAA Paper-81-0356, 1981

12. J.F. Marchman, III, Effectiveness of Leading-Edge Vortex Flaps on 60 and 75 Degree Delta Wings. *Journal of Aircraft* Vol. 18 No. 4, pp. 280-286, 1981

13. W.E. Schoonover, Jr. and W. E. Ohlson, Wind-Tunnel Investigation of Vortex Flaps on a Highly Swept Interceptor Configuration. ICAS 13th Congress, Paper 82-6.7.3., 1982

14. K.D. Hoffler and D.M. Rao, An Investigation of the Tabbed-Vortex Flap. *Journal of Aircraft* Vol. 22, No. 6, pp. 490-497, 1985

15. L.P. Yip and D.G. Murri, Effects of Vortex Flaps on the Low-Speed Aerodynamic Characteristics of an Arrow Wing. NASA Technical Paper 1914, 1981

16. P.L. Coe, Jr. and R.P. Weston, Effects of Wing Leading-Edge Deflection on Low-Speed Aerodynamic Characteristics of a Low-Aspect-Ratio Highly Swept Arrow-Wing Configuration. NASA Technical Paper 1434, 1979

17. S. Oh and D. Tavella, Analysis of a Delta Wing with Leading Edge Flaps. *Journal of Aircraft* Vol. 24, No. 6, pp. 353-354, 1987

18. S. Oh and D. Tavella, Application of Vortex Cloud Method to Slender, Flapped Delta Wings. JIAA TR-83, Joint Institute for Aeronautics and Acoustics, Stanford University, 1987

19. C.S. Reddy, Spanwise Pressure Distribution on Delta Wing with Leading-Edge Vortex Flap. *Journal of Aircraft* Vol. 24, No. 3, pp. 222-224, 1987

20. C.E. Brown and W.H. Michael, Jr., Effects of Leading-Edge Separation on the

Lift of a Delta Wing. *Journal of Aeronautical Science* Vol. 21, pp. 690-694, 1954

21. C.E. Brown and W.H. Michael, Jr., On Slender Delta Wings with Leading-Edge Separation. NACA Technical Note 3430, 1955

22. D. Küchmann and J. Weber, Vortex Motion. *Zeitschrift Für Angewandte Mathematik und Mechanik* Vol. 45, pp. 457-474, 1965

23. R.H. Edwards, Leading-Edge Separation from Delta Wings. *Journal of the Aeronautical Sciences* February, 1954

24. K.W. Mangler and J.H.B. Smith, A Theory of the Flow past a Slender Delta Wing with Leading Edge Separation. Proceedings of Royal Society London A, Vol. 251, pp. 200-217, 1956

25. K.W. Mangler and J. Weber, The Flow Field near the Center of a Rolled-Up Vortex Sheet. *Journal of Fluid Mechanics* Vol. 30, part 1, pp. 177-196, 1967

26. K.W. Mangler and C.C.L. Sells, The Flow Field near the Center of a Slender Rolled-Up Conical Vortex Sheet. Royal Aircraft Establishment Technical Report 67029, 1967

27. R.K. Nangia and G.J. Hancock, A Theoretical Investigation for Delta Wings with Leading-Edge Separation at Low Speeds. Aeronautical Research Council Current Paper No. 1086, 1970

28. J.H.B. Smith, The Isolated-Vortex Model of Leading-Edge Separation Revised for Small Incidence. Royal Aircraft Establishment Technical Report 73160, 1973

29. B. Niekerk, A Rational Approach to Lifting Surface Theory with Application to High Angles of Attack. SUDAAR-555, Stanford University, 1986

30. J.H.B. Smith, Improved Calculation of Leading-Edge Separation from Slender,

Thin, Delta Wings. Proceedings of Royal Society A, Vol. 306, pp. 67-90, 1968

31. A.H. Sacks, R.E. Lundberg and C.W. Hanson, A Theoretical Investigation of the Aerodynamics of Slender Wing-Body Combinations Exhibiting Leading-Edge Separation. NASA CR-719, 1967

32. M.I.G. Bloor and R.A. Evans, Strake/Delta Wing Interaction at High Angle of Attack. JIAA TR-30, Joint Institute for Aeronautics and Acoustics, Stanford University, 1980

33. A.J. Peace, A Multi-Vortex Model of Leading-Edge Vortex Flows. *International Journal for Numerical Methods in Fluids* Vol. 3, pp. 543-565, 1983

34. M.G. Hall, A Theory for the Core of a Leading-Edge Vortex. *Journal of Fluid Mechanics* pp. 209-228, 1961

35. K. Stewartson and M.G. Hall, The Inner Solution for the Core of a Leading-Edge Vortex. *Journal of Fluid Mechanics* pp. 306-318, 1962

36. O.A. Kandil, Recent Improvements in the Prediction of the Leading and Trailing Edge Vortex Cores of Delta Wings. AIAA Paper-81-1263, 1981

37. J.M. Luckering, A Theory for the Core of a Three-Dimensional Leading-Edge Vortex. AIAA Paper-85-0108, 1985

38. J.C. Cooke, Laminar Boundary Layer Calculations Compared with Measurements by Hummel. Aeronautical Research Council C.P. No. 1096 1967

39. J.C. Cooke, Boundary Layer in Three Dimensions. Progress in Aeronautical Society Vol. 2, pp. 222-282, 1962

40. J.A. Webber, G.W. Brune, F.T. Johnson, P. Lu and P.E. Rubbert, Three-Dimensional Solution of Flows over Wings with Leading-Edge Vortex Separation. *AIAA Journal* Vol. 14, No. 4, pp. 519-525, 1976

41. F.T. Johnson, E.N. Tinoco, P. Lu and M.A. Epton, Three-Dimensional Flow over Wings with Leading-Edge Vortex Separation. *AIAA Journal* Vol. 18, No. 4, pp. 367-380, 1980

42. H.W.M. Hoeijimakers and B. Bennekers, A Computational Model for the Calculation of the Flow about Wings with Leading-Edge Vortices. AGARD CP-247, 1972

43. O.A. Kandil and E.C. Yates Jr., Transonic Vortex Flows Past Delta Wings: Integral Equation Approach. *AIAA Journal* Vol. 24, No. 11, pp. 1729-1736, 1986

44. O.A. Kandil, Computational Technique for Compressible Vortex Flows Past Wings at Large Incidence. *Journal of Aircraft* Vol. 22, No. 9, pp. 750-755, 1985

45. J.H.B. Smith, Theoretical Modeling of Three-Dimensional Vortex Flows in Aerodynamics. AGARD CP-342, 1984

46. J.E. Barsby, Flow Past Conically-Cambered Slender Delta Wings with Leading-Edge Separation. Aeronautical Research Council Reports and Memoranda No. 3748, 1972

47. S.M. Hitzel and W. Schmit, Slender Wings with Leading-Edge Vortex Separation: A Challenge for Panel Methods and Euler Solvers. *Journal of Aircraft* Vol. 21, No. 10, pp. 751-759, 1984

48. D.P. Rizzetta and J.S. Shang, Numerical Simulation of Leading-Edge Vortex Flows. *AIAA Journal* Vol. 24, No. 2, pp.237-245, 1986

49. K. Fujii and L.B. Schiff, Numerical Simulation of Vortical Flows over a Strake-Delta Wing. AIAA Paper 87-1229, 1987

50. D.T. Yeh, D.A. Tavella, L. Roberts and K. Fujii, Navier-Stokes Computation of a Delta Wing with Leading Edge Normal Blowing. AIAA Paper 88-2558, 1988

51. S.P. Fiddes, A Theory of the Separated Flow Past a Slender Elliptic Cone at Incidence. AGARD CP-291, 1980

52. S.N. Brown, Singularities Associated with Separating Boundary Layers. Phil. Trans. Royal Soc. London A, No. 1084, Vol. 257, pp. 409-444, 1964

53. R.T. Jones, Properties of Low-Aspect-Ratio Pointed Wings at Speeds Below and Above the Speed of Sound. NACA Report No. 835, 1947

54. R.T. Jones, Properties of Low-Aspect-Ratio Pointed Wings at Speeds Below and Above the Speed of Sound. NACA Report No. 1032, 1949

55. L. Rosenhead, The Formation of Vortices from a Surface of Discontinuity. Proceedings of Royal Society, A London, Vol. 134, pp. 170-192, 1931

56. B.C. Basu and G.J. Hancock, The Unsteady Motion of a Two-Dimensional Airfoil in Incompressible Inviscid Flow. *Journal of Fluid Mechanics* Vol. 87, part1, pp. 159-178, 1978

57. R.I. Lewis, Surface Vorticity Modeling of Separated Flows from Two-Dimensional Bluff Bodies of Arbitrary Shape. *Journal of Mechanical Engineering Science* Vol. 23, No.1, pp. 1-12, 1981

58. C.S. Lee and S. Bodapati, Calculation of the Usteady Flow Field of an Airfoil with a Deflected Spoiler by Vortex Methods. JIAA TR-62, 1985

59. P.K. Stansby, A Generalized Discrete-Vortex Method for Sharp-Edged Cylinders, *AIAA Journal* Vol. 23, No.6, pp. 856-860, 1985

60. D.R. Polling and D.P. Telionis, The Response of Airfoils to Periodic Disturbances - The Unsteady Kutta Condition. *AIAA Journal* Vol. 24, No. 2, pp. 193-199,

1986

61, H.W.M. Hoeijimakers and W. Vaatstra, A Higher Order Panel Method Applied to Vortex Sheet Roll-Up. *AIAA Journal* Vol. 21, No. 4, pp. 516-523, 1983

62. A.J. Chorin, Numerical Study of Slightly Viscous Flow. *Journal of Fluid Mechanics* Vol. 57, Part 4, pp. 785-796, 1973

63. P.R. Spalart and T. Leonard, Computation of Separated Flows by a Vortex-Tracing Algorithm. AIAA Paper-81-1246, 1981

64. P.M. Stremel, A Method for Modeling Finite Core Vortices in Wake Flow Calculations. AIAA Paper-84-0417, 1984

65. D.J. Lee and C.A. Smith, Distortion of the Vortex Core During Blade/Vortex Interaction. AIAA Paper-87-1243, 1987

66. P.T. Fink and W.K. Soh, A New Approach to Roll-Up Calculation of Vortex Sheets. Proceedings of Royal Society of London, A. Vol. 362, 195-209, 1978

67. A. Leonard, Vortex Methods for Flow Simulation. *Journal of Computational Physics* Vol. 37, pp. 289-335, 1980

68. T. Fujinami, G.S. Dulikravich and A.A. Hansen, Free-Vortex Method Simulation of Unsteady Airfoil/Vortex Interaction. AIAA Paper 86-1792, 1986

69. R.R. Clements and D.J. Maull, The Representation of Sheets of Vorticity by Discrete Vortices. Progress of Aerospace Vol. 16, No. 2, pp. 129-146, 1975

70. K. Kuwahara, Study of Flow Past a Cylinder by a Inviscid Model. *Journal of the Physical Society of Japan* Vol. 45, No. 1, 1978

71. D.W. Moore, A Numerical Study of the Rolled-Up of a Finite Vortex Sheet. *Journal of Fluid Mechanics* Vol. 63, Part 2, pp. 225-235, 1974

72. T. Sarpkaya, An Inviscid Model of Two-Dimensional Vortex Shedding for Transient and Asymptotically Steady Separated Flow over an Inclined Plate. *Journal of Fluid Mechanics* Vol. 68, Part1, pp. 109-128, 1975

73. J. Katz, A Discrete Vortex Method for the Non-Steady Separated Flow over an Airfoil. *Journal of Fluid Mechanics* Vol. 102, pp. 315-328, 1981

74. J.P. Chistiansen, Numerical Simulation of Hydrodynamics by the Method of Point Vortices. *Journal of Computational Physics* Vol. 13, pp. 363-379, 1973

75. G.R. Baker, The "Cloud in Cell" Technique Applied to the Roll Up of Vortex Sheets. *Journal of Computational Physics* Vol. 31, pp. 76-95, 1979

76. Introduction to Vortex Dynamics, von Karman Institute for Fluid Dynamics Lecture Series 1986-08, Vol. 2, 1986

77. F.M. Payne, T.T. Ng and N.C. Nelson, Visualization and Flow Surveys of the Leading Edge Vortices Structure on Delta Wing Planforms. AIAA Paper 86-0330, 1986

78. L. Prandtl, The Mechanism of Viscous Flow in *Aerodynamic Theory* Vol. III, Section G, Edited by W.F. Durand California Institute of Technology, 1943

79. N.C. Lambourne and D.W. Bryer, Some Measurement in the Vortex Flow Generation by a Sharp Leading Edge having 65^o Sweep. ARC CP No. 477, 1959

80. K. Karamcheti, *Principles of Ideal-Fluid Aerodynamics* Robert E. Krieger Publishing Company, 1980

81. H.W. Liepmann and A. Roshko, *Elements of Gasdynamics* John Wiely & Sons, Inc. 1957

82. H. Ashley and M. Landahl, *Aerodynamics of Wings and Bodies* Dover 1965

83. M. Van Dyke, Lecture Note ME206 Similarity in Engineering Mechanics 1978

84. J. Rom, Lecture Note on High Angle of Attack Aerodynamics, 1986

85. N. Rott, Diffraction of a Weak Shock with Vortex Generation. *Journal of Fluid Mechanics* Vol. 1, pp. 111-128, 1956

86. A.E. Bryson, Symmetric Vortex Separation on Circular Cylinders and Cones. *Journal of Applied Mechanics* pp. 643-648, December, 1959

87. A. Betz, Behavior of Vortex System in Classical Aerodynamic Theory. NASA RP 1050 compiled by R.T. Jones, 1979

88. G.F. Carrier, M. Krook and C.E. Pearson, *Functions of Complex Variable* Hod Books, 1983

89. J.H. Ferziger, Lecture Note on Linear Mathematics for Engineering Application, 1978

90. J.H. Ferziger, *Numerical Methods for Engineering Application* John Wiley & Sons, 1981

91. B. Hunt, Numerical Methods in Applied Fluid Dynamics Editor B. Hunt Academic Press, 1980

92. R.L. Bisplinghoff, H. Ashley and R.L. Halfman, *Aeroelasticity* Addison-Wesley Publishing Company, 1955

93. A. Roshko, Experiments on the Flow Past a Circular Cylinder at Very High Reynolds Number. *Journal of Fluid Mechanics* pp. 345-356, 1961

94. A. Fage and F.C. Johansen, On the Flow of Air behind an Inclined Flat Plate of Infinite Span. Proc. Roy. Soc. A. London, Vol. 363, 1978

95. M.J. Lighthill, Chapter II in *Laminar Boundary Layer*, edited by L. Rosenhead, Clarendon Press, 1963

96. N.J. Wood and L. Roberts, The Control of Vortical Lift on Delta wings by

Tangentail Leading Edge Blowing. AIAA Paper 87-0158, 1987

97. B. Göthert, Plane and Three-Dimensional Flow at High Subsonic Speeds. NACA TM No. 1105, 1946

98. Van Dyke, *An Album of Fluid Motion* Parabolic Press, 1982

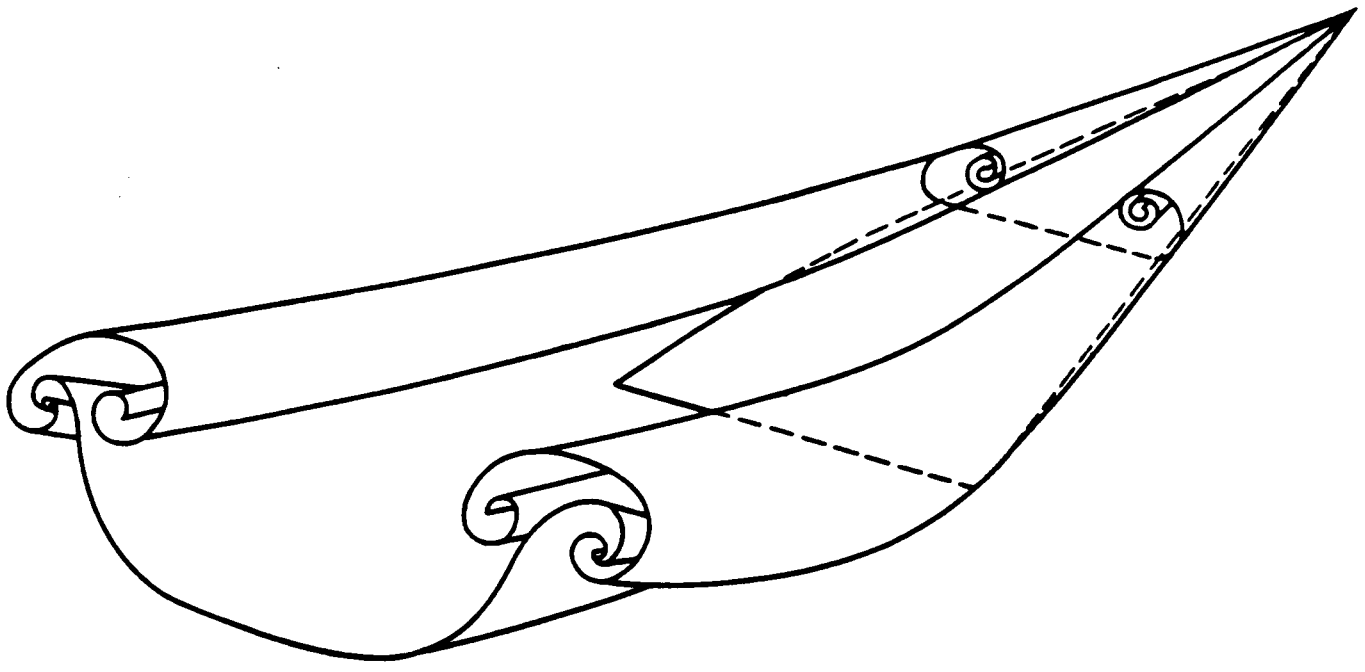

(a) Plane view

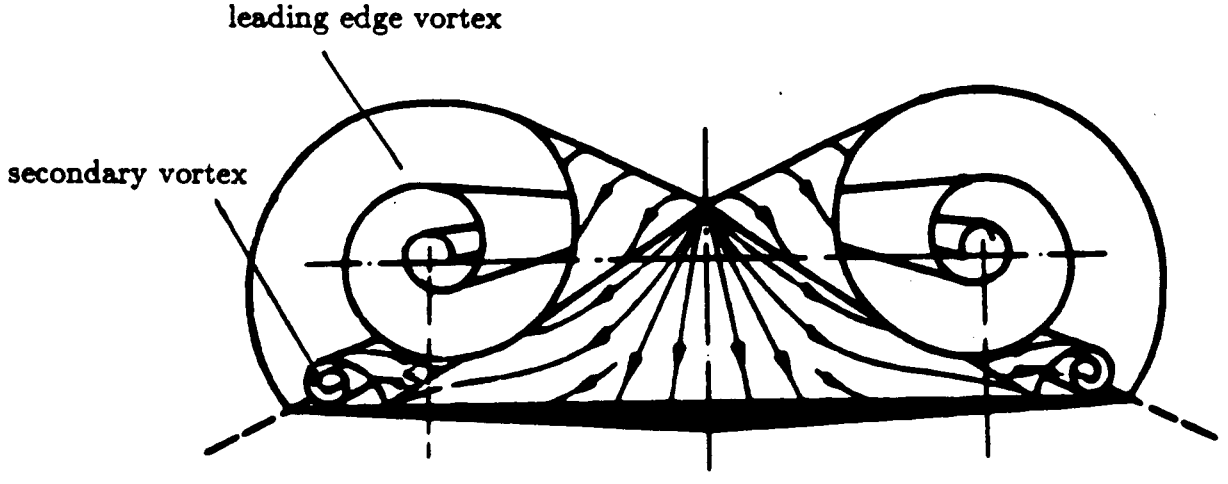

(b) View from the trailing edge

C-2

Fig. 1 Overall flow field past a plane delta wing

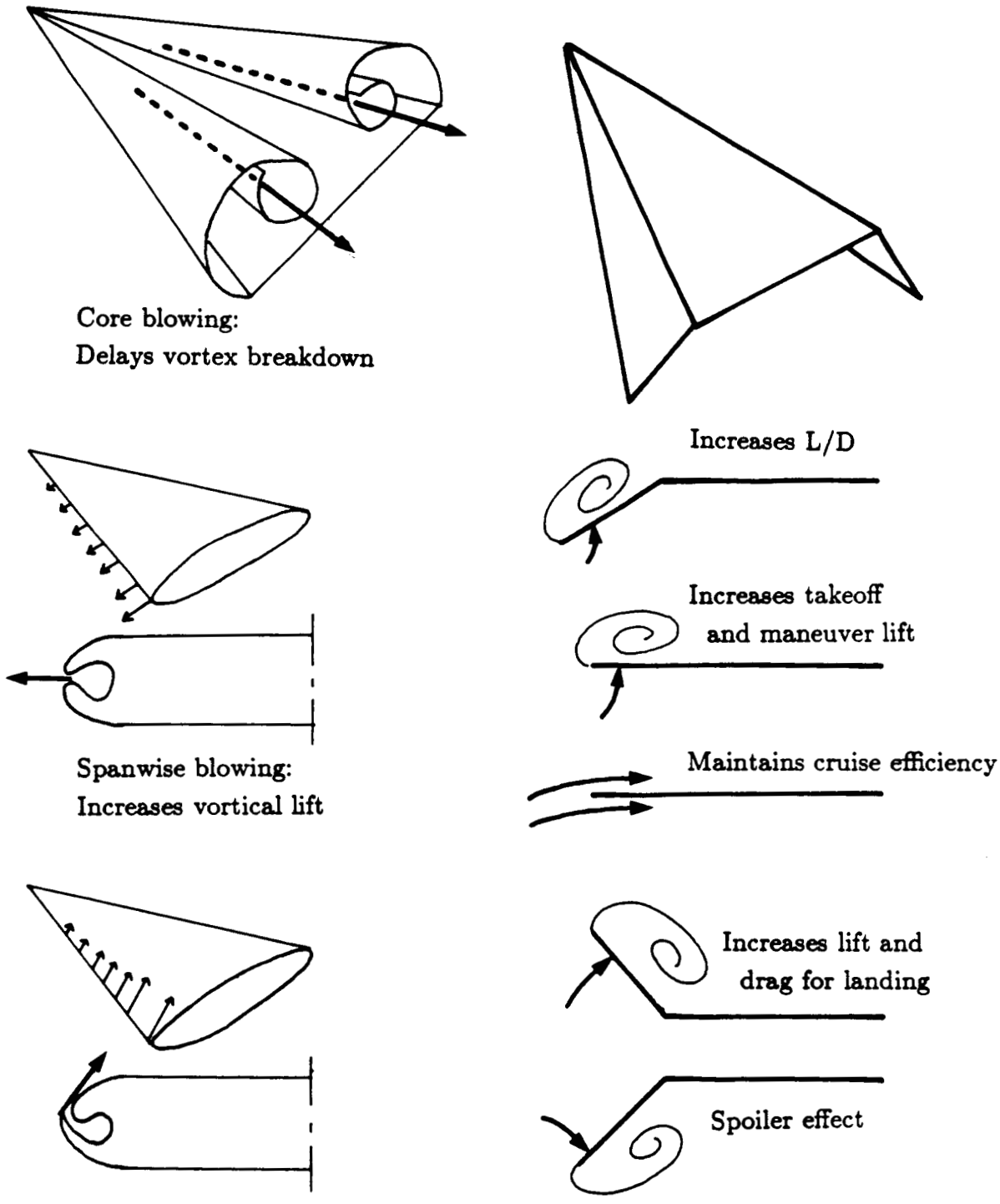

Fig. 2 Concepts for controlling the vortical flow

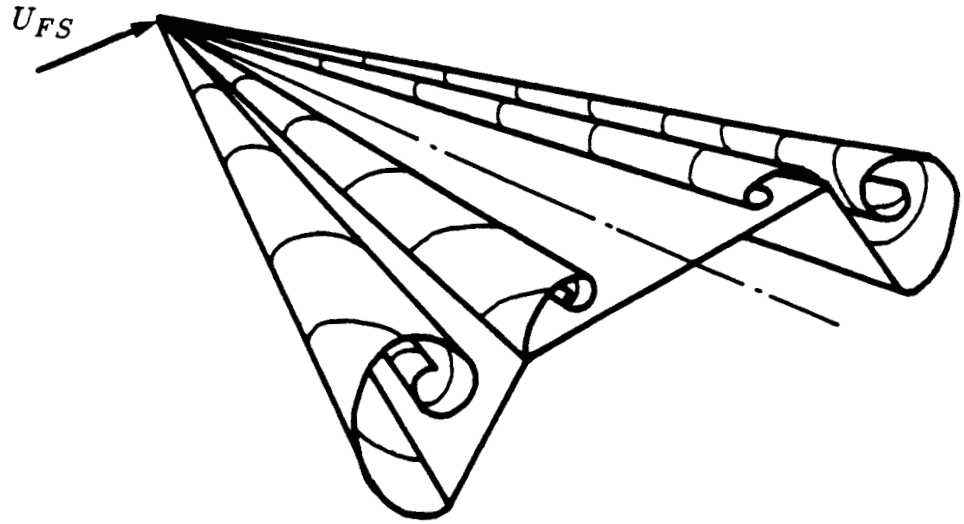

Fig. 3 Simplified flow field past a flapped delta wing

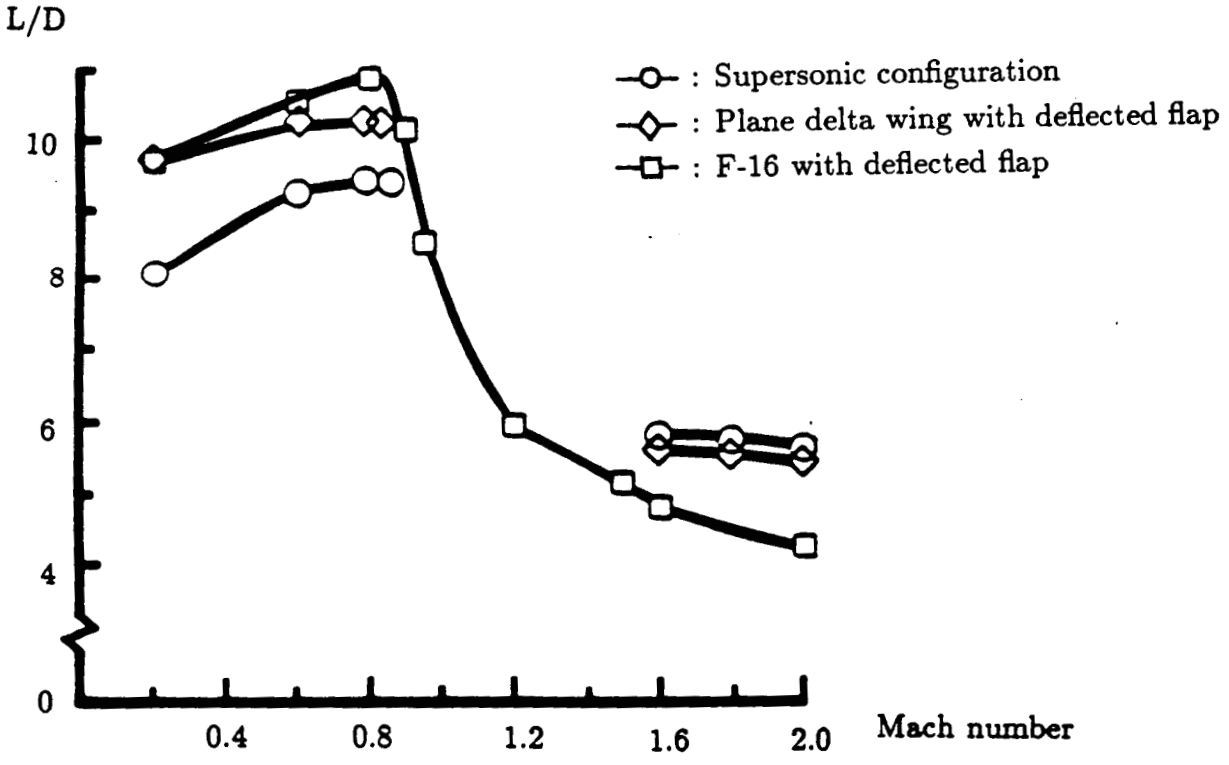

Fig. 4 Comparison of L/D for three different wing configurations, taken form Ref. 2

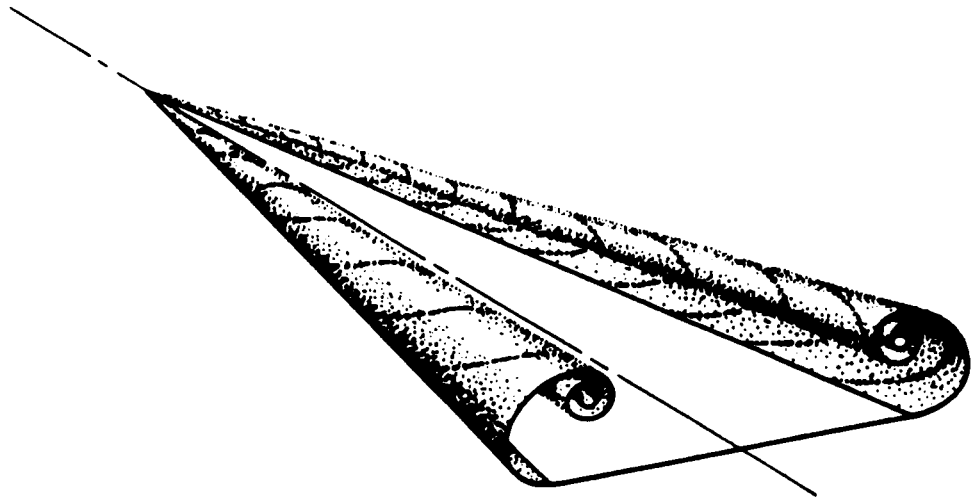

(a) Assumed flow field

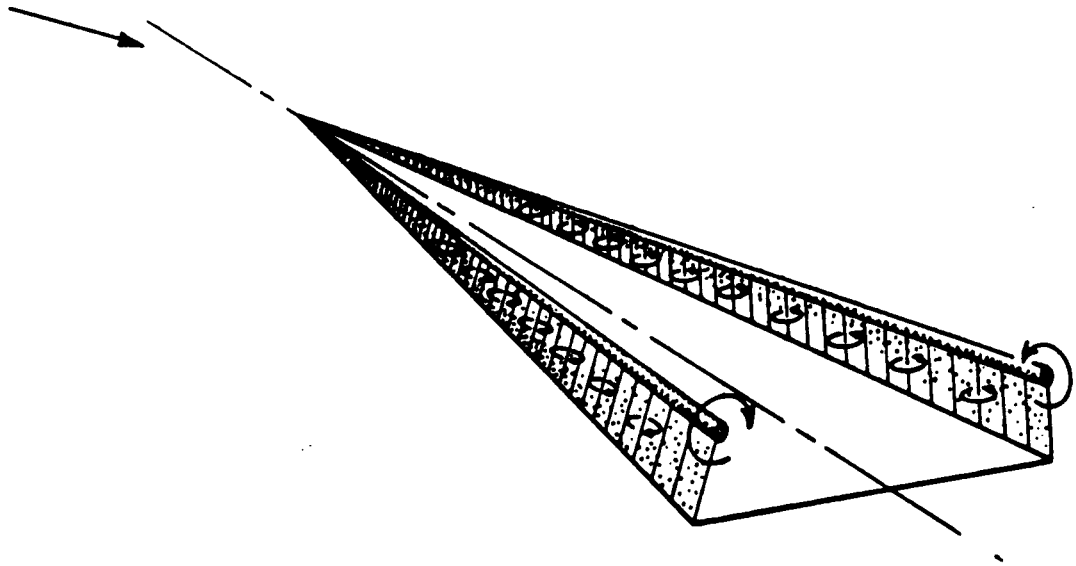

(b) Approximated flow field

Fig. 5 Brown and Michael's approximation of the vortical flow, taken from Ref. 21

ORIGINAL PAGE IS
OF POOR QUALITY

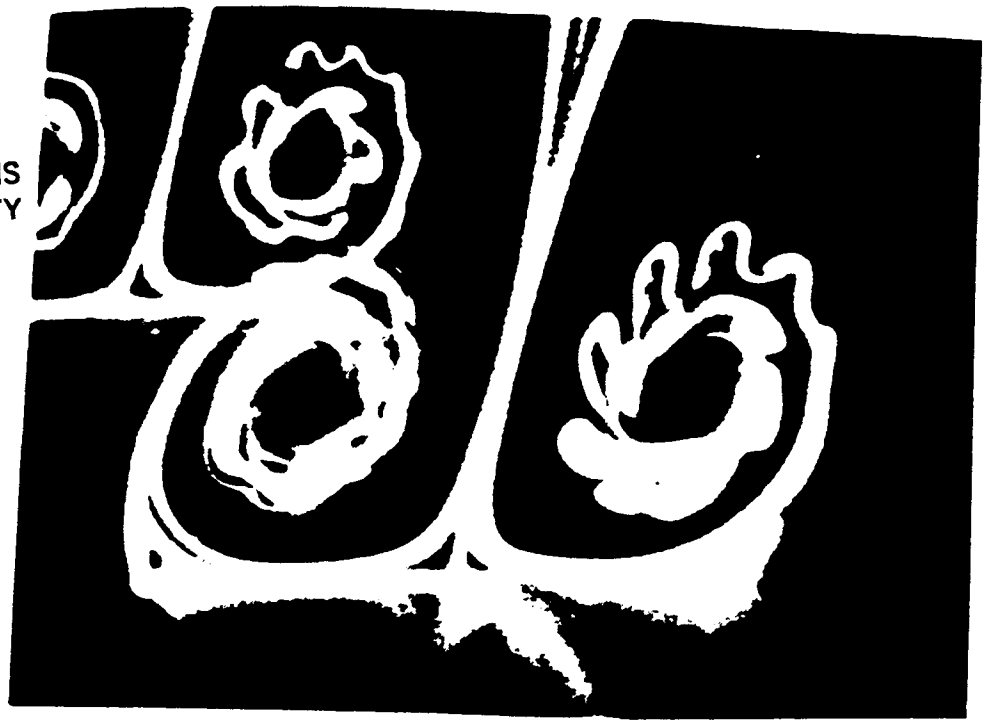

(a) Leading edge vortices, taken from Ref. 77

(b) Plane mixing layer, taken from Ref. 98

Fig. 6 Characteristics of the shear layer structure of leading edge vortices compared with the plane mixing layer

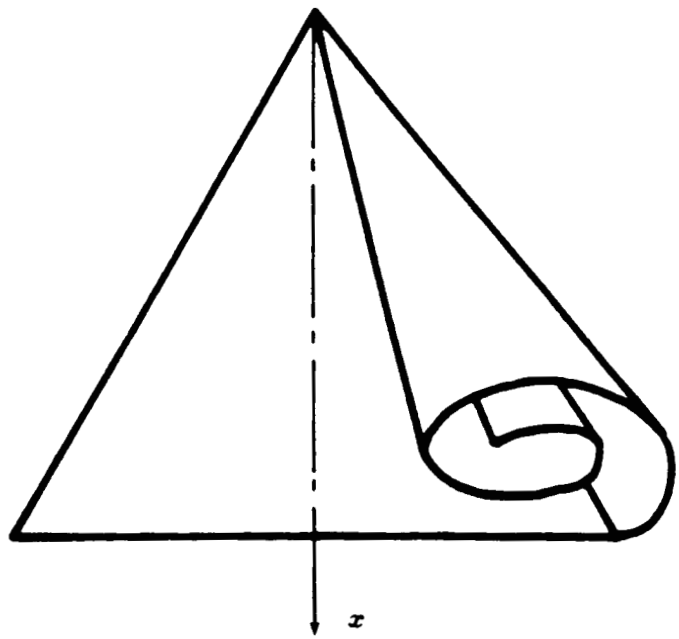

(a) 3-D Conical vortex sheet

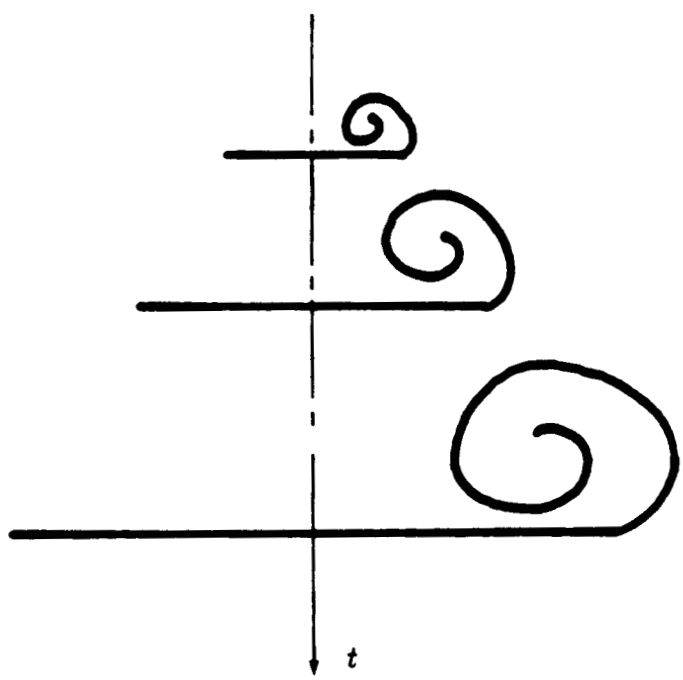

(b) 2-D unsteady self-similar vortex sheet

Fig. 7 Conical and 2-D unsteady vortex sheets

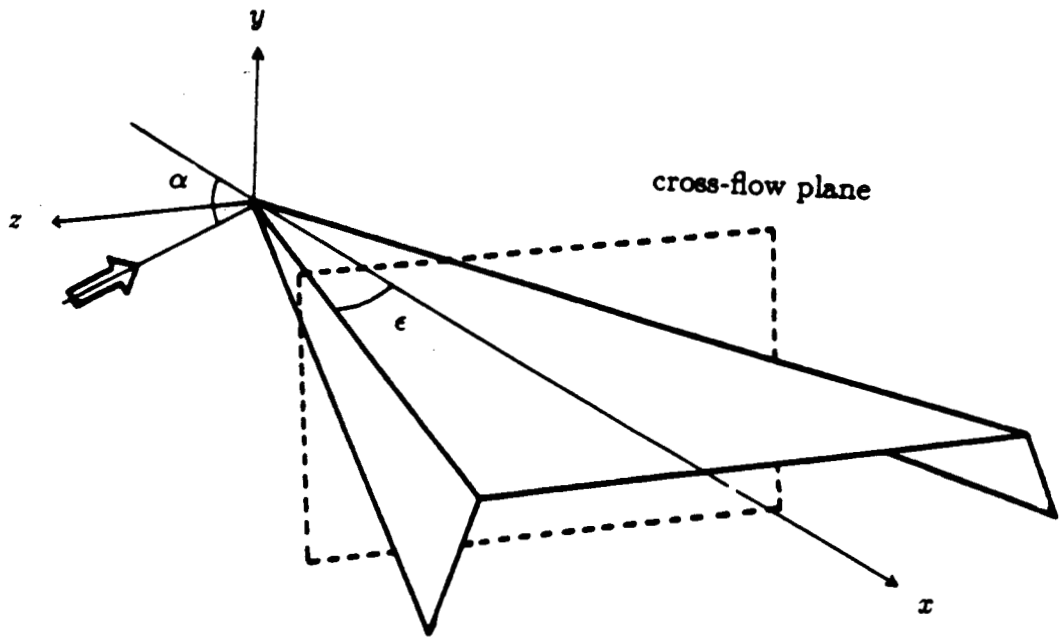

(a) Delta wing coordinate system

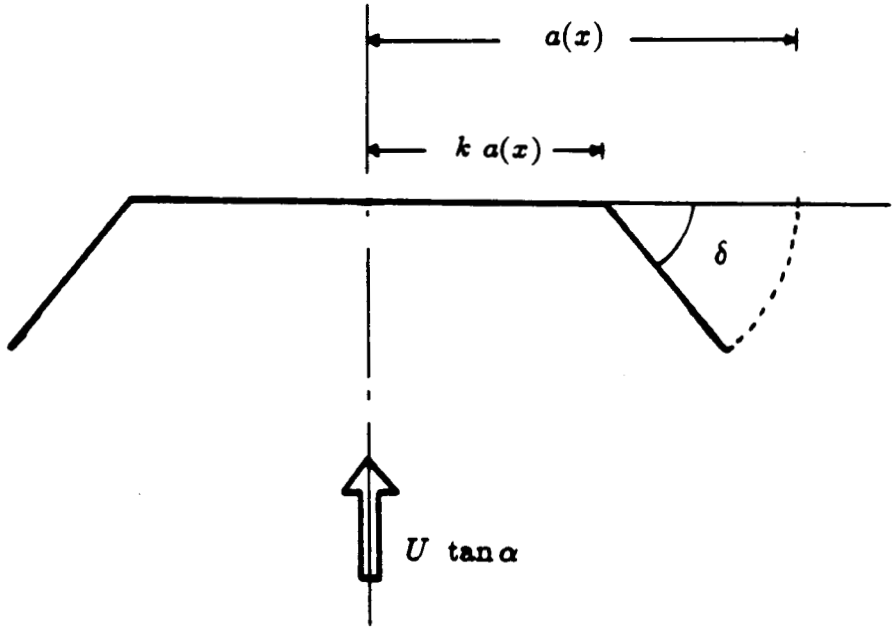

(b) Cross-flow plane

Fig. 8 Geometry of flapped delta wing

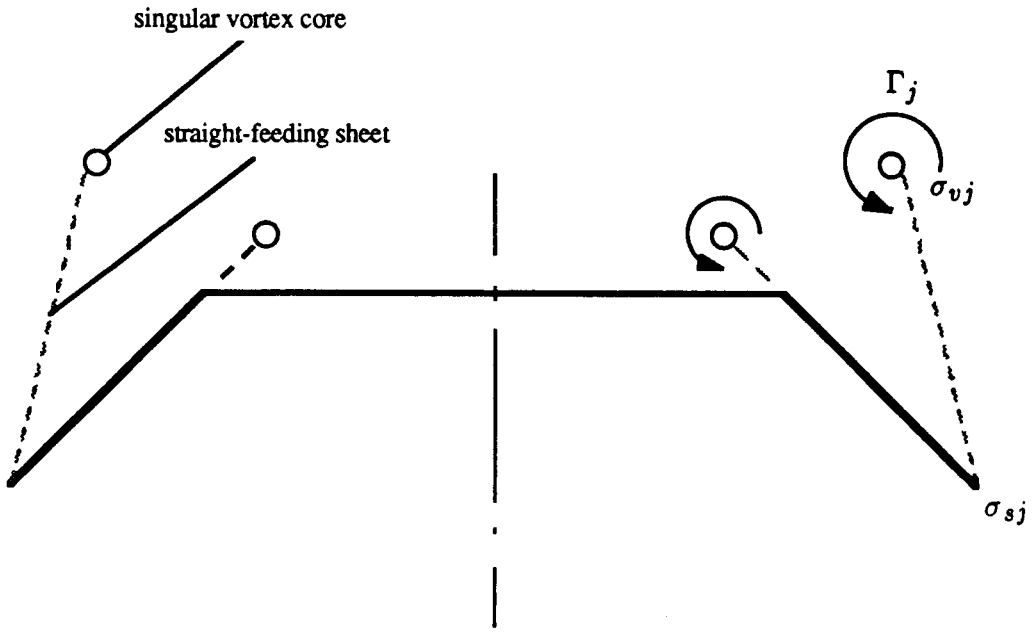

Fig. 9 Straight-feeding-sheet model

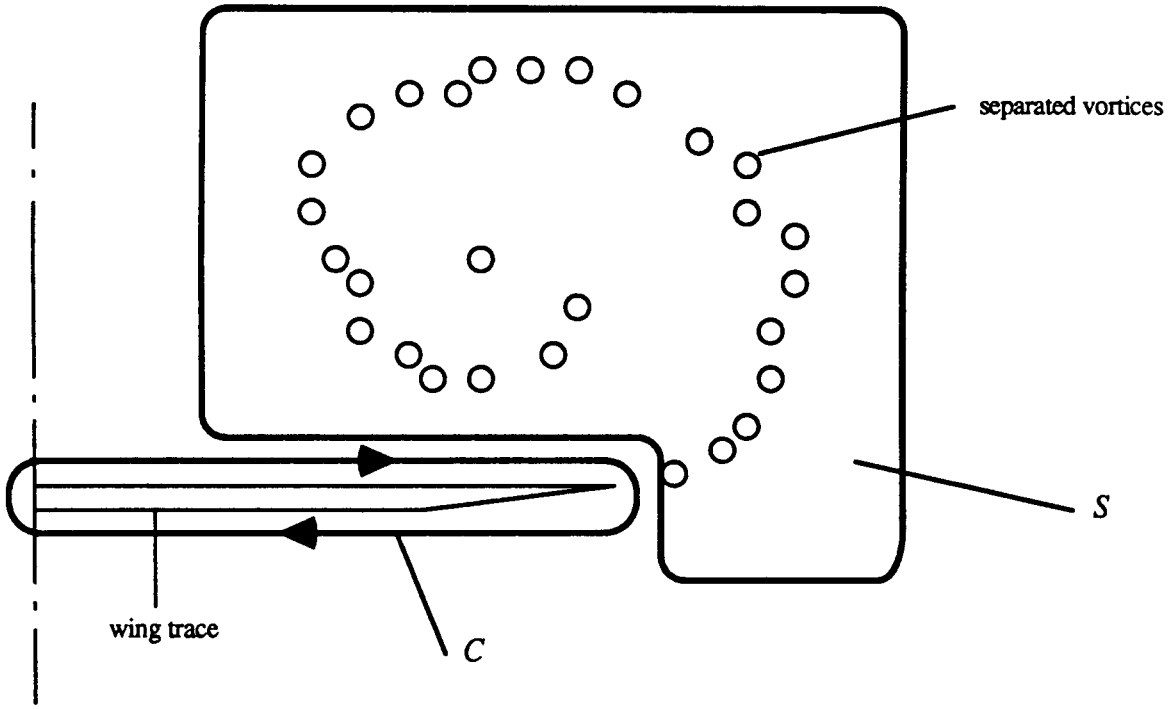

Fig. 10 Integration contours for the definition of circulation

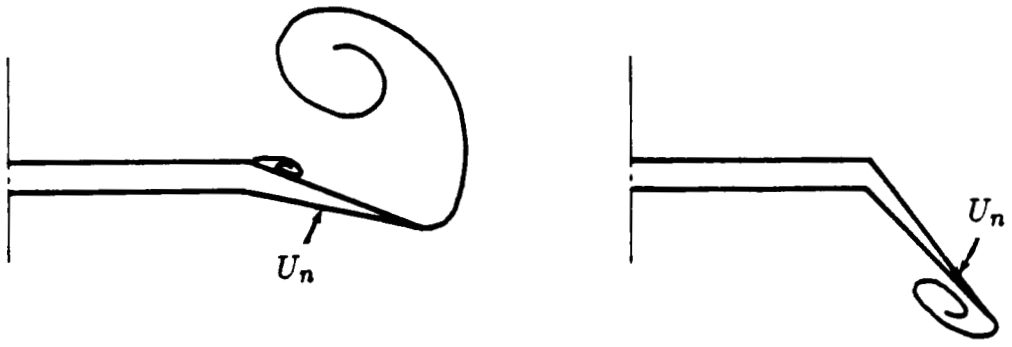

(a) Below limit angle (b) Above limit angle

Fig. 11 Shear layer location for different flap angle

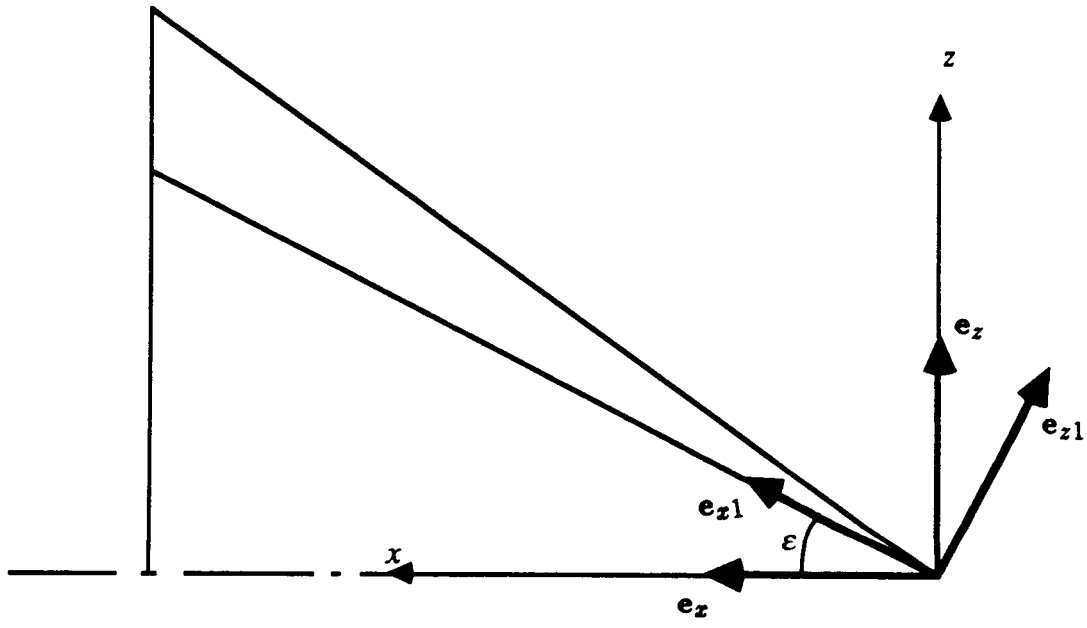

(a) Rotation about the centerline

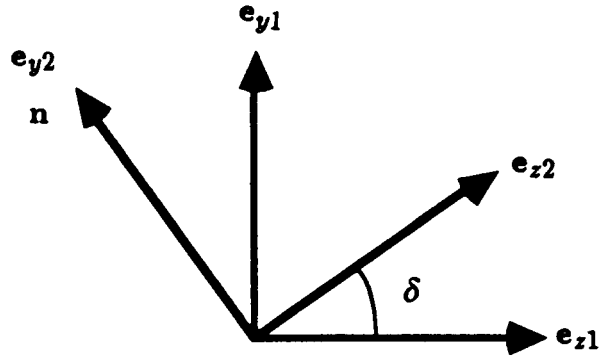

(b) Rotation about the hinge line

Fig. 12 Coordinate transformation procedure for vector normal to flap surface

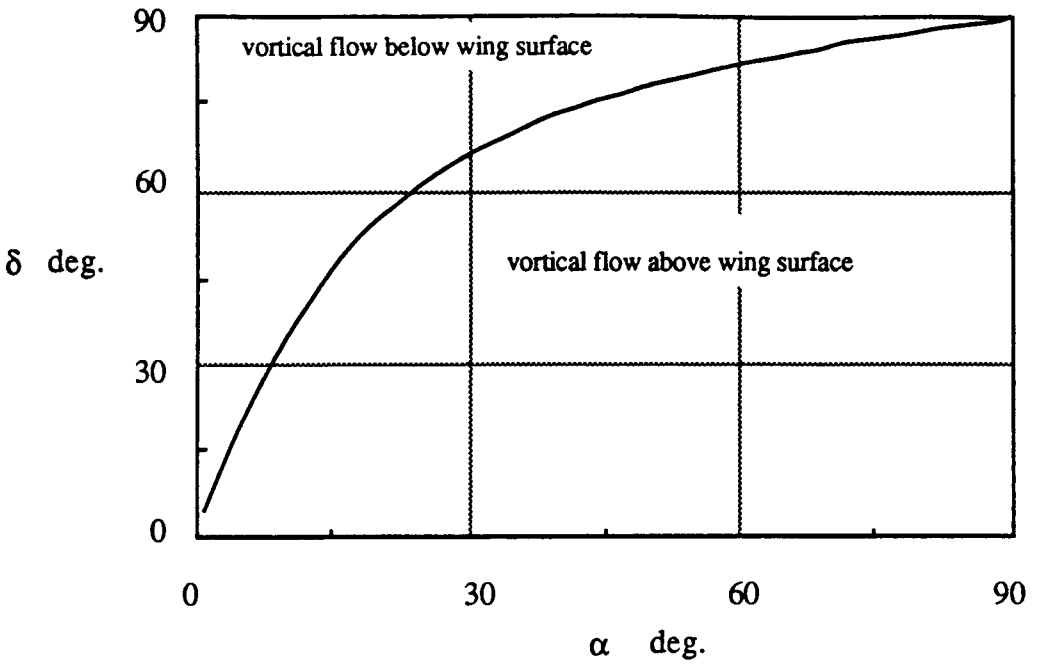

Fig. 13 Boundary of flap deflection angle, $\epsilon = 15$ deg.

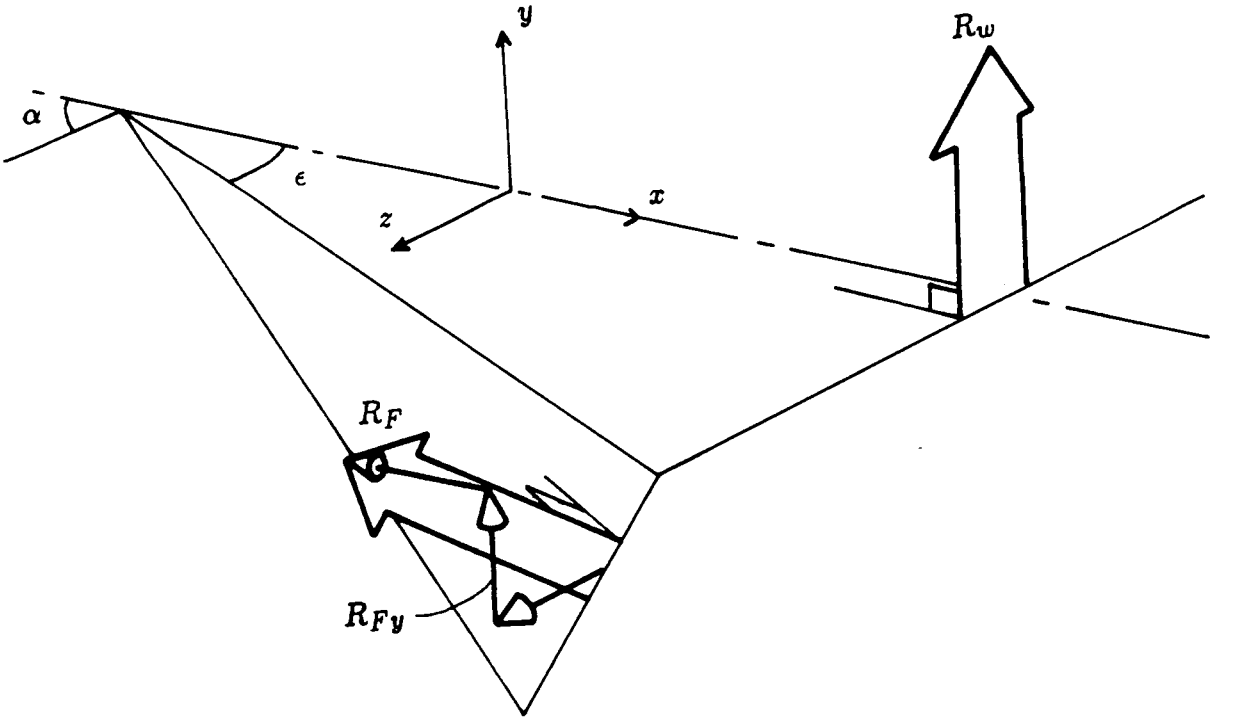

Fig. 14 Force components on wing and flap surfaces

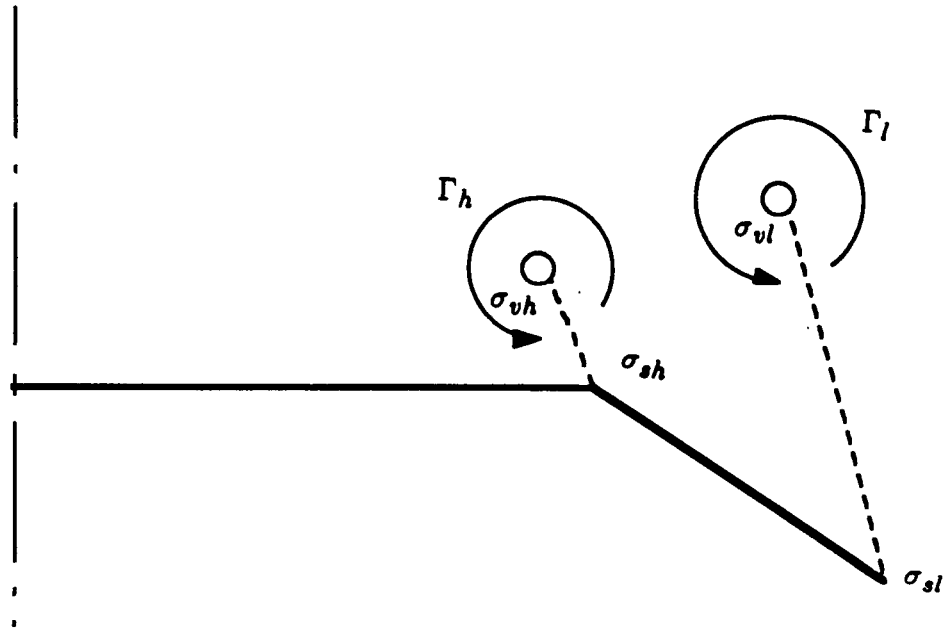

Fig. 15 Approximated flow field singularities in the cross-flow plane

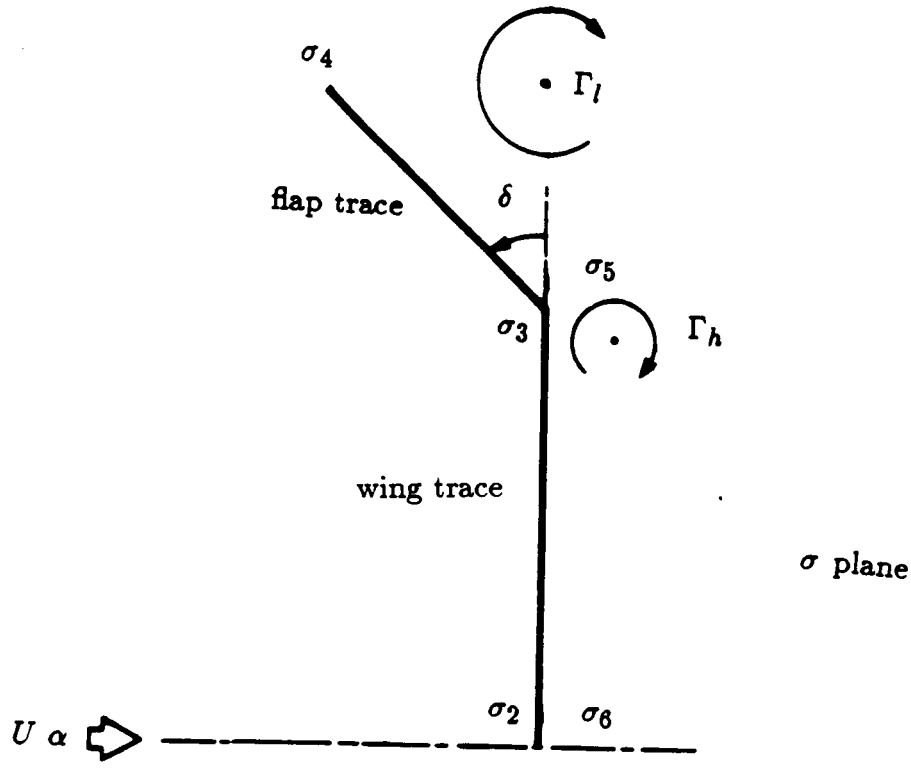

(a) Physical plane

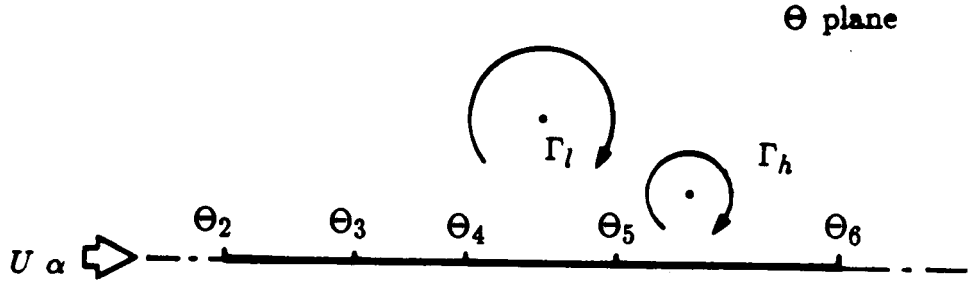

(b) Transformed plane

Fig. 16 Mapping procedure

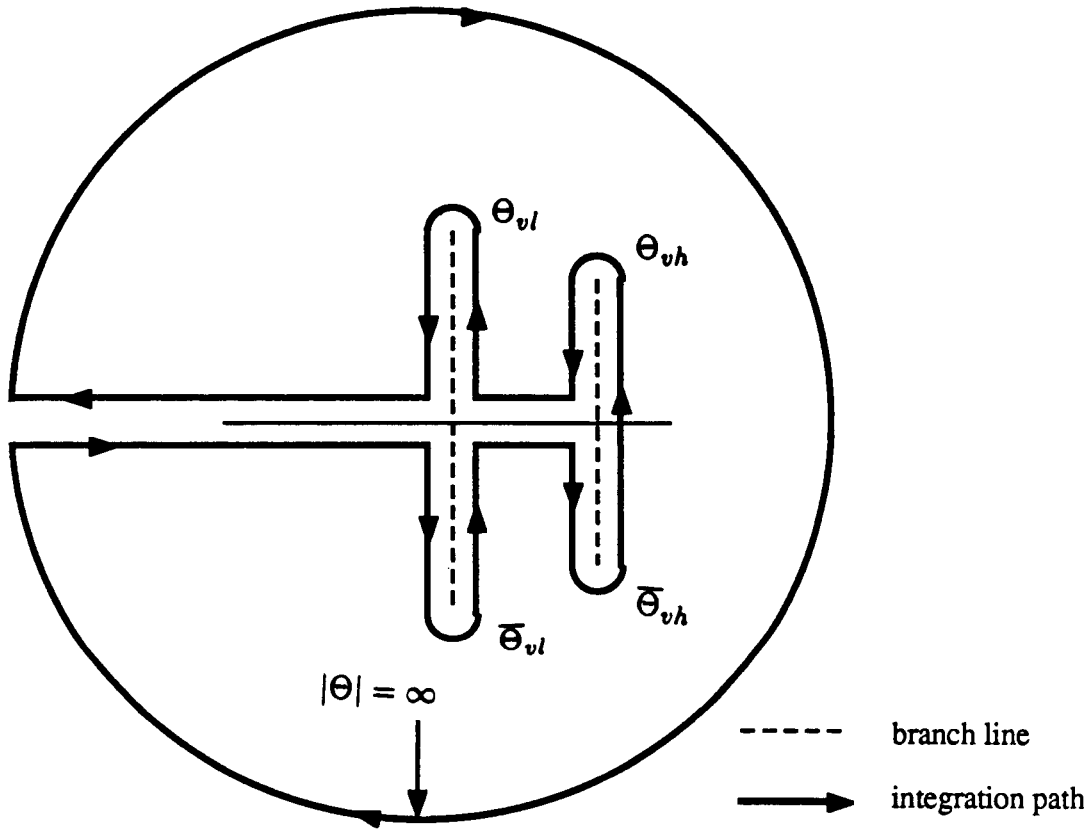

Fig. 17 Integration path for vortex+sheet systems

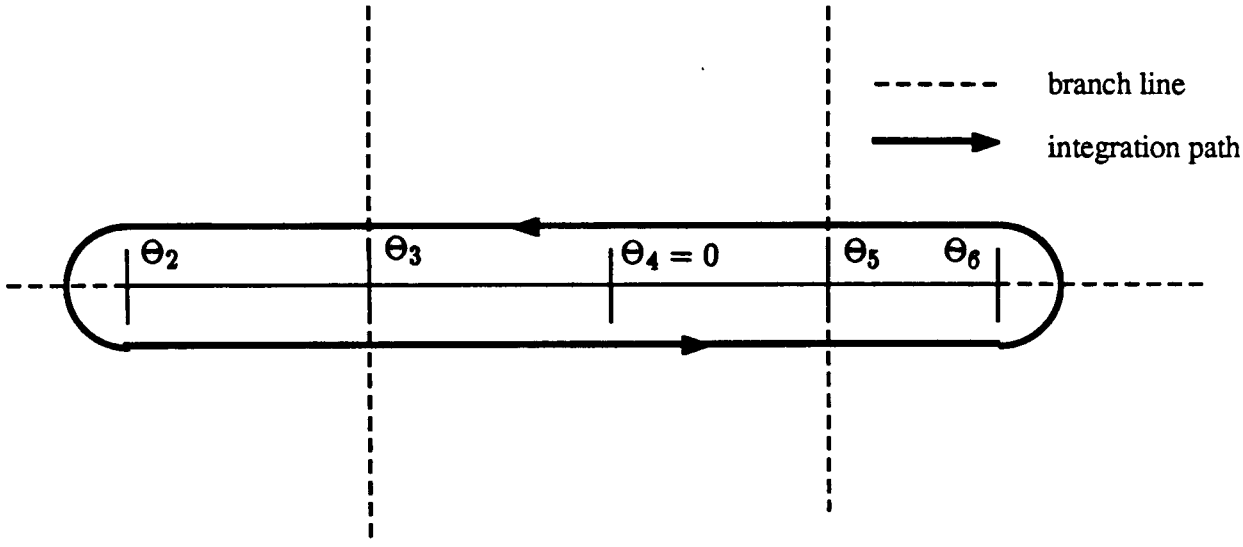

Fig. 18 Integration path along the wing trace

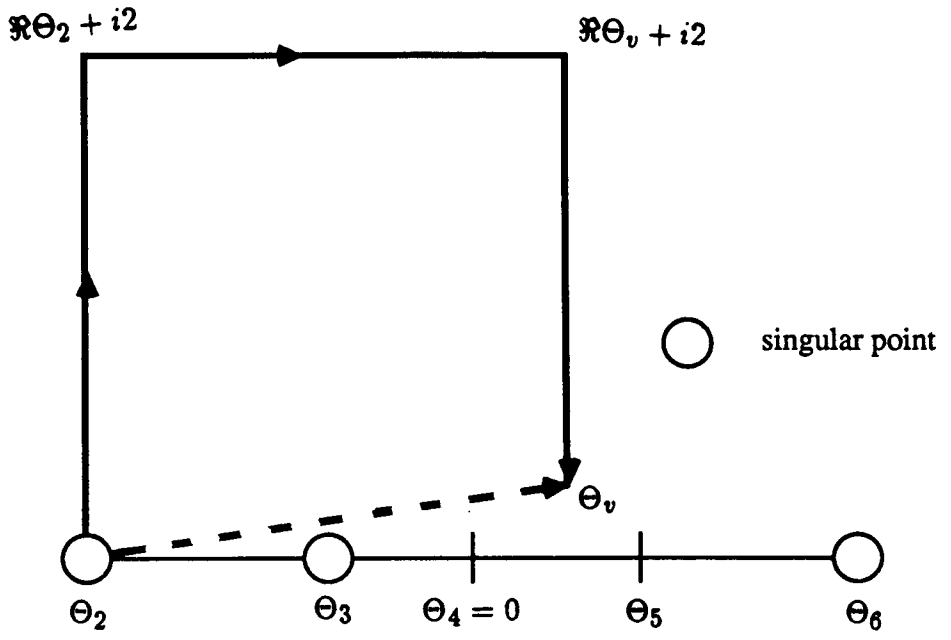

Fig. 19 Integration path for the vortex positions

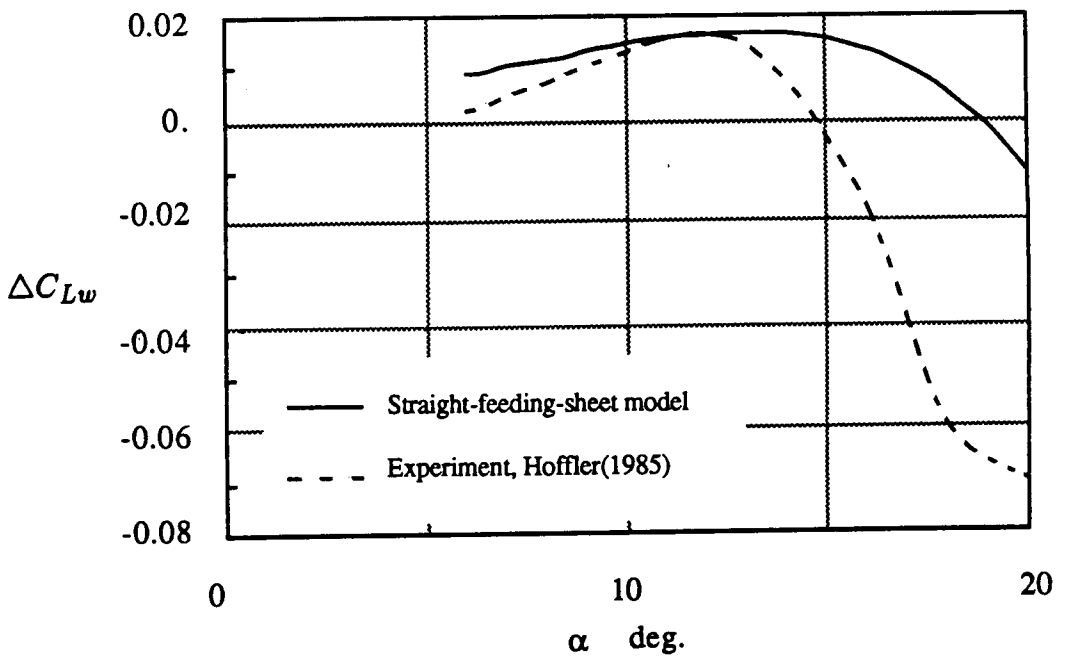

Fig. 20 Lift increment on main wing, $\delta = 40$ deg.

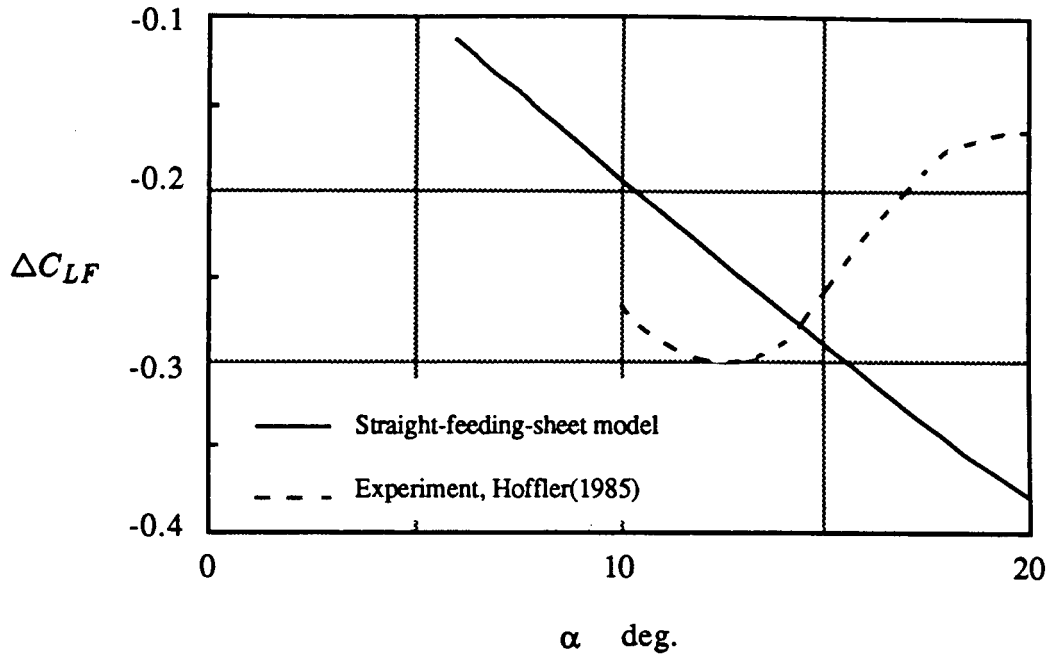

Fig. 21 Lift increment on flap, $\delta = 40$ deg.

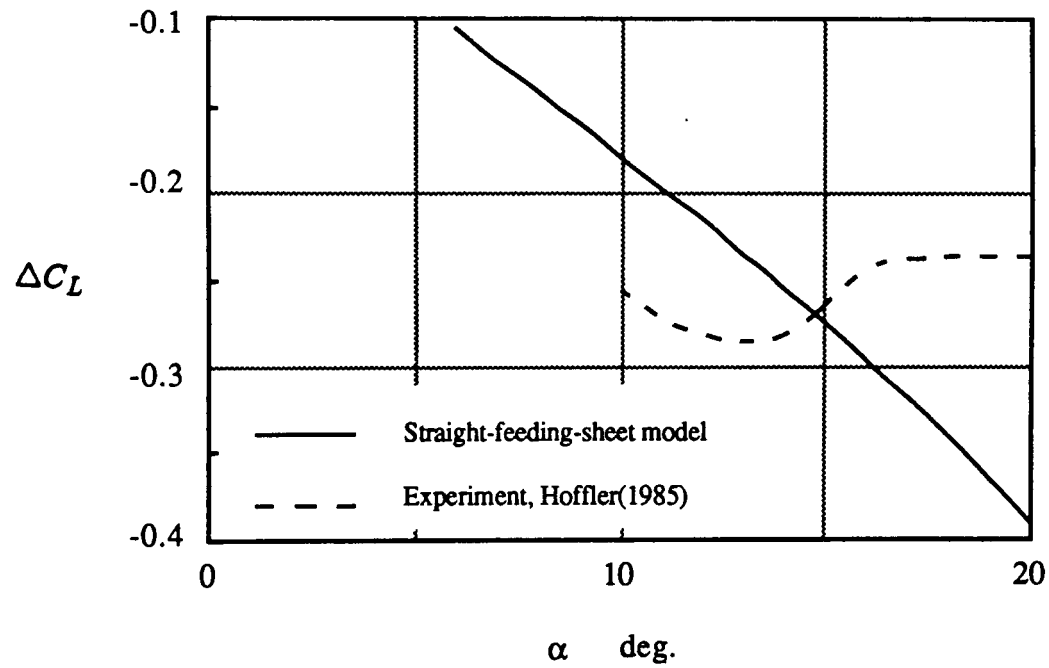

Fig. 22 Total lift increment, $\delta = 40$ deg.

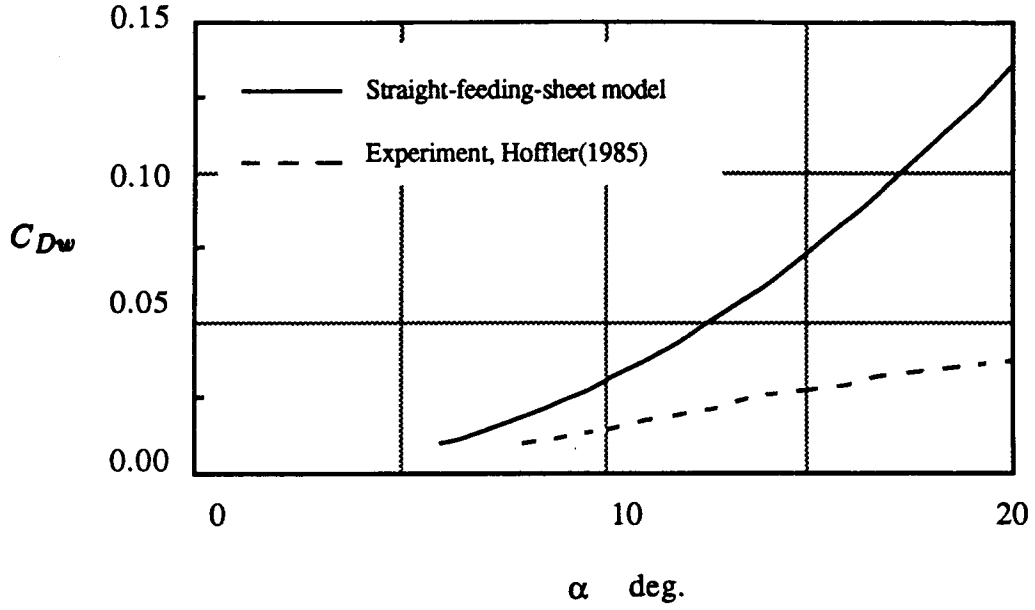

Fig. 23 Drag on main wing, $\delta = 40$ deg.

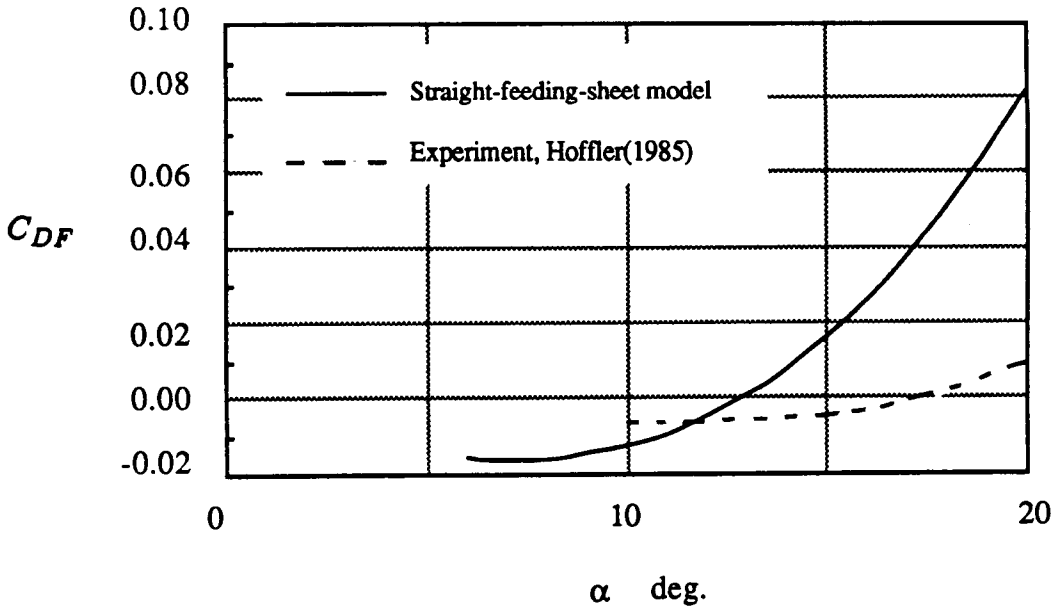

Fig. 24 Drag on flap, $\delta = 40$ deg.

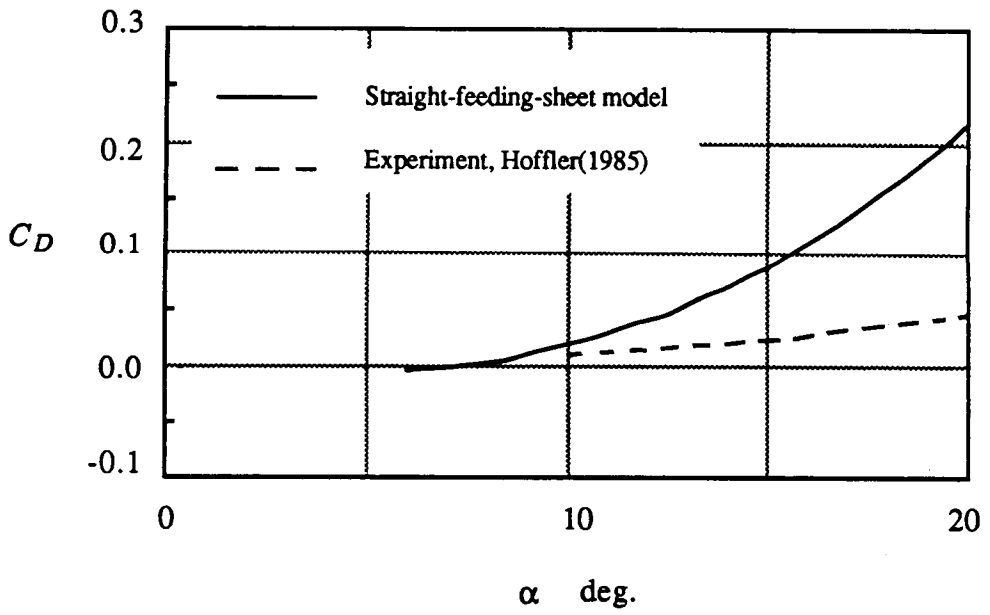

Fig. 25 Total drag, $\delta = 40$ deg.

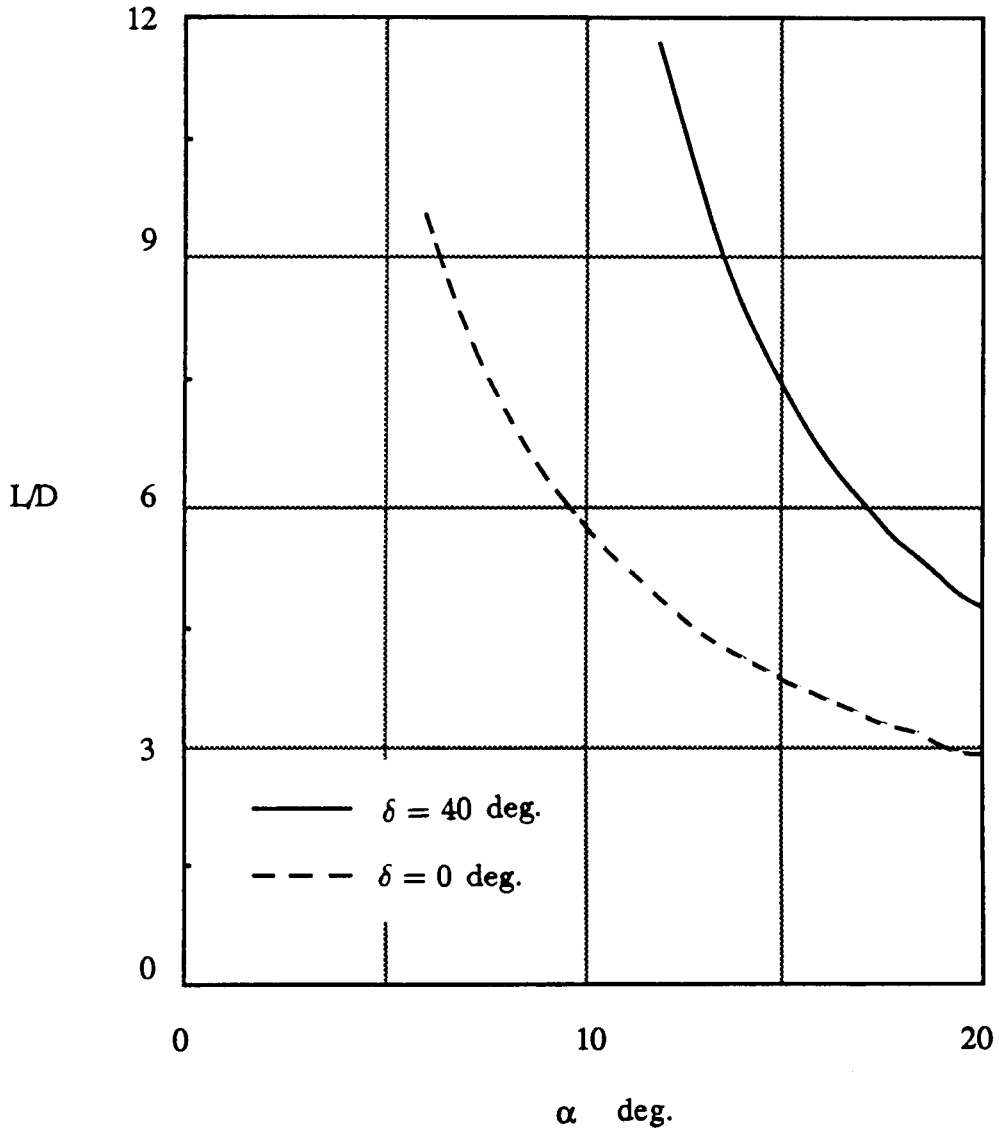

Fig. 26 Lift-to-Drag ratio

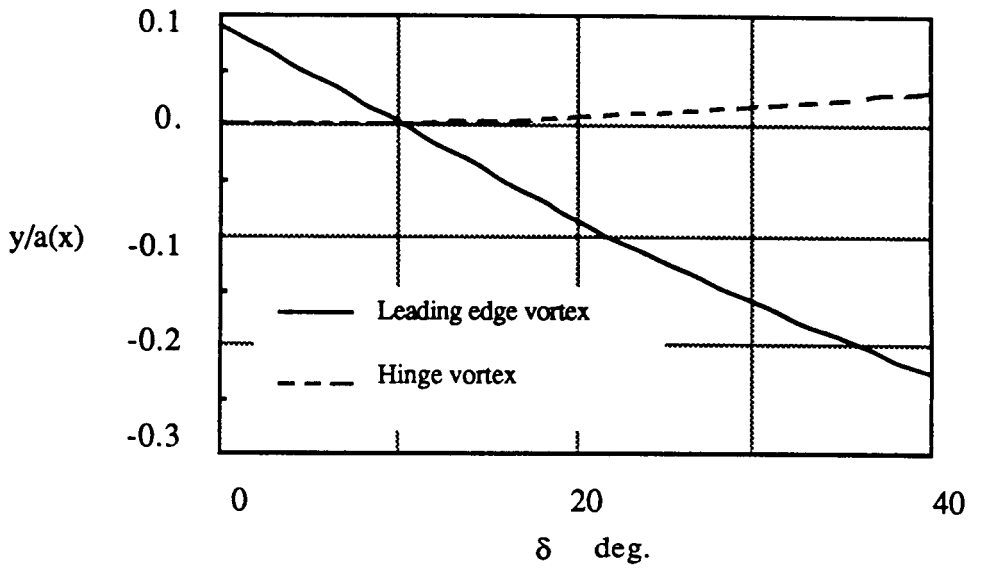

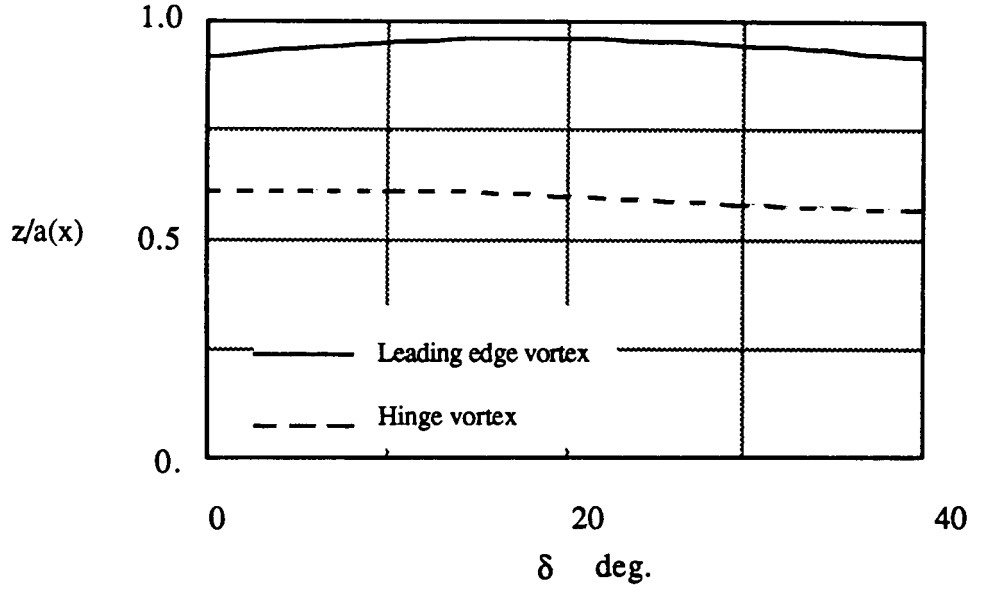

Fig. 27 Vortex position variation for $\alpha = 10$ deg.

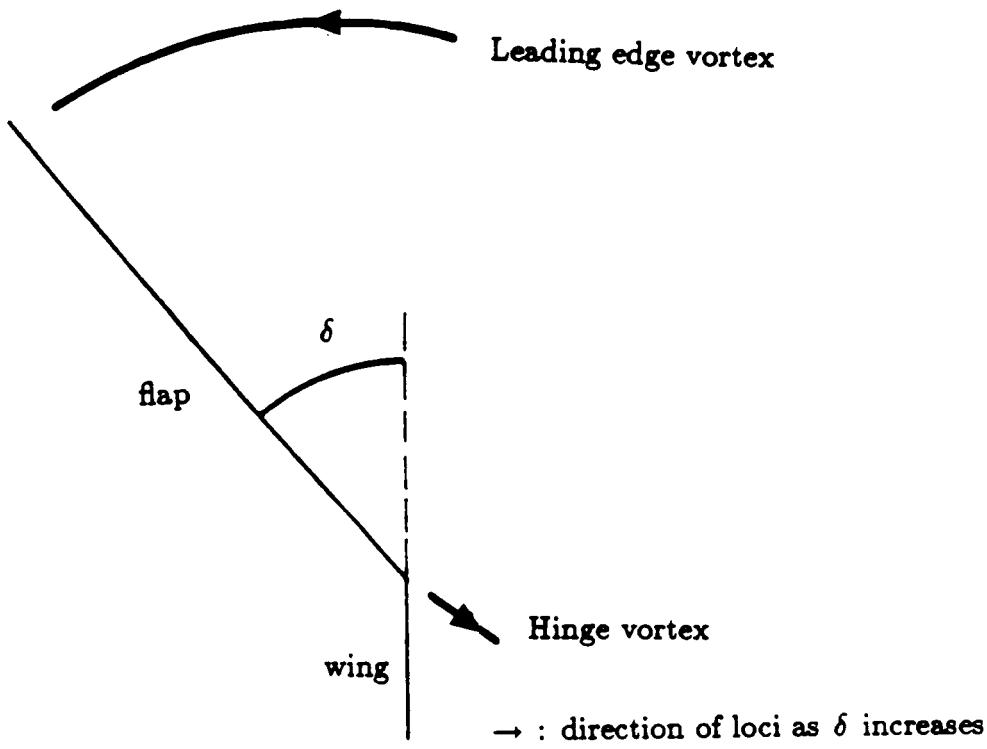

Fig. 28 Vortex loci in physical plane

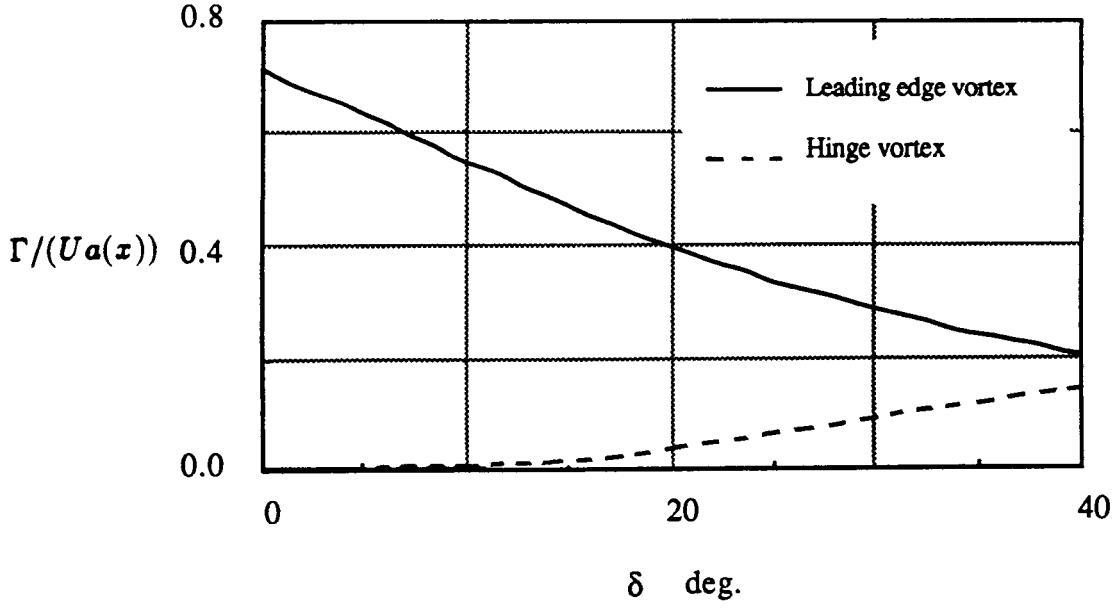

Fig. 29 Vortex strength variation for $\alpha = 10$ deg.

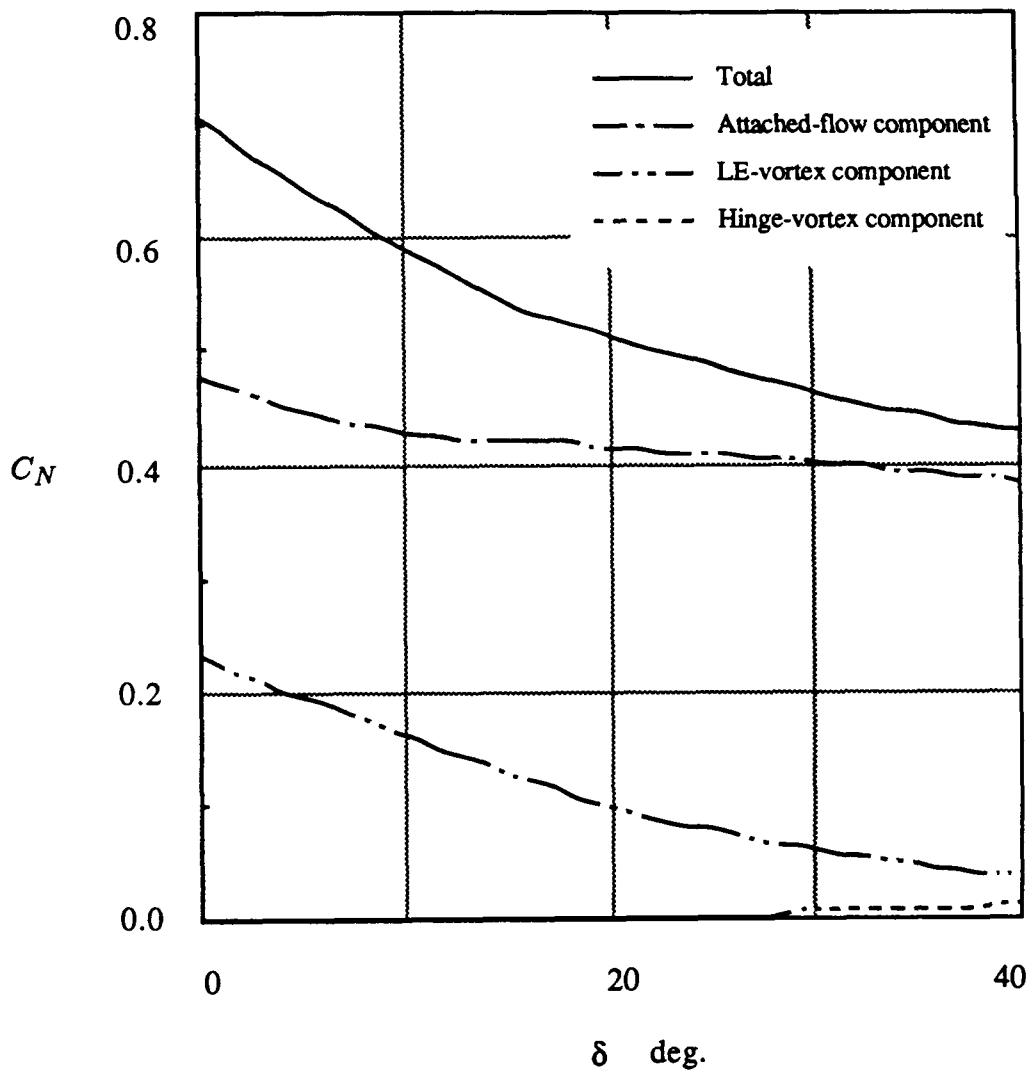

Fig. 30 Normal force components for $\alpha = 10$ deg.

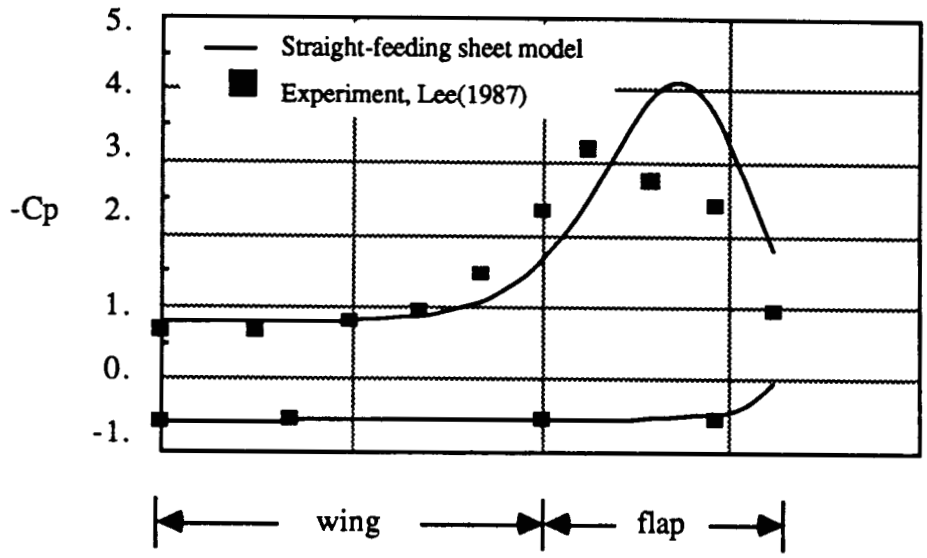

Fig. 31 Surface pressure distribution for $\alpha = 25$ deg., $\delta = 0$ deg.

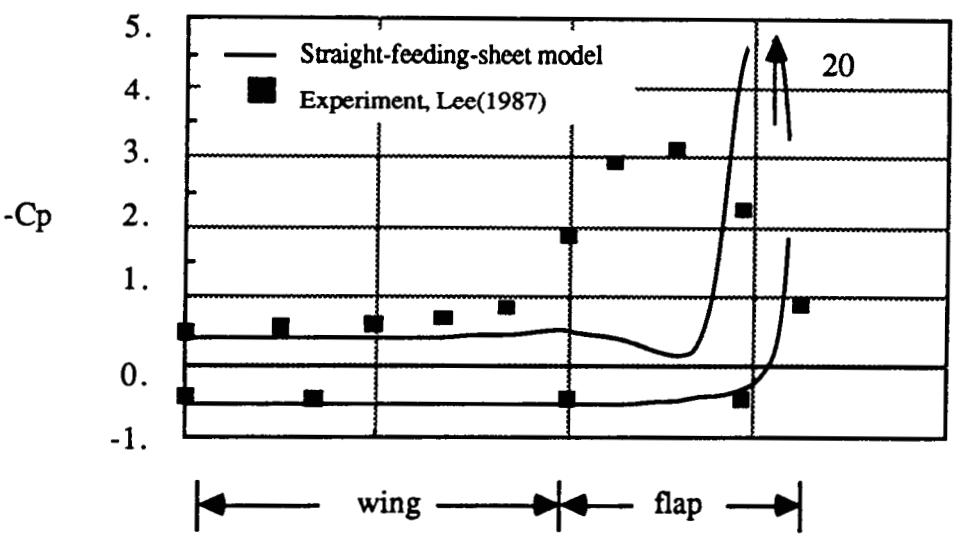

Fig. 32 Surface pressure distribution for $\alpha = 25$ deg., $\delta = 15$ deg.

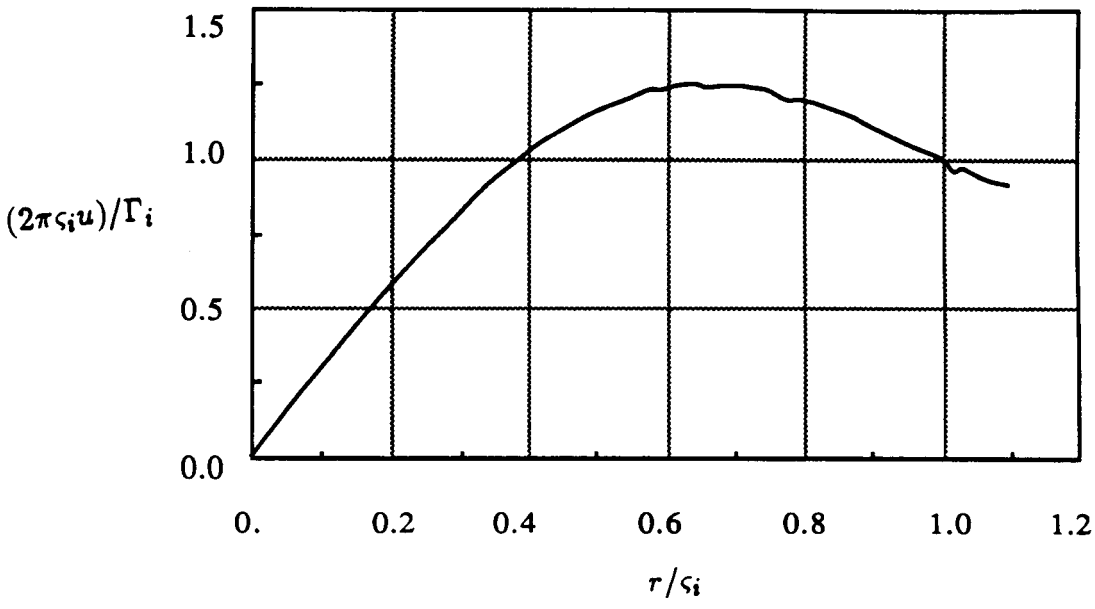

(a) Velocity distribution

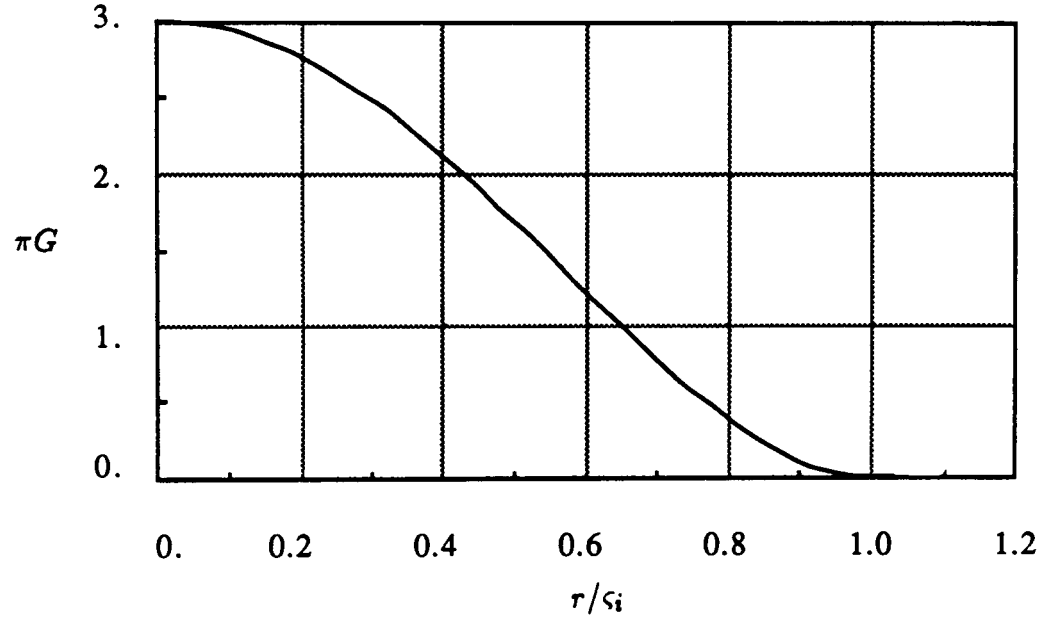

(b) Vorticity distribution

Fig. 33 Spalart's vortex model

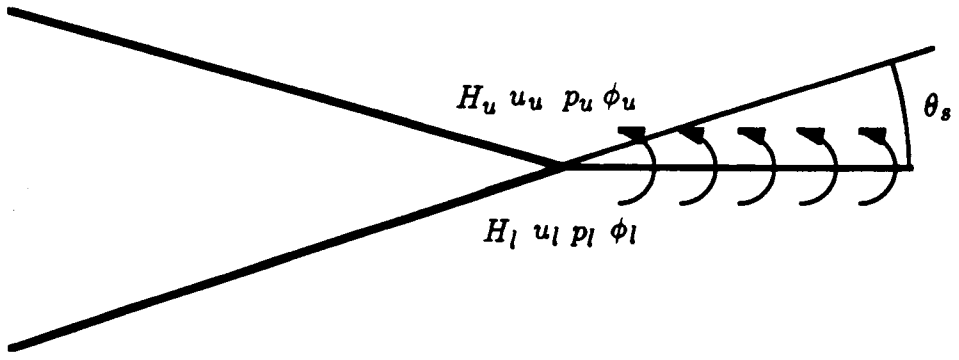

(a) General case

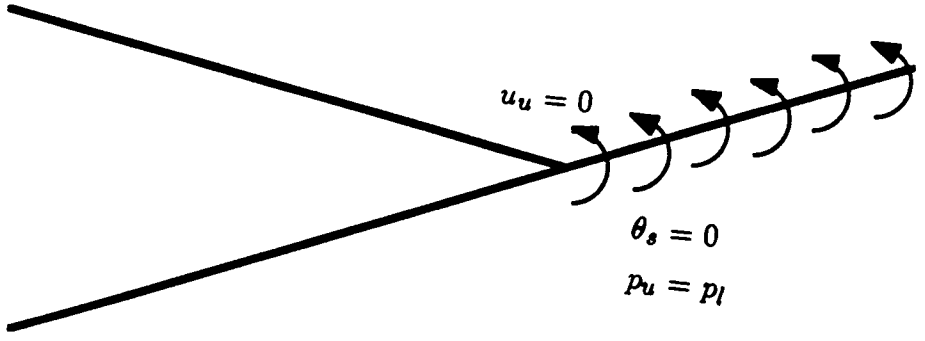

(b) Fixing the separation angle

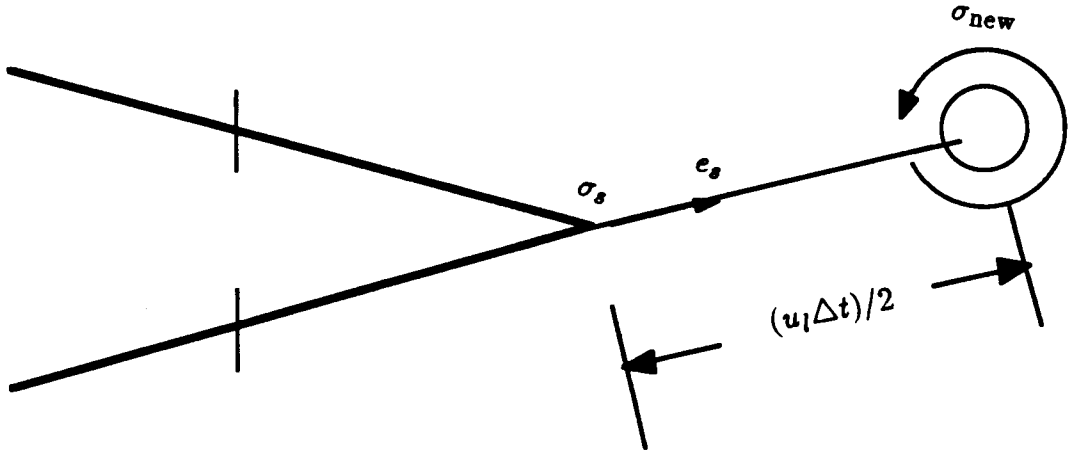

(c) New vortex position

Fig. 34 Flow around the separation point

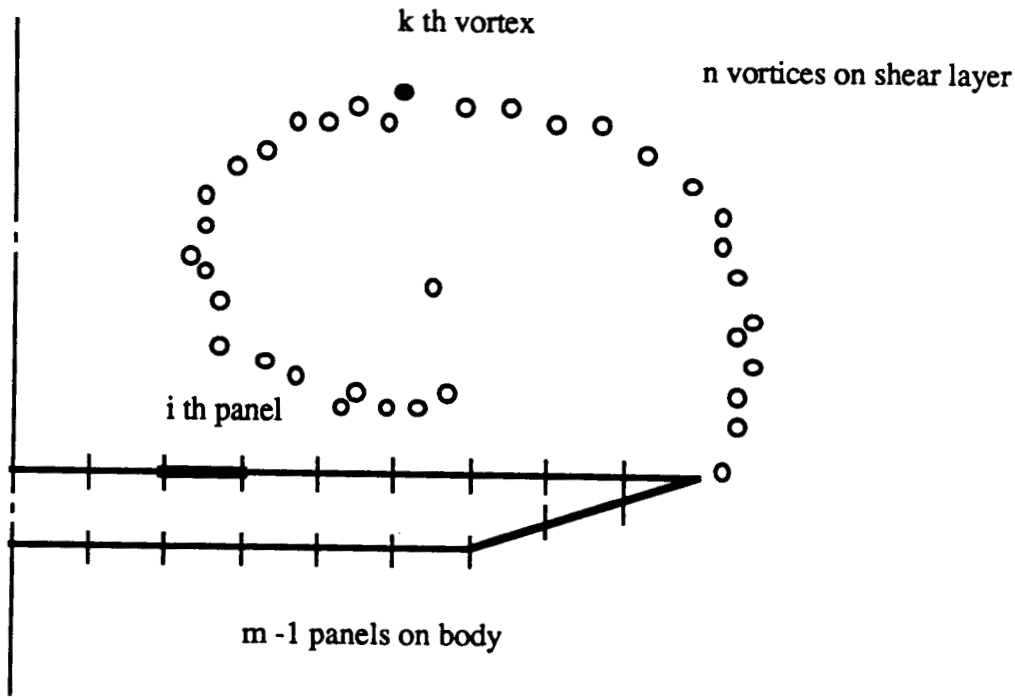

Fig. 35 Body panels and wake vortices

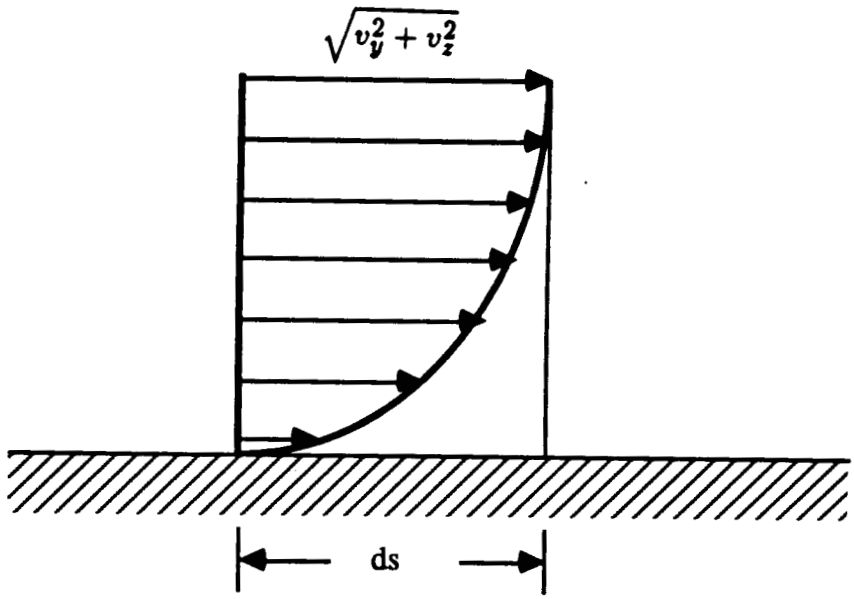

Fig. 36 Boundary layer and outer velocity

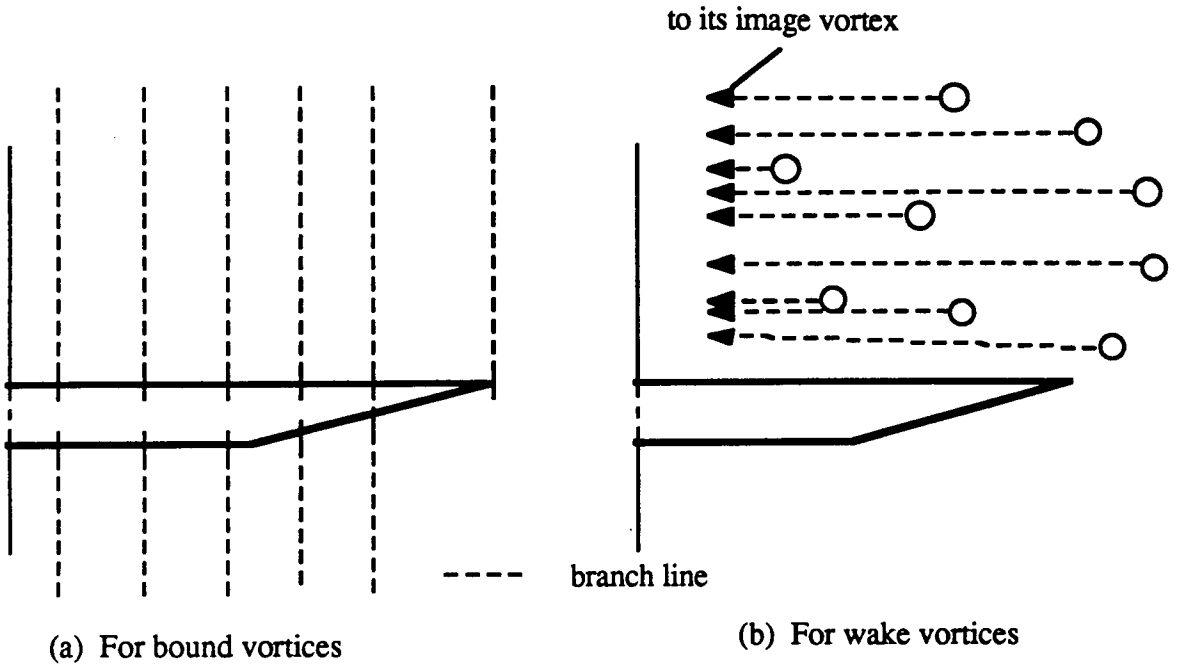

Fig. 37 Branch lines

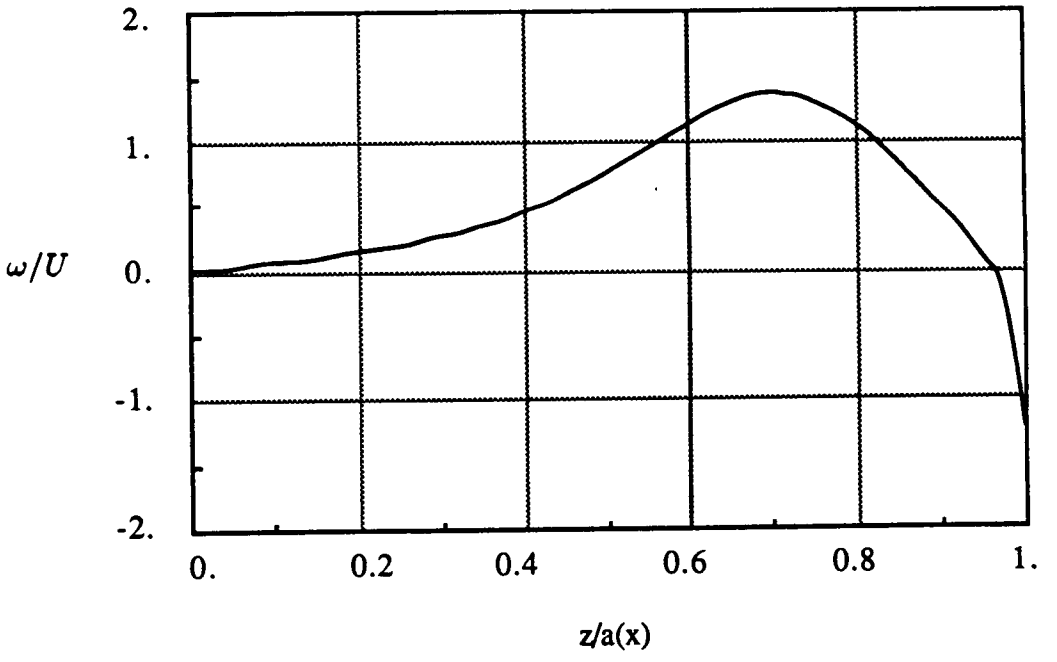

Fig. 38 Chordwise vorticity distribution

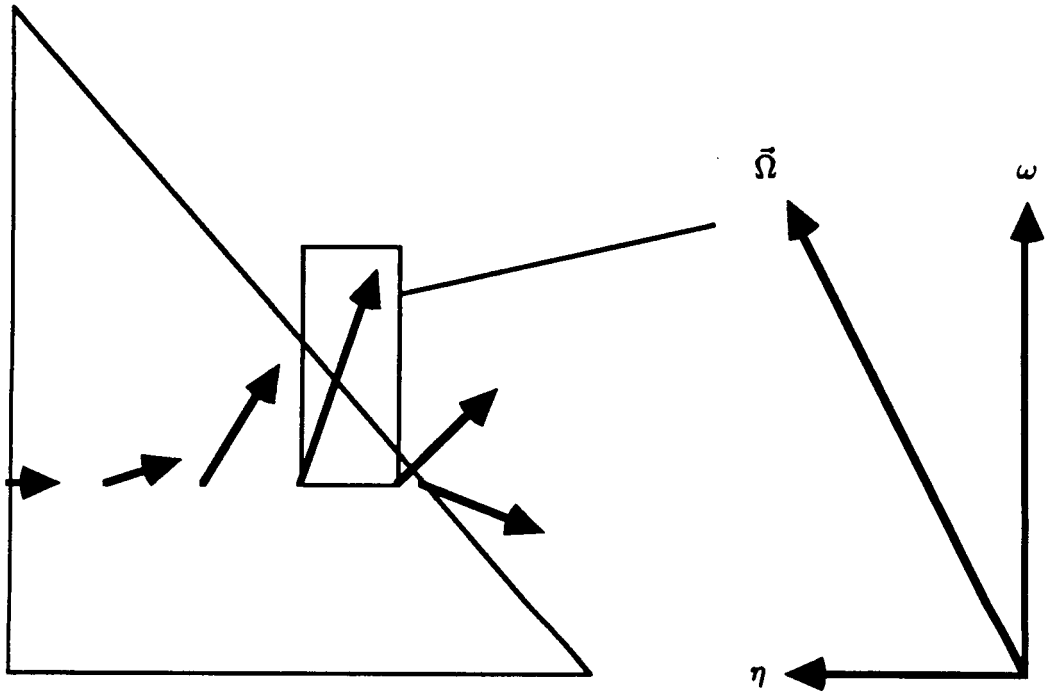

Fig. 39 Bound vorticity components

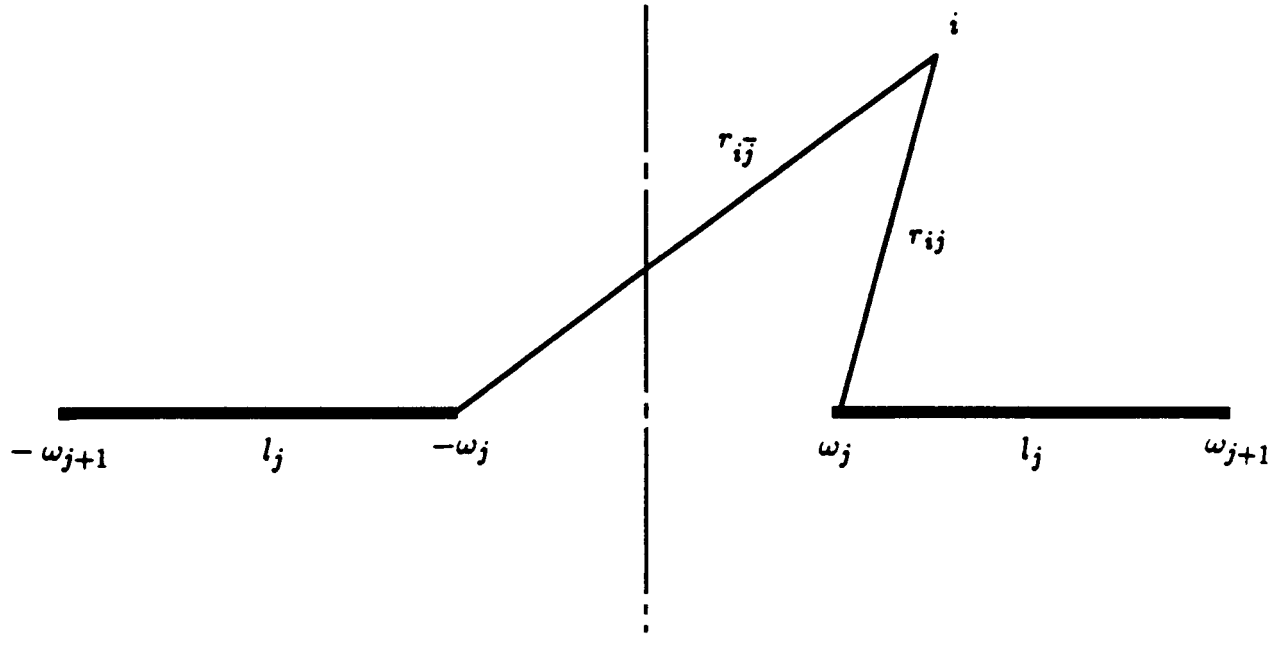

Fig. 40 Stream function induced by body panels

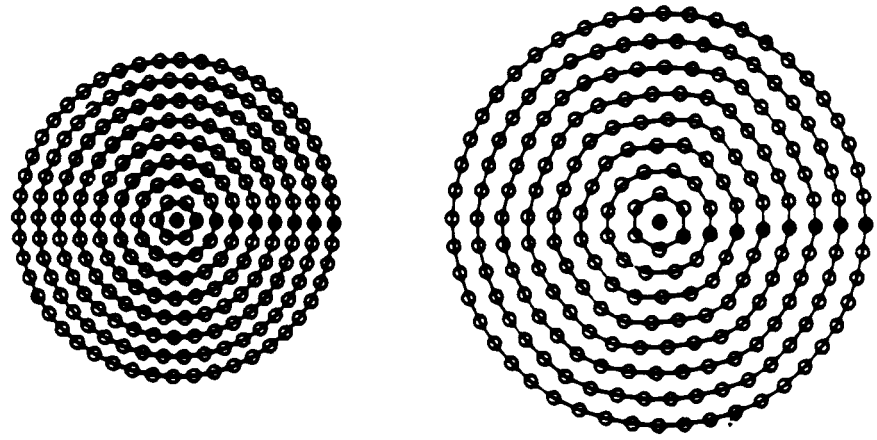

(a) Initial state (b) After some time steps

Fig. 41 Numerical diffusion illustrated by discrete simulation of Rankine vortex, taken from Ref. 65

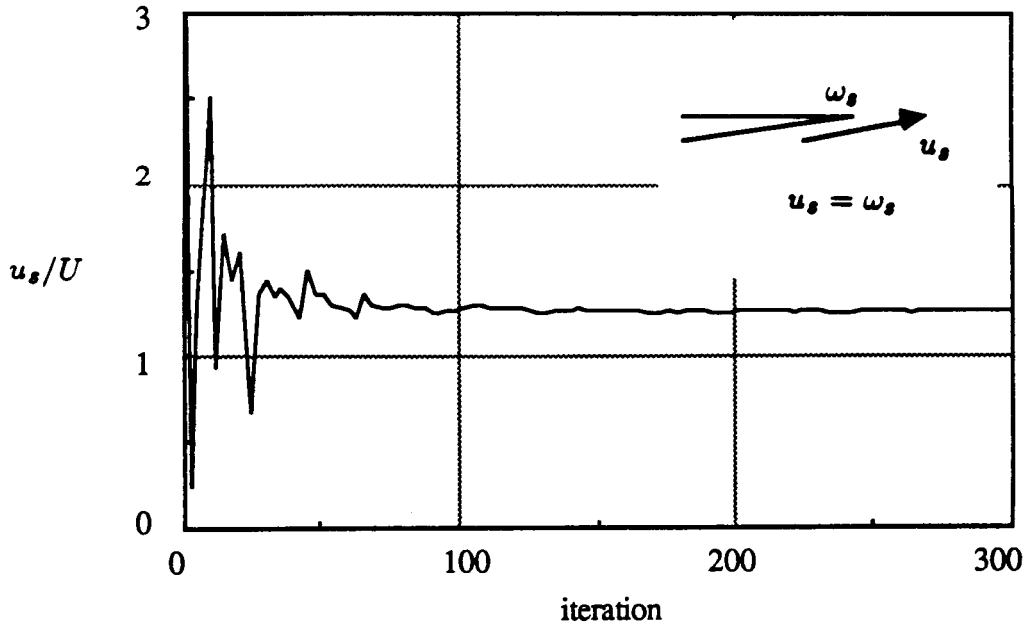

Fig. 42 Convergence of the vorticity intensity at the separation point, initial guess is $3U$

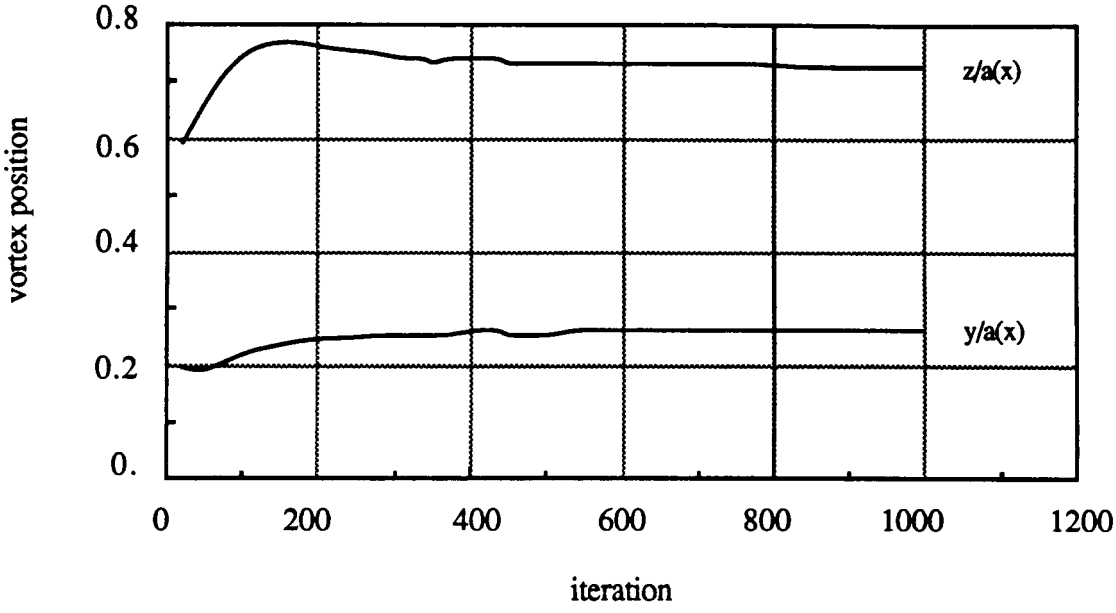

(a) Shear layer core position

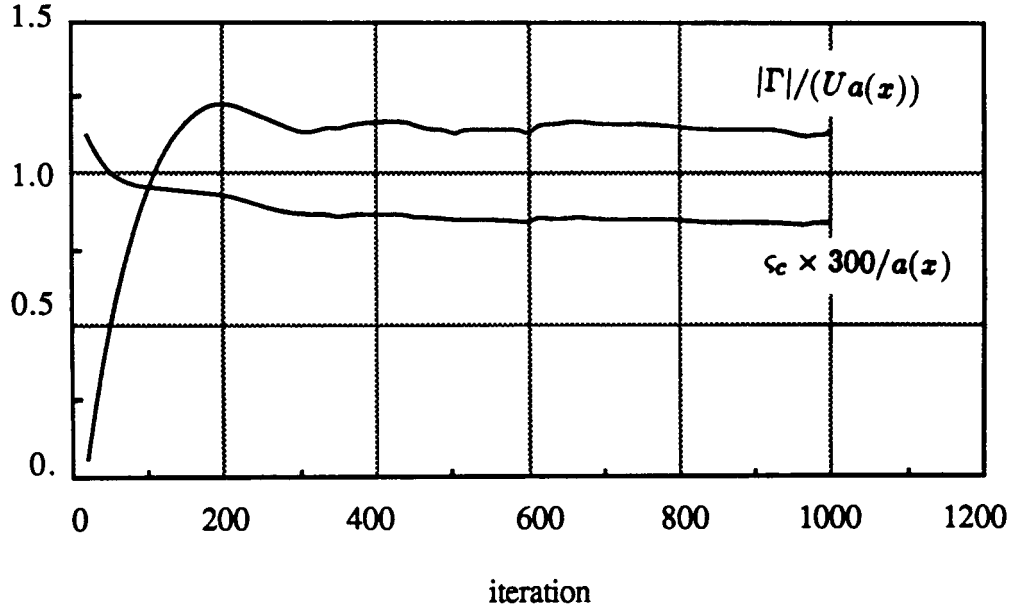

(b) Shear layer core strength and radius

Fig. 43 Calculation convergence

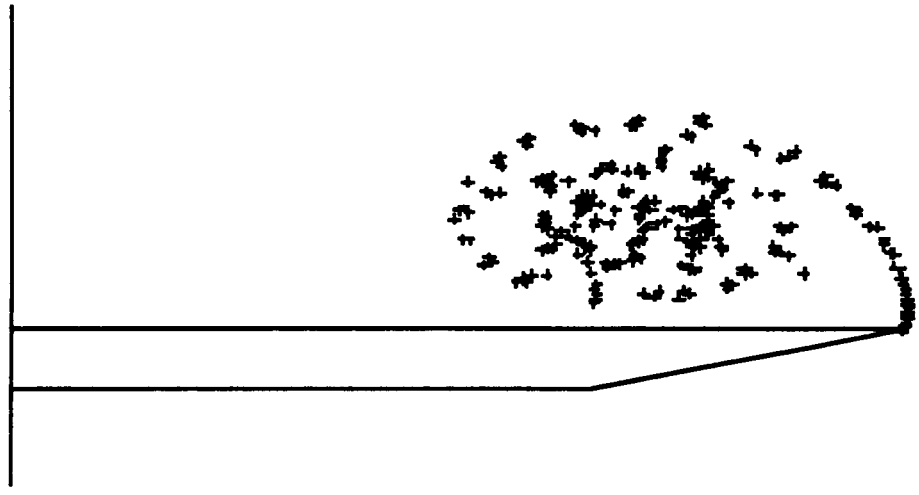

(a) Without core model

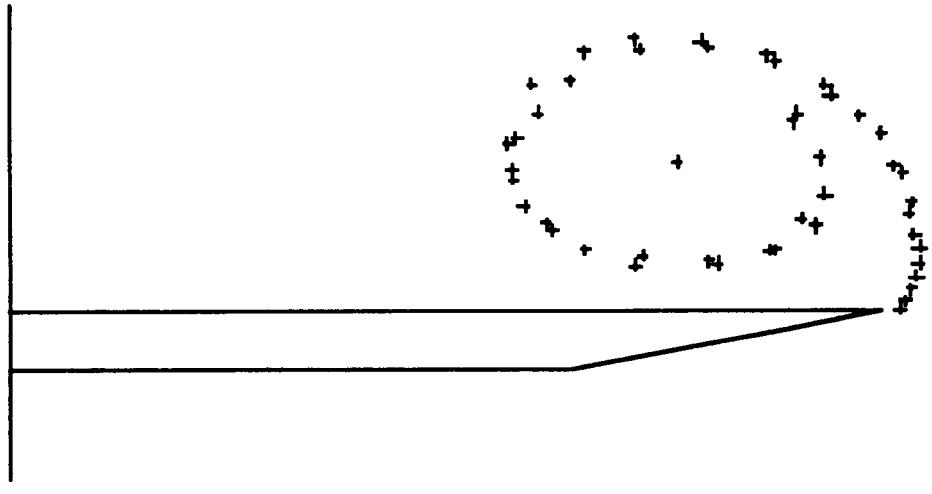

(b) With core model, 2.5π rotation angle

Fig. 44 Effects of shear layer core model, $\alpha = 25$ deg.

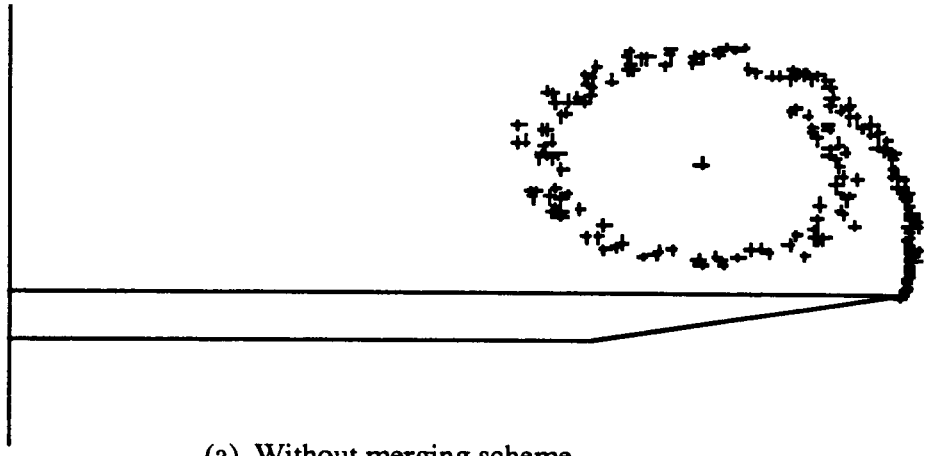

(a) Without merging scheme

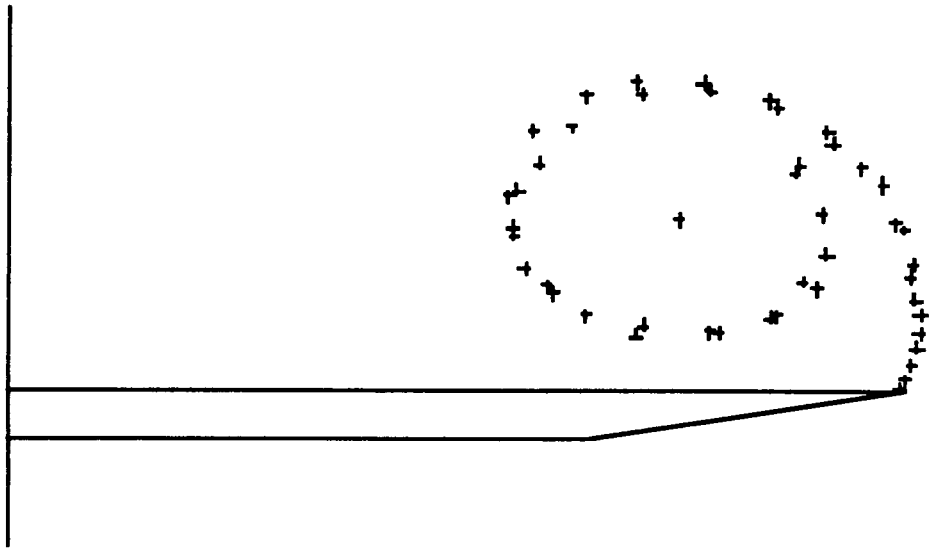

(b) With merging scheme

Fig. 45 Effects of merging scheme between neighboring vortices, $\alpha = 25$ deg.

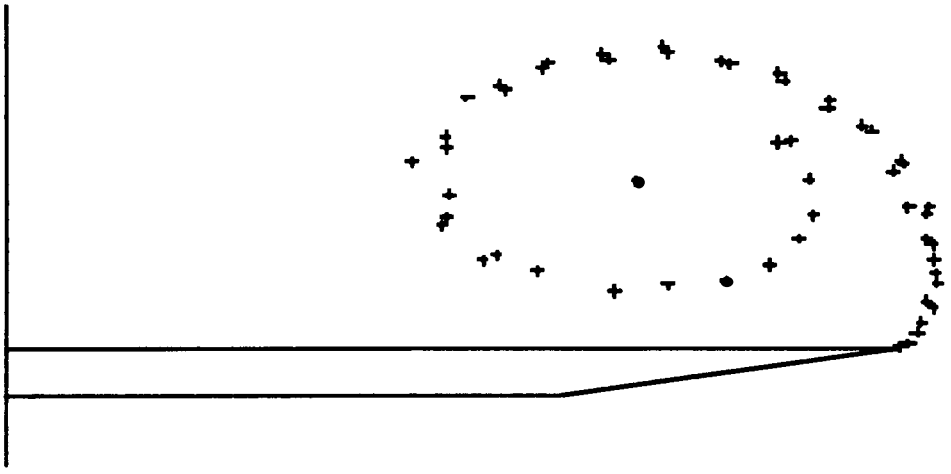

(a) 4th order Runge-Kutta method

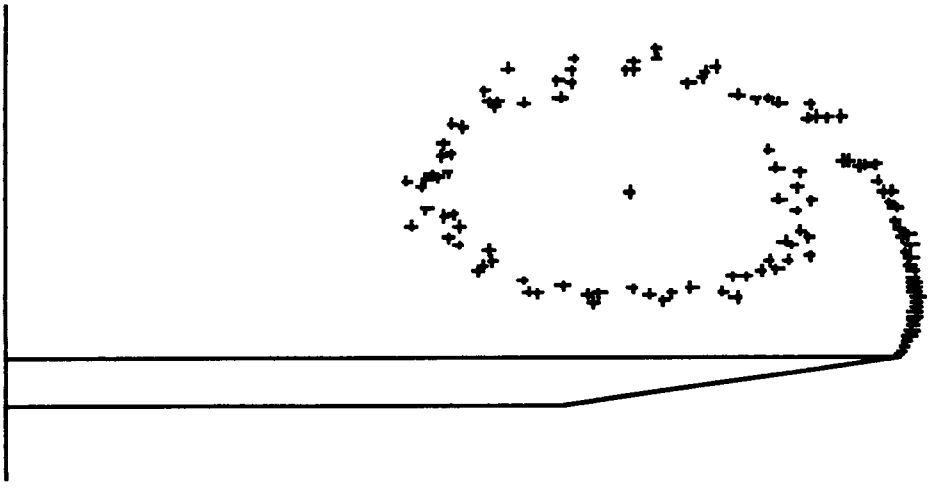

(b) 1st order Euler method

Fig. 46 Effects of integration scheme on shear layer geometry, $\alpha = 35$ deg.

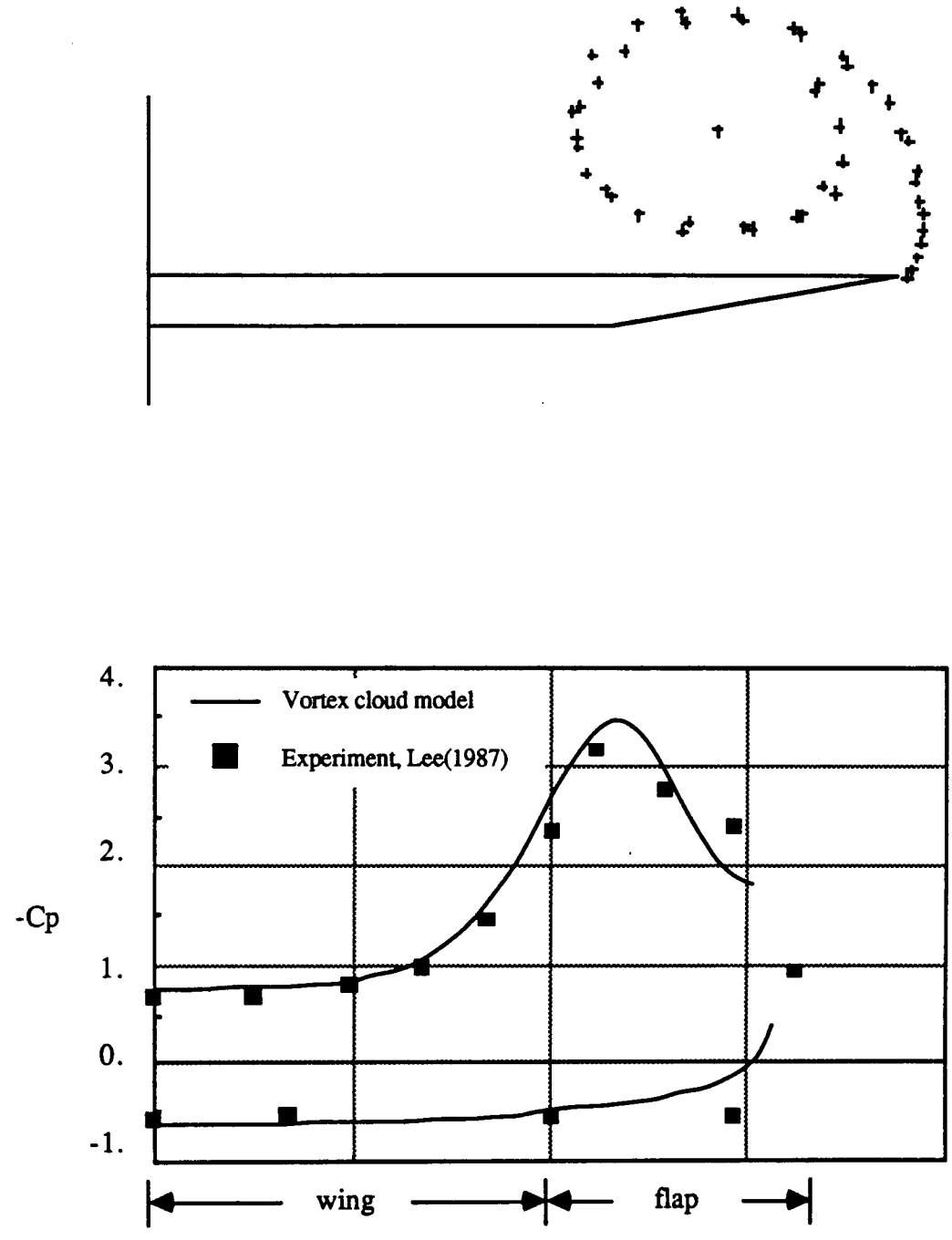

Fig. 47 Shear layer geometry and surface pressure distribution, $\alpha = 25$ deg., $\delta = 0$ deg.

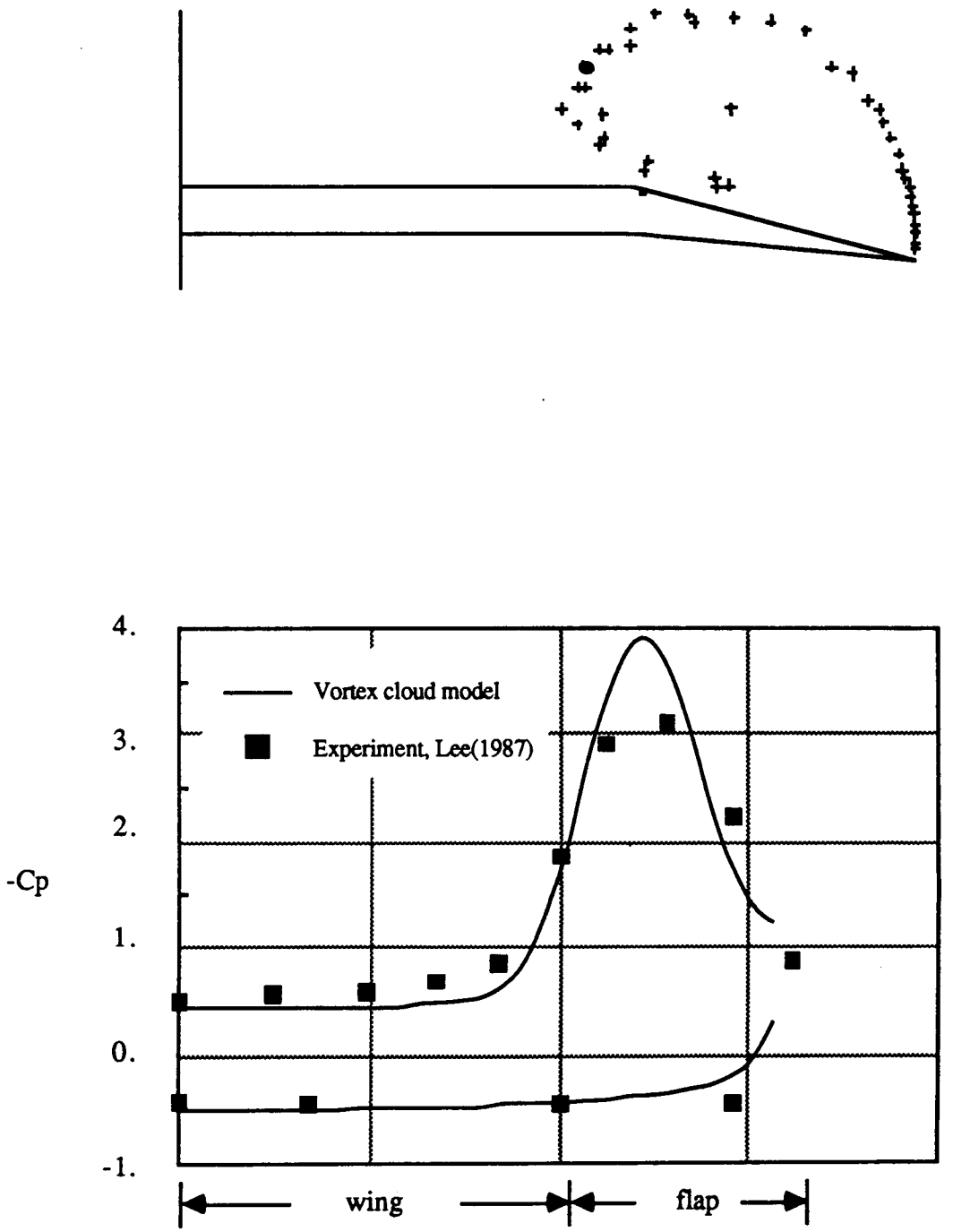

Fig. 48 Shear layer geometry and surface pressure distribution, $\alpha = 25$ deg., $\delta = 15$ deg.

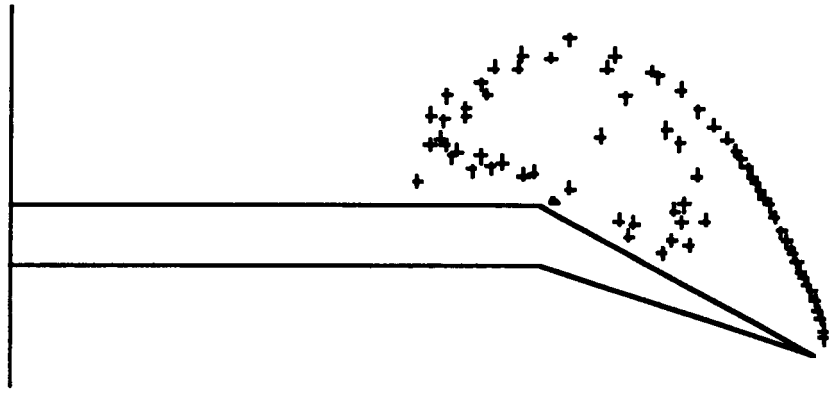

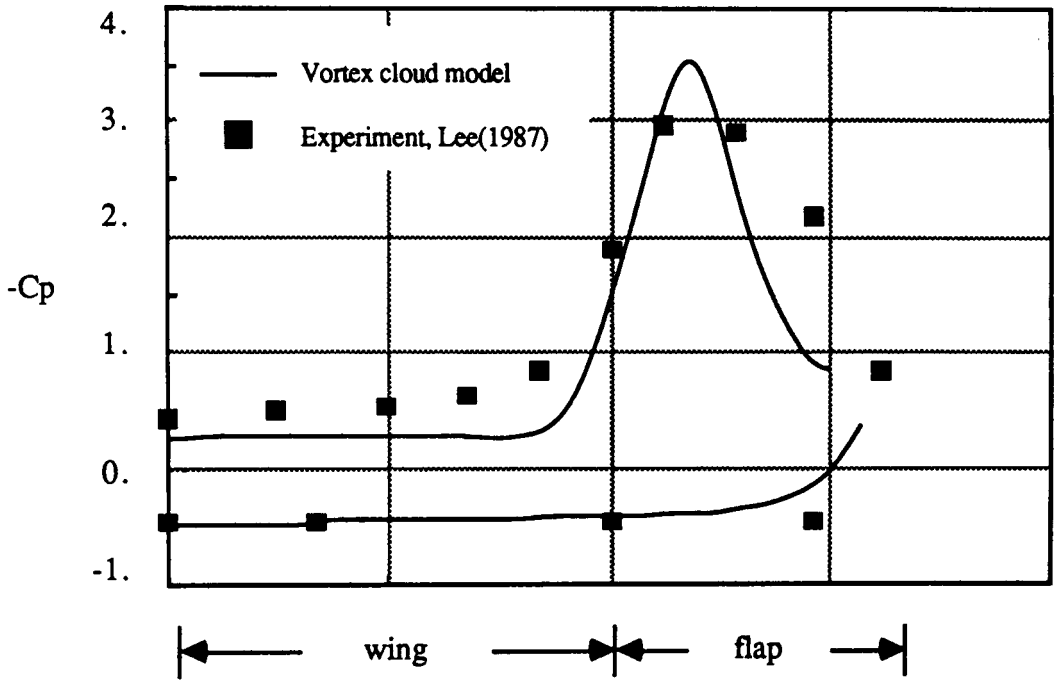

Fig. 49 Shear layer geometry and surface pressure distribution, $\alpha = 25$ deg., $\delta = 30$ deg.

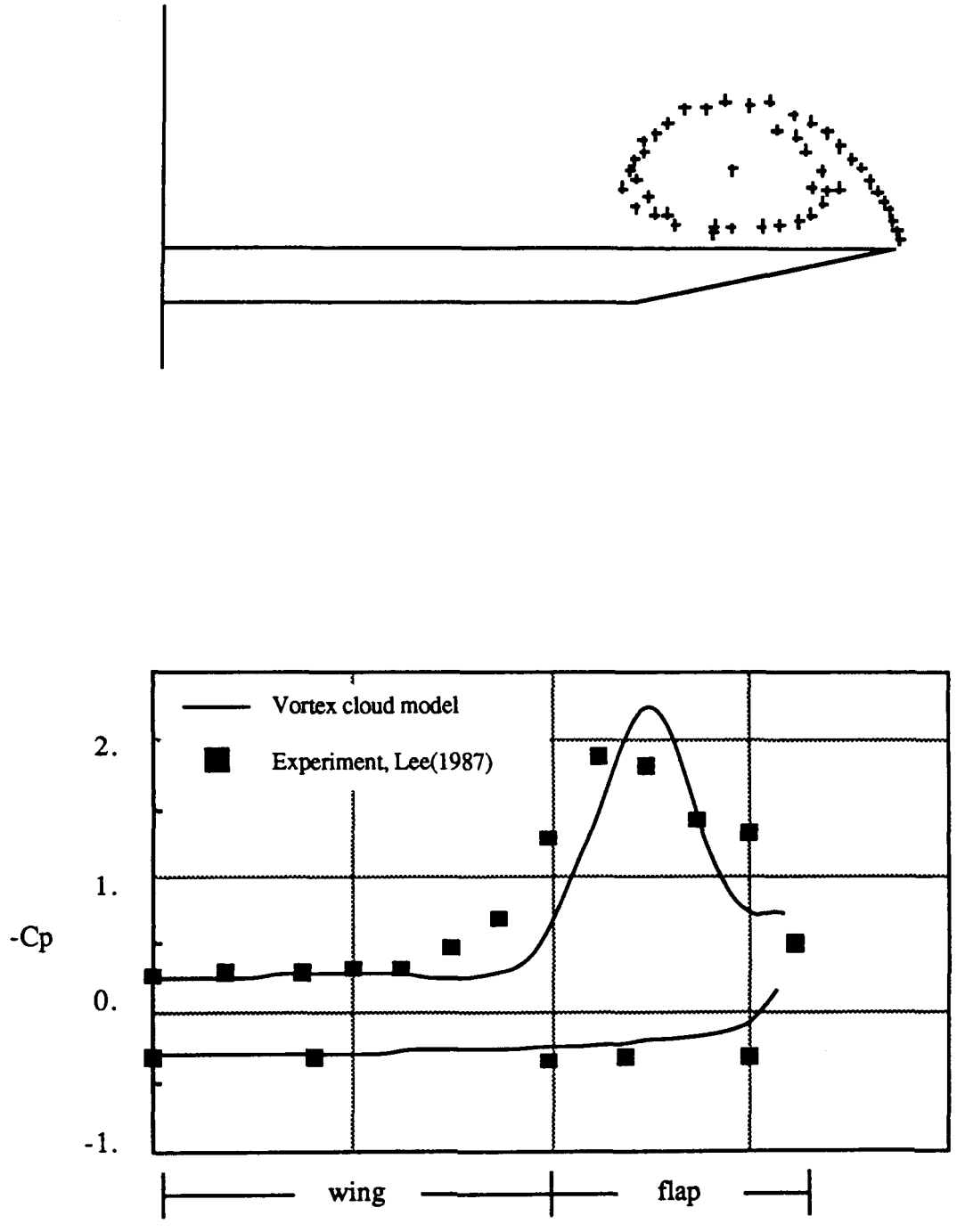

Fig. 50 Shear layer geometry and surface pressure distribution, $\alpha = 15$ deg., $\delta = 0$ deg.

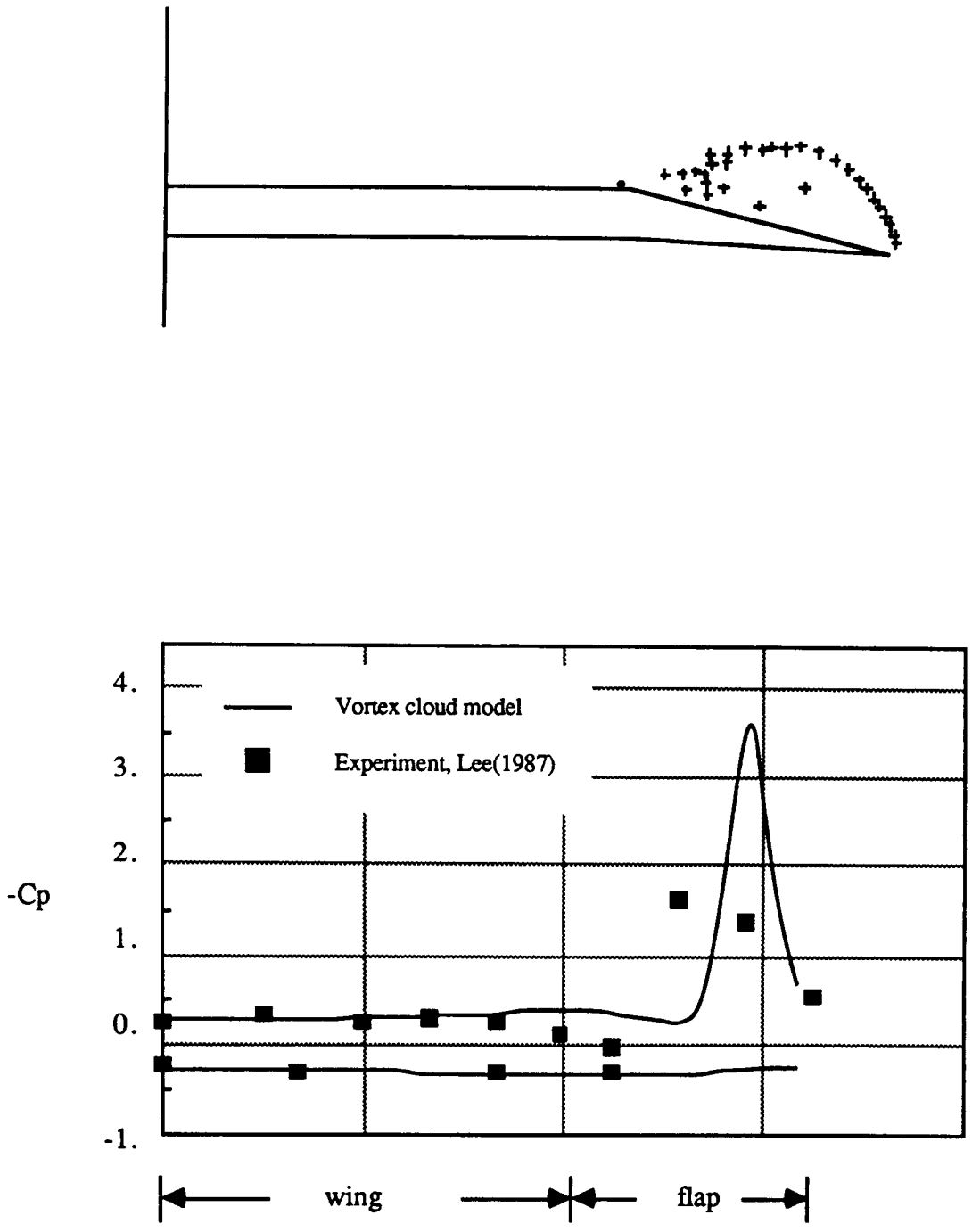

Fig. 51 Shear layer geometry and surface pressure distribution, $\alpha = 15$ deg., $\delta = 15$ deg.

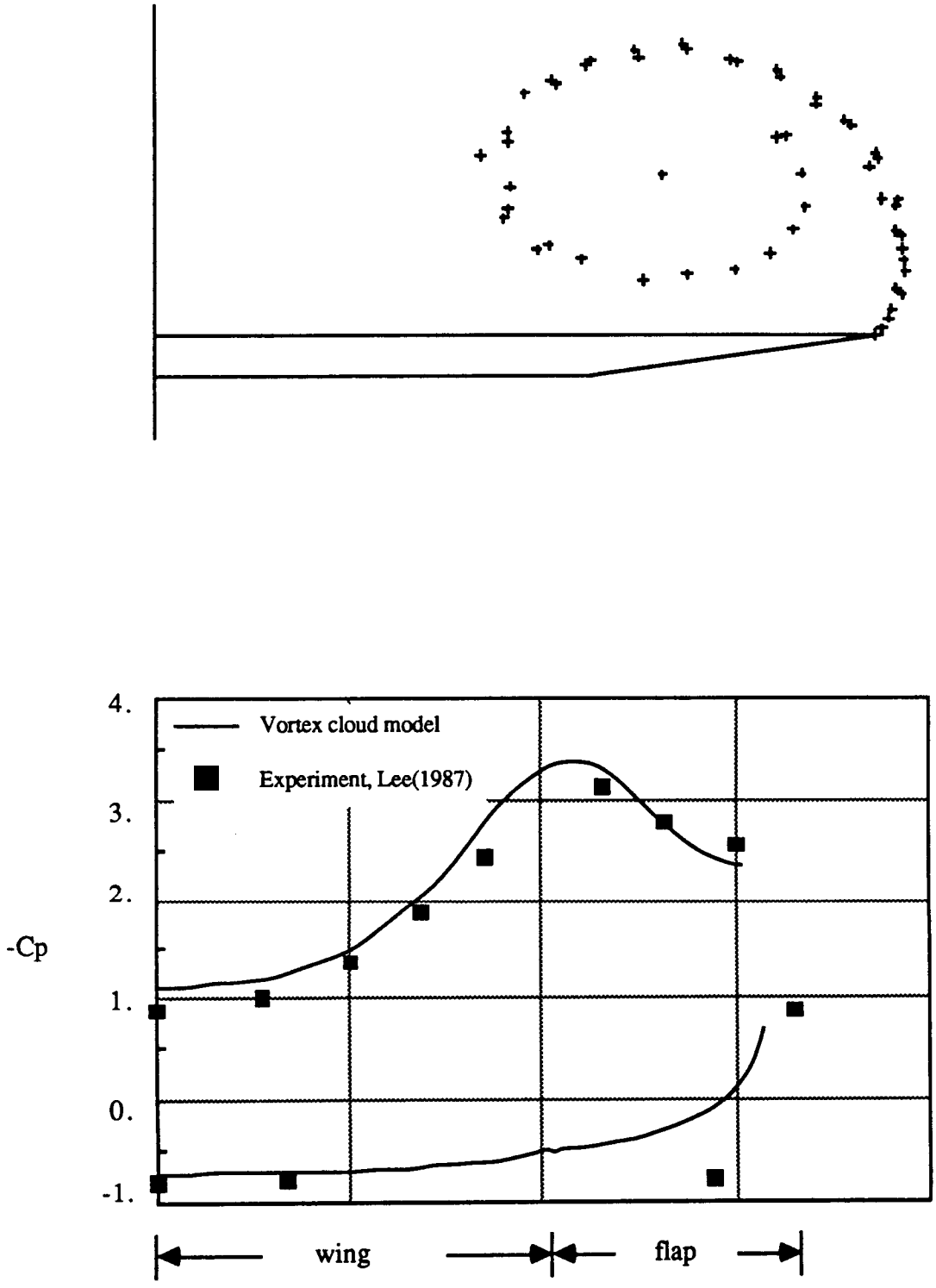

Fig. 52 Shear layer geometry and surface pressure distribution, $\alpha = 35$ deg., $\delta = 0$ deg.

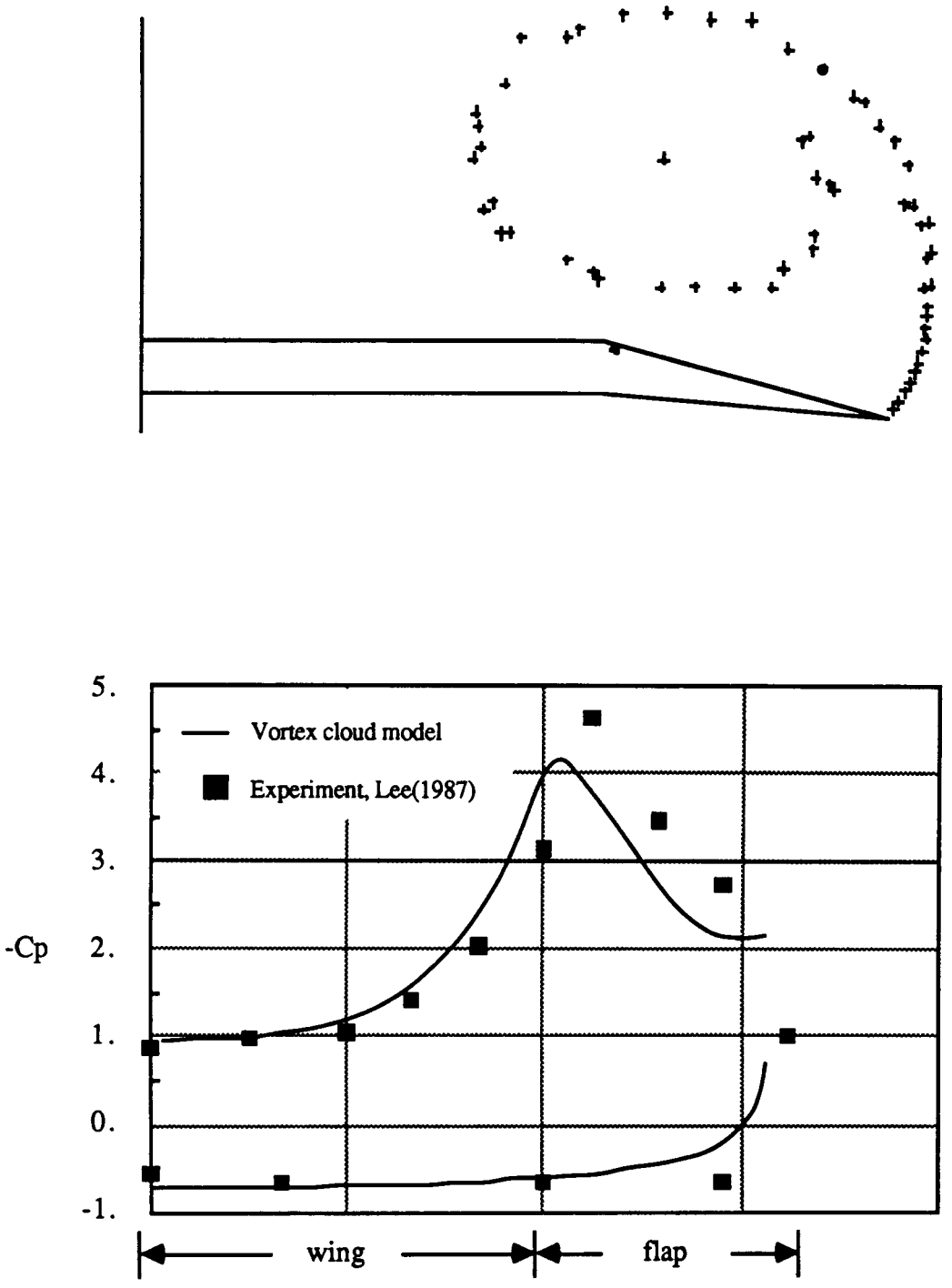

Fig. 53 Shear layer geometry and surface pressure distribution,
$\alpha = 35$ deg., $\delta = 15$ deg.

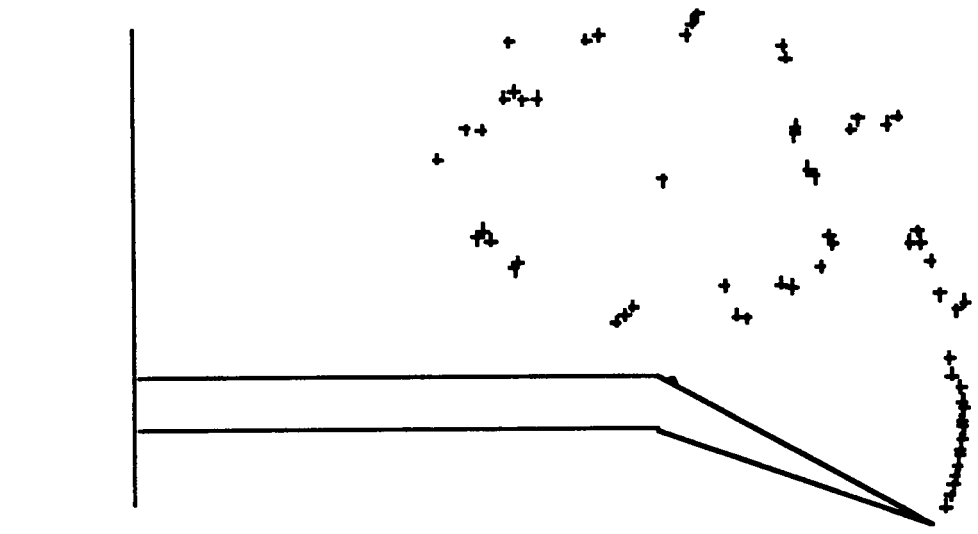

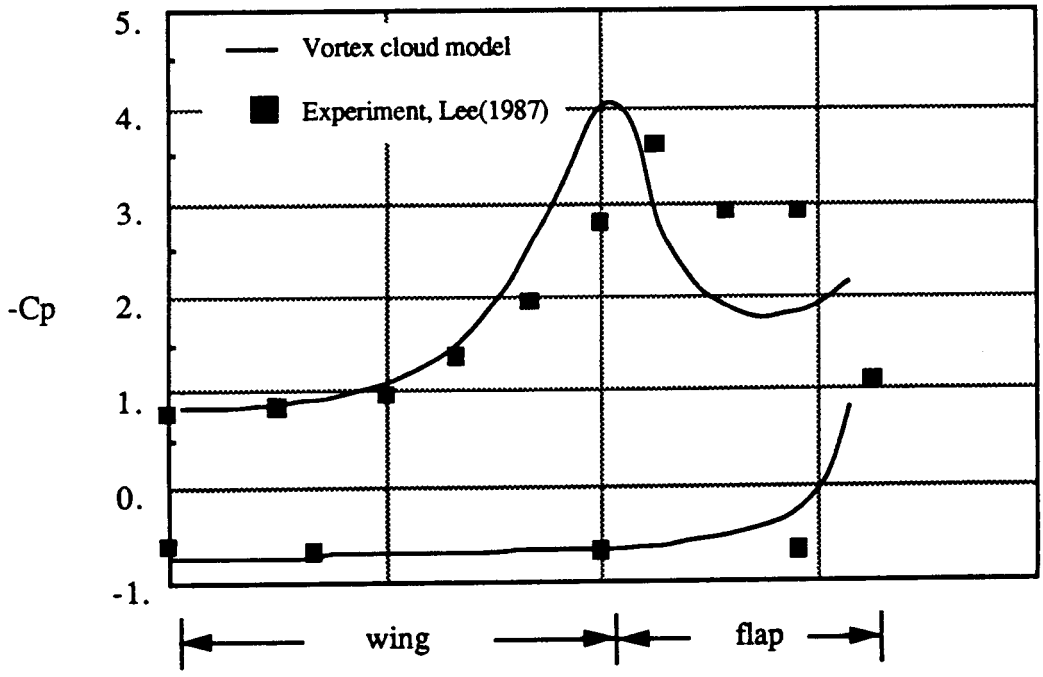

Fig. 54 Shear layer geometry and surface pressure distribution, $\alpha = 35$ deg., $\delta = 30$ deg.

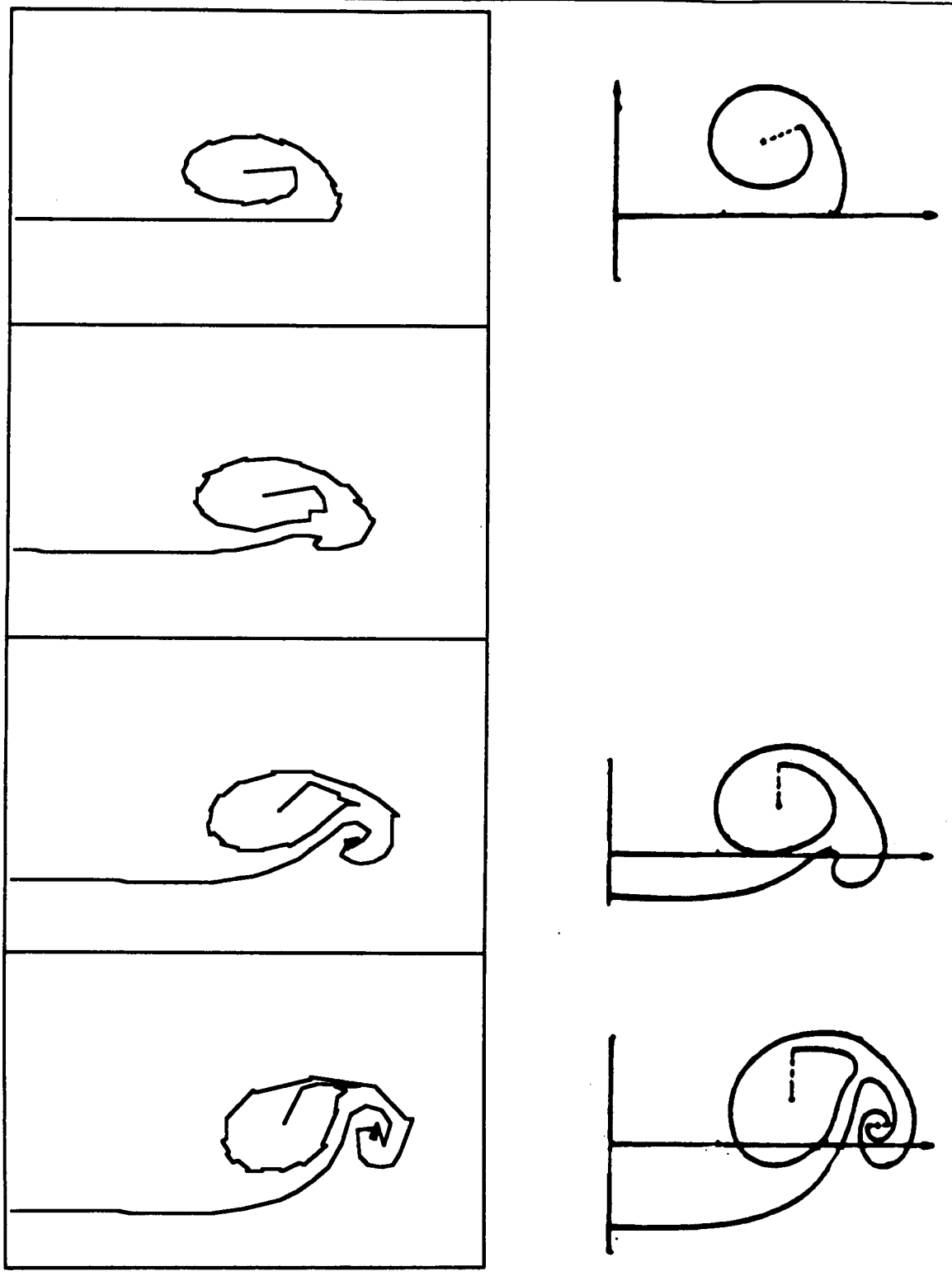

(a) Vortex cloud model

(b) Higher order panel method, taken form Ref. 61.

Fig. 55 Trailing edge wake evolution for a plane delta wing

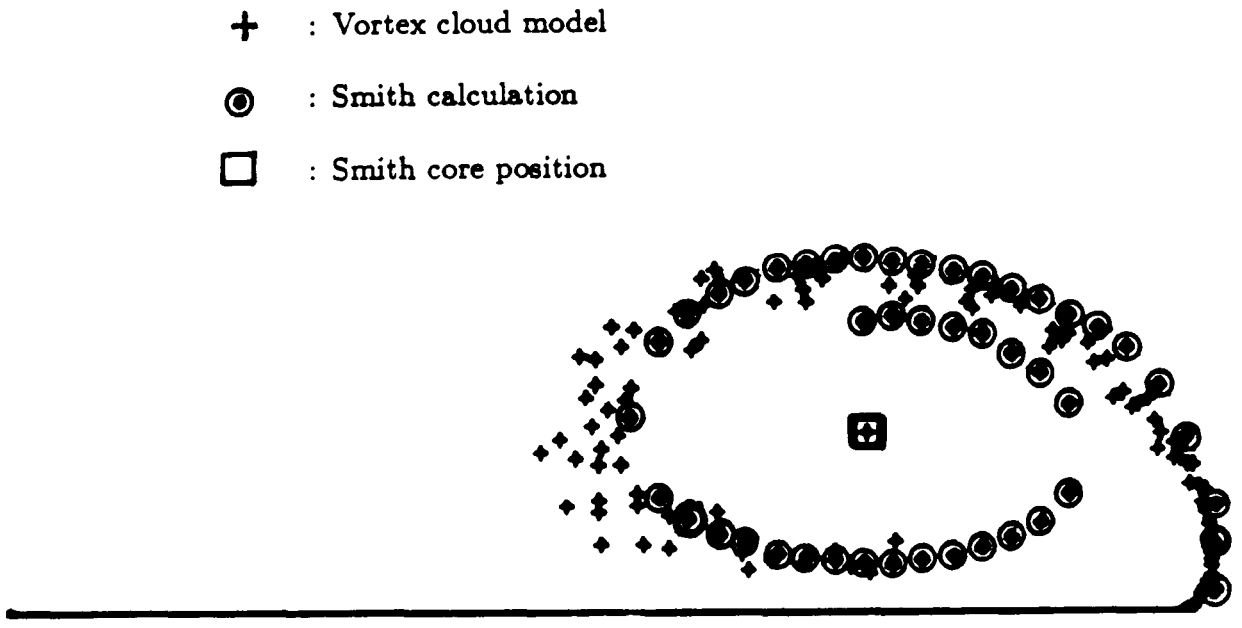

Fig. 56 Comparison of shear layer geometry with Smith's calculation for $\alpha/\epsilon = 1$

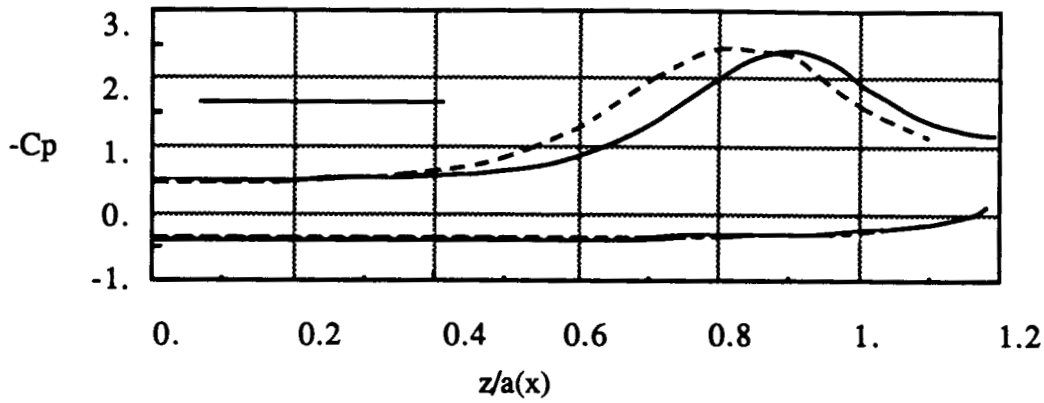

(a) no fence

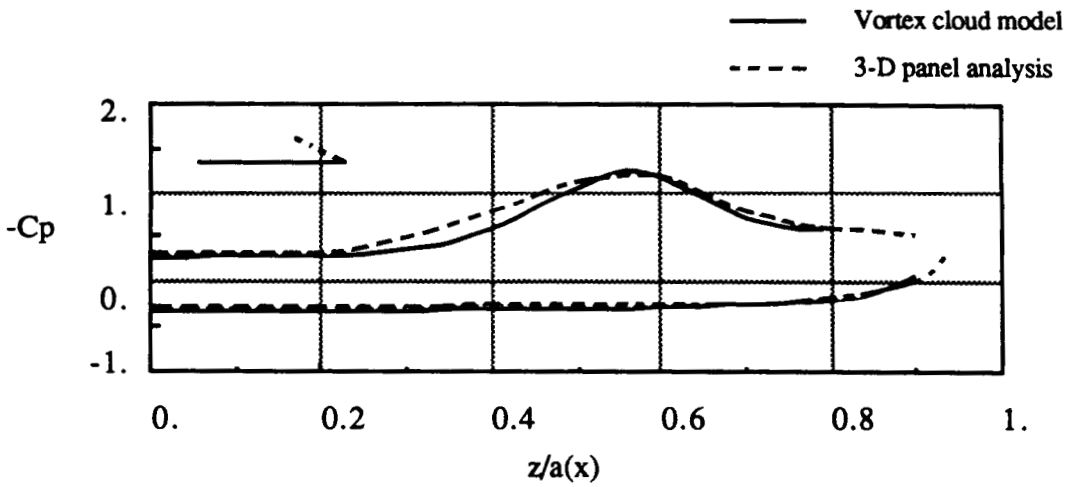

(b) main wing surface for $\delta = -130$ deg.

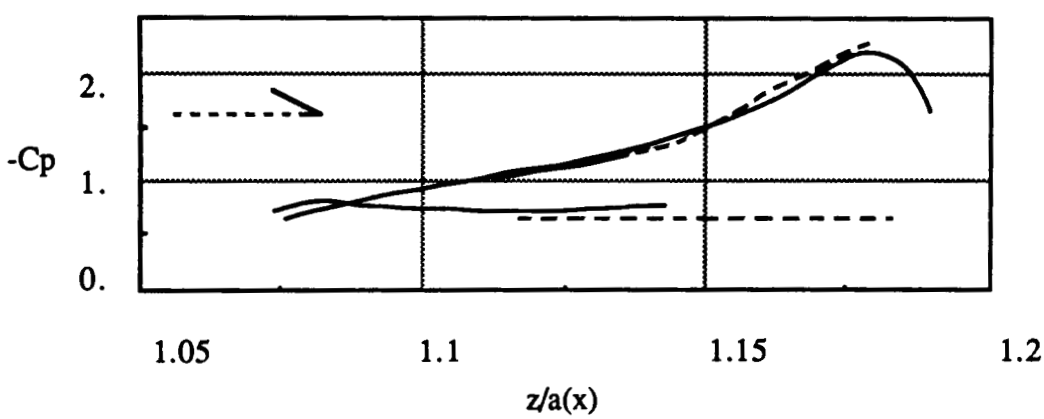

(c) Fence surface for $\delta = -130$ deg.

Fig. 57 Comparison with 3-D panel analysis

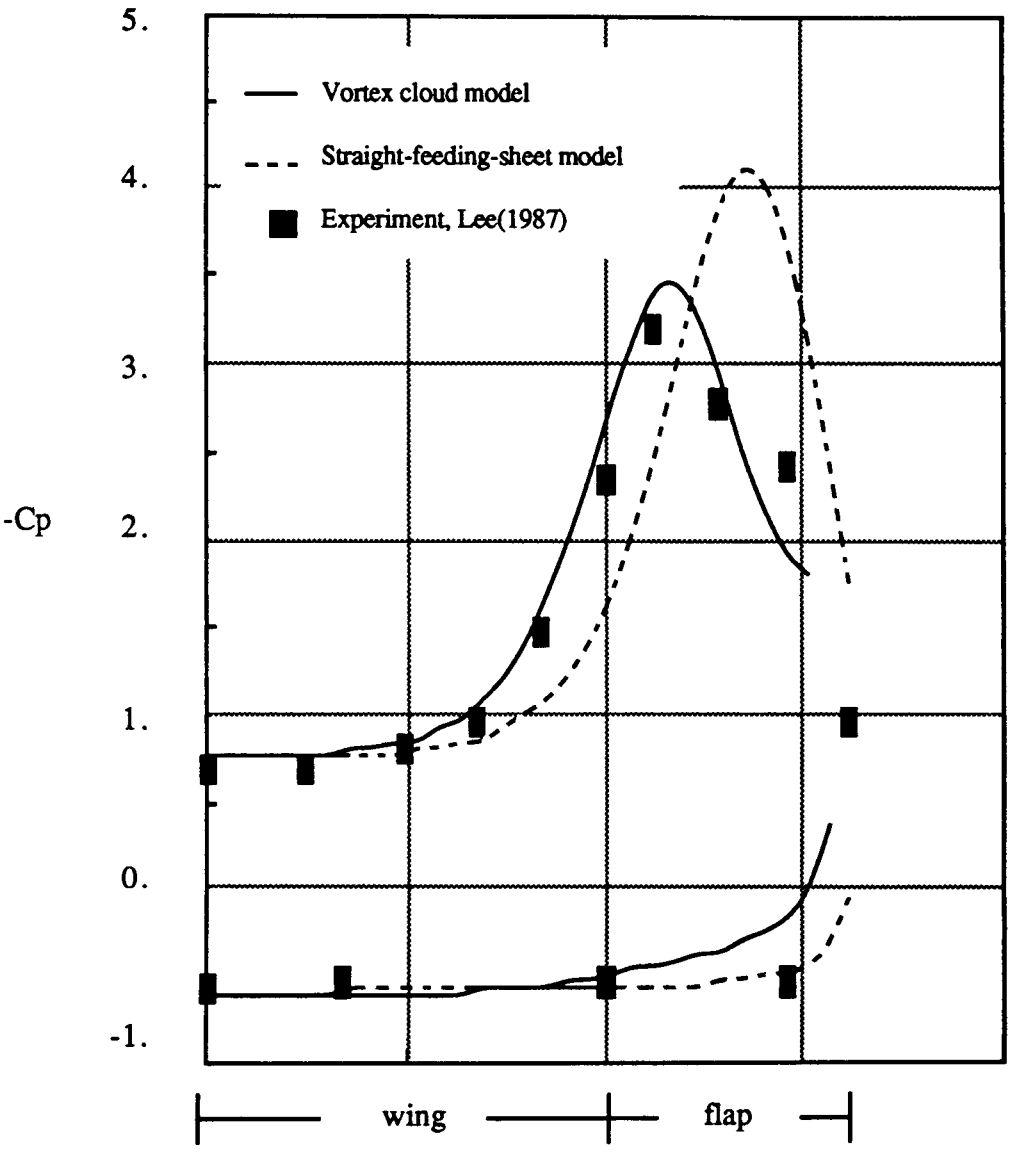

Fig. 58 Surface pressure distribution, $\alpha = 25$ deg., $\delta = 0$ deg.

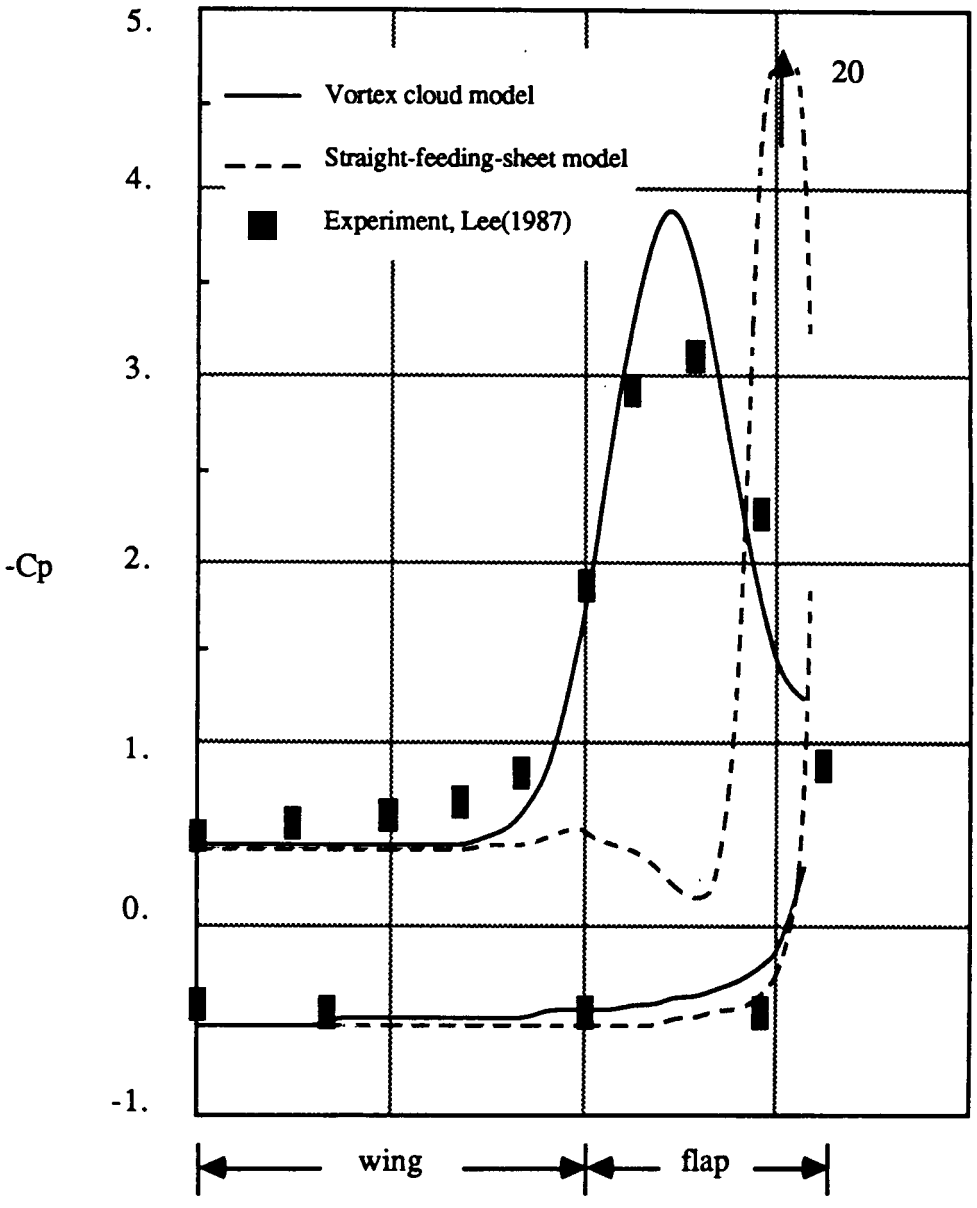

Fig. 59 Surface pressure distribution, $\alpha = 25$ deg., $\delta = 15$ deg.

Appendices

Appendix 1.

Wolfe Method

Eqs. (3.2.9a,b,c,d) are solved numerically using Wolfe method. Wolfe's method is a variation of the secant method for a system of nonlinear equations. This method has the advantage that as the solution becomes closer to the root, the convergence speed is much faster than that of Newton-Raphson method.[89] For a single equation the secant method is equivalent to solving the following two equations, with two initial guesses

$$p_1 + p_2 = 1 \qquad (A.1.1a)$$

$$p_1 f(x_1^n) + p_2 f(x_2^n) = 0 \qquad (A.1.1b)$$

The solution is updated as

$$x_3^{n+1} = p_1\, x_1^n + p_2\, x_2^n \qquad (A.1.2)$$

For a system of n equations a set of $n+1$ equations must be solved with $n+1$

vectors of initial guesses,

$$\sum_{j=1}^{n+1} p_j = 1 \qquad (A.1.3a)$$

$$\sum_{j=1}^{n+1} p_j \, f_i(x_1^j, x_2^j, \cdots, x_n^j) = 0 \qquad i = 1, 2, \cdots, n \qquad (A.1.3b)$$

For the solution update we ignore the vector $\mathbf{x}^j$, which gives the maximum residue.

$$\mathbf{x}^j|_{k+1^{th} \text{ step}} = \sum_{j=1}^{n+1} p_j \, \mathbf{x}^j|_{k^{th} \text{ step}} \qquad (A.1.4)$$

where $\mathbf{x}^j = (x_1^j, x_2^j, \cdots, x_n^j)$

This procedure is repeated until the maximum residue becomes smaller than a given value.

Appendix 2.

Newton-Raphson Method for Complex Functions

Eqs. (3.3.8a,b) are solved using the Newton-Raphson Method. Since these are complex equations, the conventional Newton-Raphson method is modified accordingly.

For the system of real equations

$$f_i(\mathbf{x}) = 0 \qquad i = 1, 2, \cdots, n \qquad (A.2.1)$$

the general form of the Newton-Raphson method is

$$\mathbf{x}_{n+1} = \mathbf{x}_n - J^{-1} \, f_i(\mathbf{x}_n) \qquad (A.2.2)$$

where J is the Jacobian of $f_i(\mathbf{x})$ at $\mathbf{x}_n$.

In the case of a system of complex equations

$$\mathbf{x} = (y_1 + iz_1, y_2 + iz_2, \cdots, y_n + iz_n) \tag{A.2.3}$$

Applying the scheme to the real and imaginary parts of f, there results

$$\begin{pmatrix} y_1 \\ z_1 \\ y_2 \\ z_2 \\ \vdots \\ y_n \\ z_n \end{pmatrix}_{n+1} = \begin{pmatrix} y_1 \\ z_1 \\ y_2 \\ z_2 \\ \vdots \\ y_n \\ z_n \end{pmatrix}_n - J^{-1} \begin{pmatrix} \Re\, f_1 \\ \Im\, f_1 \\ \Re\, f_2 \\ \Im\, f_2 \\ \vdots \\ \Re\, f_n \\ \Im\, f_n \end{pmatrix}_n \tag{A.2.4}$$

with

$$J = \begin{pmatrix} \Re\left(\frac{\partial f_1}{\partial y_1}\right) & \Re\left(\frac{\partial f_1}{\partial z_1}\right) & \cdots & \Re\left(\frac{\partial f_1}{\partial y_n}\right) & \Re\left(\frac{\partial f_1}{\partial z_n}\right) \\ \Im\left(\frac{\partial f_1}{\partial y_1}\right) & \Im\left(\frac{\partial f_1}{\partial z_1}\right) & \cdots & \Im\left(\frac{\partial f_1}{\partial y_n}\right) & \Im\left(\frac{\partial f_1}{\partial z_n}\right) \\ \vdots & \vdots & \ddots & \vdots & \vdots \\ \Re\left(\frac{\partial f_n}{\partial y_1}\right) & \Re\left(\frac{\partial f_n}{\partial z_1}\right) & \cdots & \Re\left(\frac{\partial f_n}{\partial y_n}\right) & \Re\left(\frac{\partial f_n}{\partial z_n}\right) \\ \Im\left(\frac{\partial f_n}{\partial y_1}\right) & \Im\left(\frac{\partial f_n}{\partial z_1}\right) & \cdots & \Im\left(\frac{\partial f_n}{\partial y_n}\right) & \Im\left(\frac{\partial f_n}{\partial z_n}\right) \end{pmatrix}_n \tag{A.2.5}$$

For the present problem there are two complex equations for the vortex positions, resulting in a 4×4 matrix. The reason why the Newton-Raphson method is preferred over the Wolfe method in this case, is that the latter needs a very accurate initial guess in order to converge.

Appendix 3.

Similarity Rule for Pressure Coefficient in Compressible Flow

Göthert's similarity analysis[97] is modified and applied to a general slender body at angle of attack.

The pressure coefficient for a compressible flow using the small disturbance assumption is

$$C_p = -2\frac{v_x}{U} - \left(1 - {M_\infty}^2\right)\left(\frac{v_x}{U}\right)^2 - \left(\frac{v_y}{U}\right)^2 - \left(\frac{v_z}{U}\right)^2 \qquad (A.3.1)$$

The analysis consists in considering two flow fields characterized by Mach numbers M_1 and M_2, with body shapes identified by the functions F_1 and F_2. Using a cylindrical coordinate system, the small disturbance potential equation for the flow field having free-stream Mach number M_1 and velocity U_1 with incidence angle α_1 can be written

$$\frac{\partial^2\phi_1}{\partial x^2} + \frac{1}{1 - {M_1}^2}\left(\frac{\partial^2\phi_1}{\partial r^2} + \frac{1}{r}\frac{\partial\phi_1}{\partial r} + \frac{1}{r^2}\frac{\partial^2\phi_1}{\partial\theta^2}\right) = 0 \qquad (A.3.2)$$

The boundary shape is given by

$$F_1 = r - b_1 c\, f_1(x/c, \theta) = 0 \qquad (A.3.3)$$

where b and c represent the aspect ratio and chord length of the wing respectively. The boundary condition on the wing surface given by Eq. (2.1.7) can be written as

$$\nabla\phi_1|_s \cdot \nabla F_1 = 0 \qquad (A.3.4)$$

where s indicates that $\nabla\phi_1$ is evaluated at the body surface.

Using Eqs. (A.3.2) and (A.3.3), Eq. (A.3.4) reduces to

$$\begin{aligned} -\left(U_1 + \frac{\partial\phi_1}{\partial x}\Big|_s\right) b_1 c\,\frac{\partial f_1}{\partial x} + \left(U_1 \tan\alpha_1 \sin\theta + \frac{\partial\phi_1}{\partial r}\Big|_s\right) \\ - \frac{1}{b_1 c f_1^2}\left(U_1 \tan\alpha_1 \cos\theta + \frac{\partial\phi_1}{\partial\theta}\Big|_s\right)\frac{\partial f_1}{\partial\theta} = 0 \end{aligned} \qquad (A.3.5)$$

Invoking the slender body assumption[81]

$$\frac{\partial\phi}{\partial x} \ll \frac{\partial\phi}{\partial r} \quad \text{and} \quad \frac{1}{r}\frac{\partial\phi}{\partial\theta} \qquad (A.3.6)$$

Eq. (A.3.5) reduces to

$$\left.\frac{\partial \phi_1}{\partial r}\right|_s = -U_1 \tan\alpha_1 \sin\theta + U_1 b_1 c \left.\frac{\partial f_1}{\partial x}\right|_s + \frac{1}{b_1 c f_1^2}\left(U_1 \tan\alpha_1 \cos\theta + \left.\frac{\partial \phi_1}{\partial \theta}\right|_s\right)\frac{\partial f_1}{\partial \theta} \tag{A.3.7}$$

and the pressure coefficient given by Eq. (A.3.1) becomes

$$C_{p1} = -\frac{2}{U_1}\left.\frac{\partial \phi_1}{\partial x}\right|_s - \frac{1}{{U_1}^2}\left(U_1 \tan\alpha_1 \sin\theta + \frac{\partial \phi_1}{\partial r}\right)_s^2 - \frac{1}{{U_1}^2}\frac{1}{{b_1}^2 c^2 {f_1}^2}\left(U_1 \tan\alpha_1 \cos\theta \frac{\partial \phi_1}{\partial \theta}\right)_s^2 \tag{A.3.8}$$

Next consider another flow field having Mach number M_2 and velocity U_2 with incidence angle α_2. The velocity potentials of the two flow fields are related as follows

$$\phi_1 = A \frac{U_1}{U_2}\phi_2\left(x, \sqrt{\frac{1-M_1^2}{1-M_2^2}}\, r, \theta\right) \tag{A.3.9}$$

where A is a constant to be derived later.

The new coordinates are

$$\tilde{x} = x, \qquad \tilde{r} = \sqrt{\frac{1-M_1^2}{1-M_2^2}}\, r, \qquad \tilde{\theta} = \theta \tag{A.3.10}$$

Substituting Eqs. (A.3.9) and (A.3.10) into Eq. (A.3.2) the latter reduces to

$$\frac{\partial^2 \phi_2}{\partial \tilde{x}^2} + \frac{1}{1-{M_2}^2}\left(\frac{\partial^2 \phi_2}{\partial \tilde{r}^2} + \frac{1}{\tilde{r}}\frac{\partial \phi_2}{\partial \tilde{r}} + \frac{1}{\tilde{r}^2}\frac{\partial^2 \phi_2}{\partial \tilde{\theta}^2}\right) = 0 \tag{A.3.11}$$

The body shape for the second flow field is defined by

$$F_2 = \tilde{r} - b_2 c\, f_2(\tilde{x}/c, \tilde{\theta}) \tag{A.3.12}$$

Accordingly, the boundary condition is

$$\frac{\partial \phi_2}{\partial \tilde{r}}\Big|_s = -U_2 \tan\alpha_2 \sin\tilde{\theta} + U_2 b_2 c \frac{\partial f_2}{\partial \tilde{x}}\Big|_s + \frac{1}{b_2 c f_2^2}\left(U_2 \tan\alpha_2 \cos\tilde{\theta} + \frac{\partial \phi_2}{\partial \tilde{\theta}}\Big|_s\right)\frac{\partial f_2}{\partial \tilde{\theta}} \tag{A.3.13}$$

and the pressure coefficient

$$C_{p2} = -\frac{2}{U_2}\frac{\partial \phi_2}{\partial \tilde{x}}\Big|_s - \frac{1}{{U_2}^2}\left(U_2 \tan\alpha_2 \sin\tilde{\theta} + \frac{\partial \phi_2}{\partial \tilde{r}}\right)_s^2 - \frac{1}{{U_2}^2}\frac{1}{{b_2}^2 c^2 f_2^2}\left(U_2 \tan\alpha_2 \cos\tilde{\theta} + \frac{\partial \phi_2}{\partial \tilde{\theta}}\right)_s^2 \tag{A.3.14}$$

Using the relationship given by Eq. (A.3.9) there results

$$\frac{\partial \phi_1}{\partial r}\Big|_s = A \frac{U_1}{U_2}\sqrt{\frac{1-M_1^2}{1-M_2^2}}\frac{\partial \phi_2}{\partial \tilde{r}}\Big|_s \tag{A.3.15}$$

Comparing boundary conditions (A.3.7) and (A.3.13) with relationships (A.3.9) and (A.3.10), under the assumption $f_1 = f_2$, there result

$$\sqrt{\frac{1-M_1^2}{1-M_2^2}}\, b_1 = b_2 \tag{A.3.16}$$

$$\sqrt{\frac{1-M_1^2}{1-M_2^2}}\, \alpha_1 = \alpha_2 \tag{A.3.17}$$

$$A = \frac{1-M_2^2}{1-M_1^2} \tag{A.3.18}$$

Hence, the pressure coefficients are related as follows

$$C_{p1} = \frac{1-M_2^2}{1-M_1^2} C_{p2} \tag{A.3.19}$$

which also implies that

$$C_p = \frac{1}{|1-M^2|} f\left(b\sqrt{|1-M^2|}, \alpha\sqrt{|1-M^2|}\right) \tag{A.3.20}$$